Nano Scale Devices: Fabrication, Actuation, and Related Fluidic Dynamics

Hao Jing

A dissertation submitted to the faculty of the University of North Carolina at Chapel Hill in partial fulfillment of the requirements for the degree of Doctor of Philosophy in Curriculum in Applied and Materials Sciences.

Chapel Hill
2006

Approved by:

Advisor: Professor Richard Superfine

Professor Sean Washburn

Professor Otto Zhou

Professor Leandra Vicci

Professor Brian Stoner

ABSTRACT

Hao Jing

Nano Scale Devices: Fabrication, Actuation, and Related Fluidic Dynamics

(Under the direction of Professor Richard Superfine)

Using external actuating magnetic fields to manipulate magnetic parts is an efficient method to manipulate mesoscopic actable devices. Extensive researches have explored the potentials of self-assembly techniques based on capillary force, static charge force, drying, surface tension, and even dynamic fields as a low cost method for ordered 2D or 3D super-lattice structures for new materials and devices. But the ability of tunable patterning nano-particles for designed actable devices is still a requirement yet to be met. Utilizing anodized aluminum oxide (AAO) membranes as templates, soft-magnetic nanowires around 200 nm in diameter, 10 microns long have been fabricated. In this thesis, I describe a method to assemble these magnetic nanowires into a two dimension Wigner structure, of which the wire-wire distance is conveniently adjustable during the fabrication procedure. Using geometric tailored magnetic fields, we can plant these self-assembled magnetic nanowires with desired patterns into a thin soft polymer support layer. The final devices may be readily actuated by an external actuating magnetic field (a self-designed magnetic system, 3-dimensional force microscope (3DFM)) with precise patterns and frequencies in a micro-fluidic system. This

method offers a general method to fabricate mesoscopic devices from a wide range of materials with magnetic dipoles to desired structures. And the actable devices themselves can find direct usage in low Re number flow mixing and bio-physical fluidic dynamic researches.

The beating of cilia and flagella, slender cylinders 250 nanometers in diameter with lengths from 7 to 50 microns, is responsible for many important biological functions such as organism feeding, propulsion, for bacterial clearance in the lungs and for the right-left asymmetry in vertebrates. The hydrodynamics produced by these beating structures, including mixing, shear and extensional flows, is not understood. We developed an experimental model system for cilia beating through the use of magnetic nanowires. We apply our custom magnetic system, 3DFM, to drive these magnetic nanowires rotating with desired patterns and frequencies in a liquid chamber. High speed movies of passive tracers in the oscillating 3-D flow fields reveal the spatio-temporal structure of the induced fluid motion. Complementing these experimental studies, we have developed a family of exact solutions of the Stoke's equations for a spheroid sweeping a double cone in free space, and an asymptotic solution for a spinning slender rod sweeping an upright cone above a flat, infinite no-slip plane. We are using these solutions to develop a mathematical package to quantitatively model, and predict the tracer motion induced by the spinning nano-rods with and without Brownian noise.

To understand the effect of these epicyclical flows on molecular conformations, we have studied the conformation of fluorescently labeled, single DNA molecules (λ-DNA) in the flow produced by a precessing nanowire. The flow patterns in a viscoelastic medium

about a precessing nanowire are also presented to reveal the epicyclical flows in a more bio-related environment.

ACKNOWLEDGEMENTS

This thesis would not have been possible if the 3DFM did not exist. For that, I would like to thank Dr. Richard Superfine and his 3DFM team. His vision to fund such a risky and ambitious nano-fluidic project paved the way to the completion of my thesis work. He is such a good friend and a great leader. It is he that gives me all the necessary support and encouragement so that a foreign polymer material scientist can enjoy the happiness of cutting-edge biophysical research here.

I offer sincere appreciation to Sean, Leandra and Mike. The inspiring talks with you guys are a truly enjoyable experience for me. I would love to thank Dr. Samulski and his group for their endless supports. I would also love to thank Otto, Brain, JP, and Frank. Their consultation on a lot of theoretical and experimental difficulties I met really smoothed my research.

I owe a lot thanks to the RMX researchers who are Richard McLaughlin, Roberto Camassa, and Terry Jo Leiterman. RMX is such an important part of my research that I can not imagine my research could go this far without them.

3DFM guys, I feel proud to be one of your team members. Ben, Jeremy, Kalpit and Jay, you guys are cool. Ben is such an important factor here since whenever he is around I

TABLE OF CONTENTS

LIST OF TABLES

LIST OF FIGURES

CHAPTER 1 – Overview of Thesis

Actuable mesoscale devices are key functional units for a lot of applications, such as micromixers, lab-on-chip separation chambers, and optical camouflage coatings. Fabricating sub-micron scale actuable devices by bottom-up strategies instead of by more expensive photolithography techniques is the critical step to make these devices feasible for practical applications.

Self-assembly techniques, as one of the most important bottom-up strategies, are not unfamiliar techniques to nanoscientists. Most of them, however, are more or less like an art, not easily controlled or predictable. Magnetic dipoles, such as magnetic nanowires or lines of paramagnetic beads, were suggested in recent years as potential candidates for actuable sub-micron scale devices. In our lab, soft-magnetic nanowires with a mean radius of 200 nm were electrodeposited in anodically etched commercial aluminum oxide membranes. We found that magnetic nanowires form 2D Wigner structures under a parabolic magnetic confinement field. These magnetic dipoles experience a net force along the magnetic field gradient as well as a torque under an external magnetic field. Based on finite element analysis modeling, parabolic magnetic potential wells were realized with a home-made solenoid electromagnet. The lattice distances of the final Wigner structures were tunable between several microns to tens of microns depending on field strength, total number of the nanowires, and nanowire dipole strength. A dimensionless Monte Carlo simulation was performed on an idealized

model for a better understanding the self-assembly patterns. Free standing magnetic nanowire devices were fabricated with this self-assembly mechanism and the roots of the nanowires were cured within a thin soft polymer layer. After curing this thin layer of polymer, we demonstrated a fast-response actuation by placing the standing nanowire devices in a magnetic manipulation system designed by our group, the 3 Dimensional Force Microscope (3DFM).

In nature, sub-micron scale cilia and flagella are found in almost all single cellular animals and complex multicellular animals. The beating of cilia and flagella, slender cylinders 250 nanometers in diameter with lengths from 7 to 50 microns, is responsible for many important biological functions such as feeding and propulsion, for bacterial clearance in the lungs and for the right-left asymmetry in vertebrates. Inspired by these naturally evolved sub-micron actuator arrays, and basing our designs on the self-assembly patterns we discovered, we proposed and fabricated sub-micron actuator arrays which can mimic the movements of a specific kind of motile cilia, primary nodal cilia. These devices were actuated and observed inside the 3DFM. Besides their obvious engineering applications, these devices are good platforms for studying fluidic dynamics about mobile primary cilia due to the similarities between precessing rigid nanowires and nodal cilia.

Researchers have long recognized that flow in low a Reynolds regime is the central mechanism for many biological processes, including microbe swimming, feeding, and mucociliary clearance. In the past 20 years, researchers have shown that nodal flow has a direct effect on right-left asymmetric development in vertebrate embryos. It is a general belief now that this nodal flow is a direct consequence of beating nodal cilia (belonging to the class of cilia known as motile primary cilia). The fundamental fluidics of this flow,

however, is still a mystery due to the unanswered question of what the flow field about a precessing slender body is. It is of interest to us to explore this flow based on rigorous fluid dynamics studies on the sub-micron scale. This is the first time, as far as we know, that an experiment modeling fluid flow was performed on such a small scale to understand a biologically related flow with thermal noise of comparable magnitude. Collaborating with Terry Jo Leitermann from the Department of Applied Mathematics at UNC, we compared our experimental results to the exact solutions Leitermann derived from basic Navier-Stokes functions in a low Reynolds viscous environment. This exact solution is not trivial, and because of the accurate predictions it provides, this is the first time that researchers can interpret experimental measurements on such a scale in the presence of prominent thermal fluctuations.

In this thesis, I describe the details of soft magnetic nanowire (Ni:Fe) fabrication based on the template methods outlined in Chapter 2. In Chapter 3, the actuation of standing magnetic nanowires in the 3DFM is demonstrated and explained in detail. In Chapter 4, I focus on Wigner structures formed by magnetic nanowires in a parabolic assembly field. The mechanisms for these self assembly phenomena are interpreted by the coordinate-dependent part of the Hamiltonian and tested by dimensionless Monte Carlo simulations. The epicyclical flow about a precessing nanowire is experimentally and theoretically revealed in Chapter 5. I describe the epicyclical flow in more biologically relevant media in Chapter 6.

CHAPTER 2 – Nanowire Fabrication

2.1   Introduction

In this chapter, fabrication procedures for magnetic metal nanowires are introduced in detail. Here, "nanowire" means a rod-shaped material with a sub-micron radial scale and an aspect ratio of about 50-100. There are several methods of fabricating this kind of 1-D nano structure. The most straightforward methods are photo lithography and e-beam lithography. It is possible, however, to use bottom up strategies like self-assembly or template methods for nanowire fabrication as well.

Template methods include a large family of very different techniques like growing materials by step edges on a layer structured crystal surface, growing materials inside self-assembled templates formed by surfactants or block polymers, and growing materials inside reactive ion etched polymer membranes or anisotropic etched inorganic membranes [1] [2] [3] [4]. By far, the template method is the most commonly used and easily accessible method for producing large quantities of inorganic nanowires. Wet chemistry synthesis and chemical vapor deposition (CVD) have been recognized as good strategies for growing materials inside confined geometries. 1-D nano structured materials can be grown directly inside appropriate templates.

Two of the most commonly used templates are track etched polymer films and anodized aluminum oxide (AAO) membranes. Track etched membranes are typically polymer films which have been irradiated by heavy ions. The damaged bonds along the particle tracks are preferentially etched away, leaving pores inside the membrane. The pores fabricated by this method are generally distributed randomly across the surface, and the orientation of these channels cannot be controlled easily. Channels tilted over 30° are not hard to find in this kind of template. To produce metal nanowires with precise geometries, AAO is a better choice. AAO membranes are fabricated by anodizing Aluminum in an acid electrochemical bath. Unlike the track etched polymer films, AAO membranes form hexagonal close-packed channels perpendicular to the membrane surface and parallel to each other. There are many techniques for growing nanowires inside AAO templates, such as vapor phase deposition, solution injection, melt filling, electrophoresis deposition and electrodeposition[5] [6] [7] [8].

Among the growing techniques listed above, electrodeposition is especially attractive for metal nanowire growth due to its economy and convenience. For modern scientists, it is not unusual to control the plating procedure in a highly precise layer-by-layer (atomic level) manner [9].

2.2   Electrodeposition of Soft-magnetic Ni:Fe Permalloy Nanowires

2.2.1   The Concept of Electrodeposition

Electrodeposition is the process of producing a coating, usually metallic or at least conductive, on a surface by reductant-oxidant (redox) reactions along with charge exchanges [10]. This is achieved by applying negative charges to the object to be coated and allowing

them combine with the hydrated ions of the metal to be deposited. In other words, the object to be plated is the cathode of an electrodeposition cell (an electrolytic cell). The metallic ions carry positive charges. When they reach the negatively charged object, the redox reaction occurs so that desired metal film is coated on the cathode surface. The reduction of a metal can be generalized as,

$$M_{(aq)}{}^{z^+} + ze^{-1} \rightarrow M(s) \qquad (1),$$
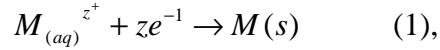
meaning that to reduce one mole of a Z valence metal, z moles of electrons are required. The total cathode charge consumed in the deposition Q, Coulomb, is

$$Q = zN_aQ_e \qquad (2)$$

N_a is Avogadro's number and Q_e is the electrical charge per electron [10]. The total charge transferred in the deposition can be obtained by the integration of the current I and the time of deposition t if the deposition current is held constant.

$$Q = \int Idt \qquad (3)$$

Solving for thickness while assuming the deposition current efficiency is 100%,

$$H = \frac{M_w}{zFA\rho} \int Idt \qquad (4)$$

Here H is the deposited film thickness, M_w is the molecular weight, F is the Faraday constant, A is the effective plating area, and ρ is the metal density. As function (4) indicates, as long as the current efficiency remains constant, the deposition layer thickness is proportional to the deposition time. By controlling the time or the exchanged total charge, the deposition thickness is easily controlled.

2.2.2   Co-deposition of Ni:Fe Nanowires

Permalloy, a soft magnetic Ni:Fe alloy, is an important industrial material known for its high saturation field strength and low coercive force. Nanowires made of Ni:Fe have benefits such as being able to respond to a noninvasive magnetic field and saturate easily in a moderate magnetization field [11, 12].

Electrodeposition of nickel-iron alloys is classified as an anomalous co-deposition because the discharge rate of the more noble component, Ni, is inhibited, causing the less noble metal, Fe, to exhibit a higher atomic ratio in the final deposited material than its share in the electrolyte [13]. The explanation of this phenomenon is that the local pH value rises due to the hydrogen dissociation accompanying the electrodeposition process. I performed an optimizing procedure to find a more stable deposition bath. Pressing a multi welled PDMS template to a polished Cu sheet and injecting electrolytes of various compositions into the wells, I produced an array of electrolytic cells and plated multiple samples at one time (figure 2.1). I measured these plated samples using EDAX for optimal composition.
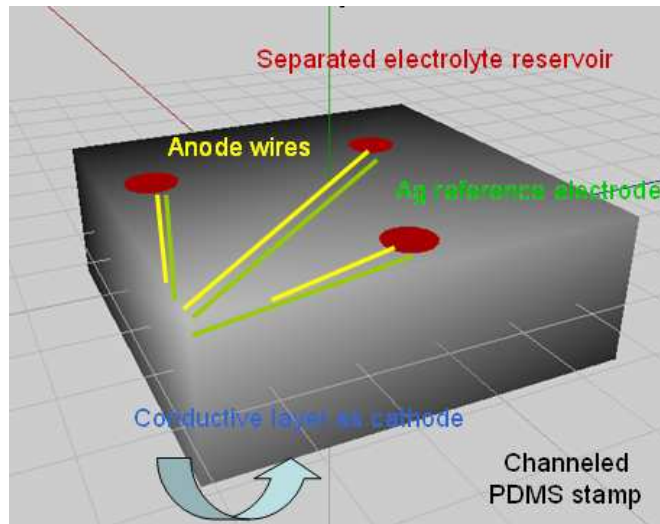
Figure 2.1, Representative structure of a multi-welled PDMS stamp used to screen the optimized electrolyte bath for Ni:Fe co-deposition. Electrolytes with different Ni^{2+}:Fe^{2+} ratio were injected inside the wells for electrodeposition under the same plating parameters. The composition of plated metal layers was measured by EDAX to determine the optimal recipe.

There are several techniques which can be used to improve magnetic nanowire growth. One way chosen to reduce the Fe content and thereby reduce the anomalous behavior is by pulse and pulse reverse plating[13]. By allowing enough time for fresh metallic ions to diffuse, a much more uniform deposited material could be collected. Organic additives like saccharin (figure 2.2) can suppress the hydrogen evolution by absorbing metallic ions on the surface of the substrates. The presence of organic additives also helps relieve the stress of the deposited alloy[13]. With the help of devices illustrated in figure 2.1, I produced an optimized sulfate-based plating bath working in pulse galvanostatic deposition mode by a VoltaLab^R work station from Radiometer Analytical Co. (table 2.1).
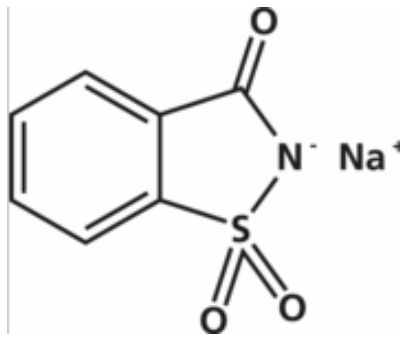
Figure 2.2, The chemical structure of saccharin.

The applied potential for Ni:Fe co-deposition is above the water decomposition voltage -0.994 V at pH 4 which can be valued through a Pourbaix Diagram of water[14]. We designed our plating cell with an angle between the injecting end (lower) and the outlet end (figure 2.3). The hydrolyzed H_2 bubbles could be pushed to the outlet end due to the slightly lower hydrostatic pressure there. With this design, it was possible to reduce the effects of hydrolysis H_2 for a smoother plating procedure inside the sub-micron channels of the AAO membranes. In conclusion, we realized Ni:Fe co-deposition in sub-micron scale channels.

The length of the deposited nanowires, as well as the aspect ratio, could be easily controlled
by the total deposition time.

Table 2.1   Optimized electrolyte bath used in my dissertation for Ni:Fe soft magnetic
nanowire fabrication

	comments	
composition (g/L)	$NiSO_4.6H_2O$	200
	$FeSO_4.7H_2O$	9
	$NiCl_2.6H_2O$	5
	Boric Acid	25
	Saccharin Sodium	3
pH	Using 1 M HCl adjust to 4	
deposition mixing	gentle	
pulse galvanostatic parameters	4 V; 1 kHz; Gate wave, bottom 0 V, peak 4 V;	
	Duration time, on : off = 1 : 1 per pulse	
others	solution need to be mixed overnight before using	
	to minimize the oxidization, N2 purge is necessary	
	two electrode system, Cu as working and Pt as counter electrode	
	three electrode system, Cu as working, Pt as counter electrode, and Ag wire as reference electrode	
	Fe^{2+} can be oxidized to Fe^{3+} easily, so use a fresh solution	
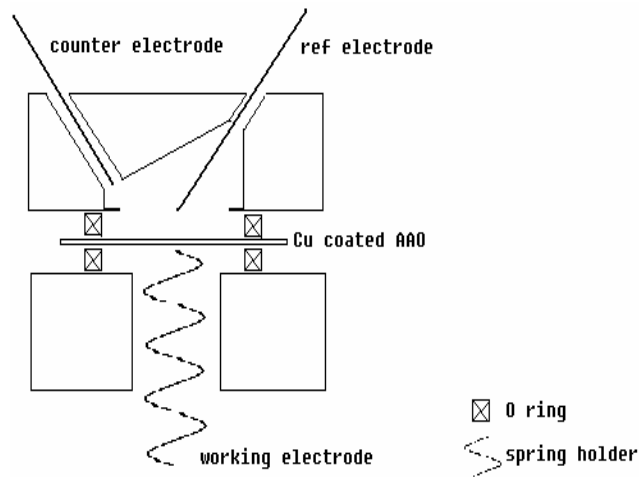
Figure 2.3, Schematic of the electro-deposition cell design for Ni:Fe nanowire deposition. It is a three electrode plating system with a Au counter electrode, a Ag reference electrode, and a steel spring pressed Cu layer at the back of a AAO membrane as a working electrode. The fresh electrolyte was pumped through the lower end and then pushed out from the higher outlet end. There are two "O" rings to seal and separate the deposition chamber from the outside.

Commercial AAO membranes were purchased from Whatman[®] with open channels of different sizes. I sealed one side of the membrane with a thin layer of Cu, which served as a working electrode as well. Different target materials such as Cu, Ag, and Au were all used in a thermal deposition chamber to produce a 300 nm conductive metal layer on one side of the AAO. Due to the inner stress generated by the coated metal films, I also deposited a 10-20 $\overset{o}{A}$ Cr layer between the AAO membrane and the sealing metal layer to prevent the peeling off of the deposited metal layer. A custom made holder was hung inside the chamber at a 45° angle to the metal target holder plane for better sealing. SEM measurements (figure 2.4) and diffusion tests (one side of the membrane containing Ag^+ solution and the other side containing Cl^- will remain clear only when the two sides are perfectly separated) both

showed a soundly sealed surface after thermal deposition of 300 nm of metal to an AAO membrane with 200nm channels.

In my electrodeposition system the plating speed may be affected by several issues, especially the diffusion of the hydrogen bubbles and the metallic ions. By increasing the electrolyte flow speed, we achieved a more stable growth speed (typically, 1-2 μm / 10 min). Worthy of notice is the fact that the optimized electrolyte bath (determined by the screening methods mentioned earlier on a macroscopic Cu sheet) did not produce the same plated film composition when adopted for nanowire growth. The composition of plated nanowires changed to Ni:Fe ≈ 90:10 (insert of figure 2.6) instead of the original Ni:Fe ≈ 80:20 (figure 4.11) of the plated films on a macroscopic Cu sheet. I believe this is related to complicated kinetic effects such as metallic ion diffusion, hydrogen formation and diffusion, local pH variance in a confined environment. Subsequently, Cu, Cr, Ag were all able to be easily etched away by wet chemical solutions like Cu^+, commercial Cr etchant and HNO_3.
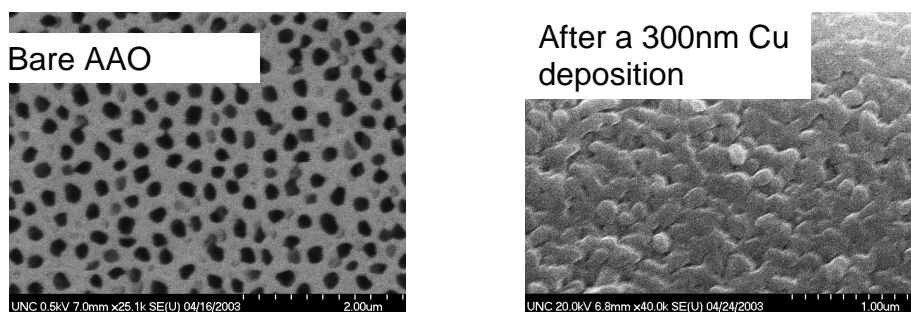
Figure 2.4, SEM images of a 200 nm channeled AAO membrane with Cu deposition. AAO membrane was hung at 45° to the metal target boat plane.

2.2.3 Half and Full Released Ni:Fe Nanowires

After deposition, the channels inside the AAO membrane were filled with Permalloy nanowires. The appearance of the membranes changed depending on how much Permalloy was deposited inside. The final membrane was clearly magnetic. Deposited nanowire arrays typically exhibited a high number density of up to 10^9, which makes them a good candidate for a high density magnetic memory device[15].

Half-etched deposited AAO membranes formed a structure like a "wheat field" with many metal nanowires extending beyond the remaining template. Researchers have demonstrated the possibility of using this structure to improve electrical contact between nanowire-containing membranes and substrate metal surfaces[1]. Al_2O_3 was easily etched away by 2M NaOH. I inserted the deposited AAO membrane sideways in a 2M NaOH bath. The level of the NaOH solution was adjusted so as to only submerge one third of the membrane. Due to the good wetting, the NaOH solution formed a wetting film with a thickness gradient along the membrane surface. Without external agitation, a gradient in the degree of etching along the membrane occurred. This was an efficient way to obtain SEM images of nanowires in their densely packed form.

Figure 2.5 is an image of a half-etched deposited AAO membrane. Two issues need to be noted:

1. The nanowire pattern is strictly a copy of the template. Better self-assembled AAO templates will lead to more crystal-like standing nanowire arrays.

2. The number density of the nanowire array as deposited is around 10^8-10^9/cm^2 which copies the channel density of the AAO membrane used.

12
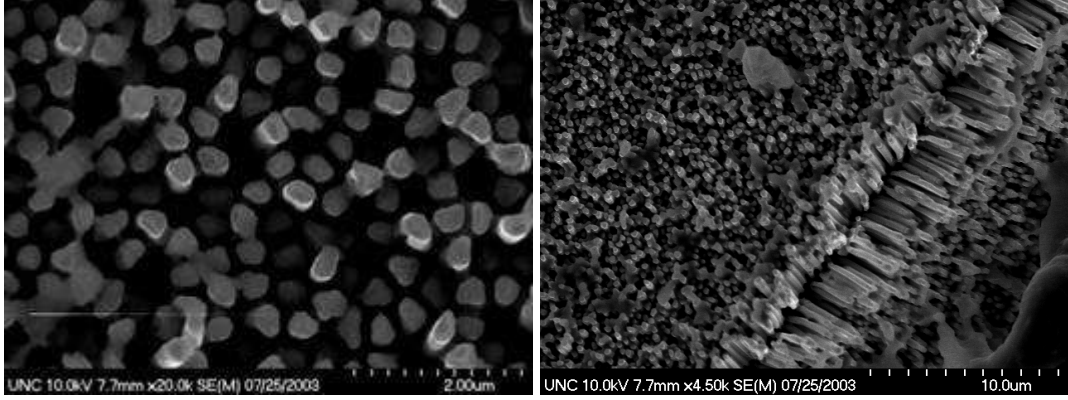
Figure 2.5, SEM images of half-etched Ni:Fe plated AAO membranes. Left, top view of a half etched plated AAO disc, leaving nanowires standing out from their template; right, side view of the same disc. The nanowire number density is around 10^9/cm^2.

My research requires released magnetic nanowires for actuation purposes. To get free released magnetic nanowires, the Cu working electrode (also serving as a sealing layer) was etched away by saturated ammonia, while the AAO and the deposited Permalloy nanowires were preserved. After NaOH etching and rinsing with DI water, we obtained an aqueous nanowire suspension. Unless noted otherwise, all the magnetic nanowires used in this dissertation will be these 200 nm wide, variable length Ni:Fe nano structures. According to the literature [16] [17], magnetic nanowires of these dimensions are not single-domain structures. Research has shown that similar magnetic materials have an easy magnetic axis in the longitudinal direction. According to the Stoner and Wolfarth model [18], the total energy for an ellipsoid of revolution is the sum of magnetization and shape anisotropy energies:

$$E = -BM_s \cos\phi - \frac{\mu_0 M_s^2}{2}(N_b - N_a)\cos^2(\phi - \theta) \text{ (5)}$$

where ϕ is the angle between the field and the magnetization moment of the rod and θ is the angle between the field and the easy axis of the rod; M_s is the saturation magnetization; N_b and N_a are demagnetizing factors along width and longitude directions respectively. For a

high aspect ratio nanowire, N_b-N_a = 0.5 [19]. The exact solution for ϕ obtained by setting

$\dfrac{dE}{d\phi} = 0$ indicates that the approximation

$$\phi \cong \theta * \left[1 + \frac{B}{\mu_0 M_s (N_b - N_a)} \right]^{-1} \quad (6)$$

is valid for small B[20]. Since $\lim_{B \to 0} \dfrac{\phi}{\theta} \to 1$, ϕ is commensurate to θ over a wide range of 0

$< \theta < \pi/2$ as long as the field strength is low. For example B = 0.03T will introduce into ϕ

only a 3% bias away from θ (M_s = 8.33 x 10^5 A/m). So it is reasonable to treat my high

aspect ratio magnetic nanowires as magnetic dipoles oriented along the longitudinal axis in

my experimental setup, which operates below 0.03T in the sample area.

Figure 2.6, SEM image of a released Ni:Fe nanowire. The radial dimension is around 200 nm and the length is about 9 μm. The insert is the EDAX measurement of an etched Ni:Fe plated AAO membrane.

2.3 Properties of Magnetic Nanowires and Nanowires of Other Materials

EDAX is a powerful tool for exploring the composition of my magnetic nanowires. Though typically not viewed as an accurate quantitative method, it is reasonable to assume that the elemental analysis will give us the results with accuracy no worse than 5% with heavy metals. My measurements showed that the nanowires were alloy of Ni:Fe in an atomic ratio of 90:10.

It is interesting to know the magnetic property of an individual nanowire. The sensitivity of the commercially available superconducting quantum interference device (SQUID) is no higher than 10^{-7} emu. The magnetic moment of a single nanowire is in the range of 10^{-9} to 10^{-11} emu, two to three orders of magnitude smaller than the detection limit of the SQUID [21]. Another graduate student in our group, Tim Meehan, measured magnetic properties of a small piece of a Ni plated 200nm channel AAO membrane [22]. His plating procedure was very similar to mine and the AAO membrane was also from the same supplier. Based on the channel density, his calculation showed that the saturation magnetic moment per rod with the applied field oriented parallel and perpendicular to the rod axis respectively were $m_{\Uparrow} = 7.0 \cdot 10^{-13} Am^2$ and $m_{\perp} = 7.9 \cdot 10^{-13} Am^2$. There was no significant difference of the magnetization between the parallel and perpendicular orientations of the nanowires. He also applied a linear fit to obtain the remanence and the susceptibility of Ni nanowires. The results showed Ni nanowire is "soft" magnetic material with coercive field 100G and reaches 90% saturation at 4000G. To get a sense of the "softness" of my Ni:Fe nanowires and at what field strengths they are saturated, I also did a quick measurement on a Ni:Fe plated AAO membrane without normalization of volume or mass. Although the data was too sparse to be exact, it is obvious that the coercive field of my Permalloy nanowire was no more than 100G and the material reached 90% saturation at 200G. Therefore, under most of my magnetic

manipulation experiments, it was safe to treat a pre-saturated Ni:Fe nanowire as a constant dipole as long as:

1. the initial field strength was stronger than 200G;

2. there was no de-magnetization procedure applied.

Due to the ferromagnetic nature of the Permalloy nanowires, there is a remanence left in each nanowire even without an external magnetic field. The remanence field led to the head-end configuration of nanowires when dropping a nanowire suspension on a flat substrate (figure 2.7) in the absence of a strong external magnetic field.
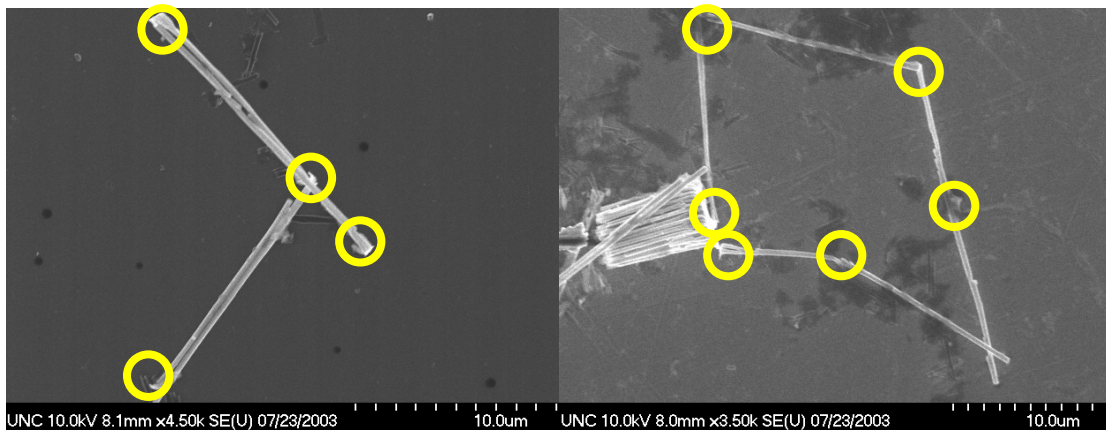
Figure 2.7, SEM images of Ni:Fe nanowires adopted a south-north or "head-end" chain configuration. The yellow circles indicate the "head-end" configuration. Noticeable here is that, due to the nanowire growing from an uneven Cu sealing layer, the feet (end) of nanowires are not very regular and are easy to distinguish from the head.

The template plating method was used for other metal nanowires in our lab as well, such as Au, Ag, Cu, Co, and Ni. Also of interest are segmented nanowires composed of more than one element. I synthesized Co nanowires capped with 1 μm Ag in a custom made AAO membrane with 100 nm channels as well (thanks to Dr. Lei Zhang's help). The capped Ag is

a good surface plasmon material which may introduce interesting optical properties into the final product. TEM images (figure 2.8) showed that I have successfully resolved the hydrolysis problem in AAO templates with channels less than 100 nm. The electron diffraction pattern of the Ag-capped portion in a TEM revealed the crystal nature of the deposited Ag nanowires (figure 2.8).
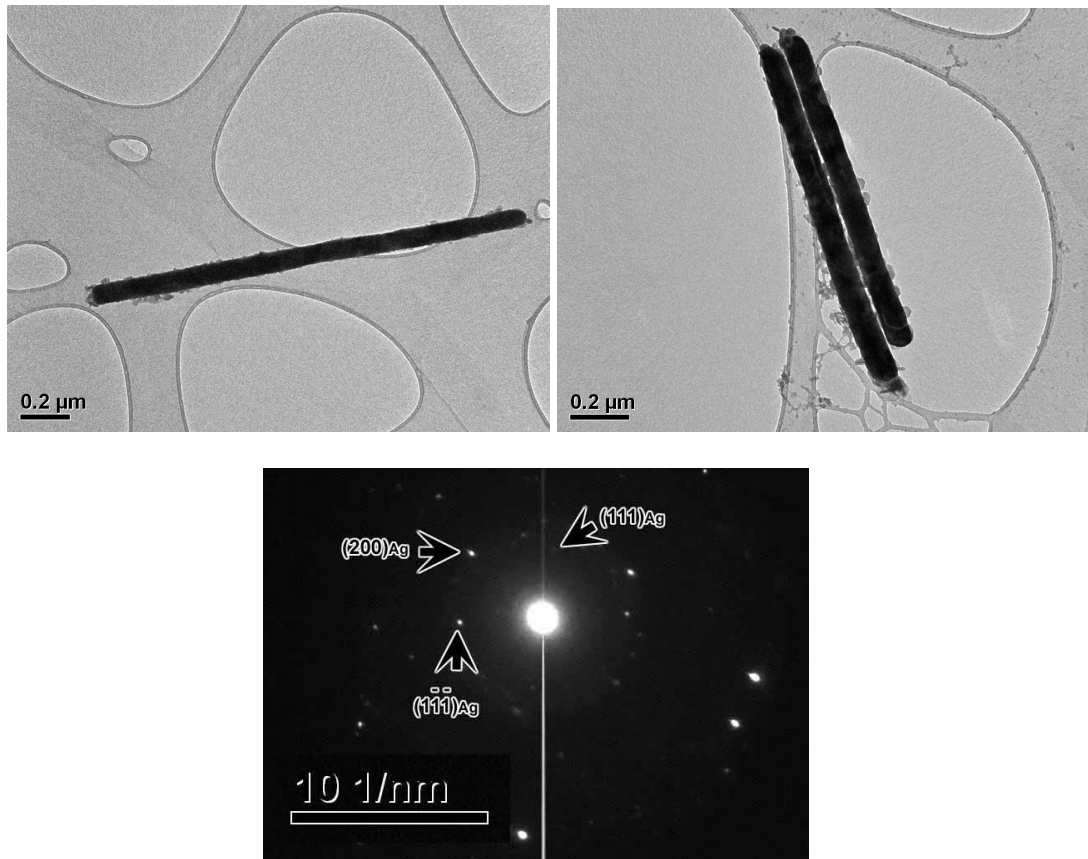
Figure 2.8, TEM images and electron diffraction patterns of Ag capped Co nanowires from a home made AAO membrane. The nanowire diameter is around 100nm.

2.4   References

1.   Yu, S.F., et al., *Nano wheat fields prepared by plasma-etching gold nanowire-containing membranes.* Nano Letters, 2003. **3**(6): p. 815-818.

2.   Vila, L., et al., *Growth and field-emission properties of vertically aligned cobalt nanowire arrays.* Nano Letters, 2004. **4**(3): p. 521-524.

3.   Teo, K.B.K., et al., *Field emission from dense, sparse, and patterned arrays of carbon nanofibers.* Applied Physics Letters, 2002. **80**(11): p. 2011-2013.

4.   Moser, J., et al., *Individual free-standing carbon nanofibers addressable on the 50 nm scale.* Journal of Vacuum Science & Technology B, 2003. **21**(3): p. 1004-1007.

5.   Whitney, T.M., et al., *Fabrication and Magnetic-Properties of Arrays of Metallic Nanowires.* Science, 1993. **261**(5126): p. 1316-1319.

6.   Schwarzacher, W., et al., *Metal nanostructures prepared by template electrodeposition.* Journal of Magnetism and Magnetic Materials, 1999. **199**: p. 185-190.

7.   Wang, J.B., et al., *Structure and magnetic study of Fe1-xNix (0 < x <= 0.32) alloy nanowire arrays.* Journal of Physics D-Applied Physics, 2001. **34**(24): p. 3442-3446.

8.   Chen, Q.L., et al., *Fabrication and electrochemical properties of carbon nanotube array electrode for supercapacitors.* Electrochimica Acta, 2004. **49**(24): p. 4157-4161.

9.   Lister, T.E. and J.L. Stickney, *Atomic level studies of selenium electrodeposition on gold(111) and gold(110).* Journal of Physical Chemistry, 1996. **100**(50): p. 19568-19576.

10.   Rieger, P.H., *Electrochemistry.* 1987, Englewood Cliffs, N.J.: Prentice-Hall. xvii, 508.

11.   Liu, Q.F., et al., *Fabrication and Mossbauer study of arrays of Fe1-xNix nanowires.* Acta Physica Sinica, 2001. **50**(10): p. 2008-2011.

12. Liu, Z.W., et al., *Plasma dry etched p-silicon micromolds for permalloy microstructure array electrodeposition.* Surface & Coatings Technology, 2000. **131**(1-3): p. 239-242.

13. Popov, B.N., K.M. Yin, and R.E. White, *Galvanostatic Pulse and Pulse Reverse Plating of Nickel-Iron Alloys from Electrolytes Containing Organic-Compounds on a Rotating-Disk Electrode.* Journal of the Electrochemical Society, 1993. **140**(5): p. 1321-1330.

14. http://www.wellesley.edu/Chemistry/chem120/pour.html.

15. Thurn-Albrecht, T., et al., *Ultrahigh-density nanowire arrays grown in self-assembled diblock copolymer templates.* Science, 2000. **290**(5499): p. 2126-2129.

16. Strijkers, G.J., et al., *Structure and magnetization of arrays of electrodeposited Co wires in anodic alumina.* Journal of Applied Physics, 1999. **86**(9): p. 5141-5145.

17. Tanase, M., et al., *Magnetotransport properties of bent ferromagnetic nanowires.* Journal of Applied Physics, 2003. **93**(10): p. 7616-7618.

18. Stoner, E.C. and E.P. Wohlfarth, *A Mechanism of Magnetic Hysteresis in Heterogeneous Alloys (Reprinted from Philosophical Transaction Royal Society-London, Vol 240, Pg 599-642, 1948).* Ieee Transactions on Magnetics, 1991. **27**(4): p. 3475-3518.

19. Osborn, J.A., *Demagnetizing Factors of the General Ellipsoid.* Physical Review 1945 **11-12**: p. 351-358.

20. Evans, B., *78 Permalloy Rod in B-Field at Saturation*.

21. Tanase, M., *Ferromagnetic Nanowires: Field-Induced Self-Assembly, Magnetotransport and Biological Applications*. 2003 Johns Hopkins University.

22. Meehan, T., *Force quantification of magnetically driven nanoparticles*. 2006 University of North Carolina Chapel Hill.

CHAPTER 3 – Standing Ordered Nanowire Structures

3.1   Introduction

In Chapter 1, I discussed the potentials of mesoscopic actuators in different applications such as sensors, mixers, and functional coatings. Significant progress has been made in mesoscopic actuable device fabrication techniques. Traditionally, lithography has been used for sub-micron actuator fabrication [1-4], but the limited aspect ratio in the direction of the exposing beam and the high cost limit its application in many areas. Bottom up strategies have been gaining more interest in hopes of avoiding some of the shortcomings of lithography. A significant challenge is the ability to fabricate actuators through a bottom-up strategy. Self-assembly strategy is a common approach in the field of nano technology. Researchers have demonstrated many strategies for producing highly ordered sub-micron structures with static charges, interfacial stresses, chemical affinities, and magnetic forces. Specifically, nano spherical particles with static charges or magnetic dipoles are well-known to be building materials for self-assembled 2D or 3D structures such as lithography templates [3], photonic crystals [5], and exotic new materials [3] [6]. However, my research represents the first time that magnetic nanowires have been explored as a building material for patterned structures [7, 8].

The fabrication strategy described in this chapter is a significant step forward in the field of bottom-up actuator fabrication since it readily controls the standing nanowire array lattice structures without the help of any kind of lithography, while still being flexible enough to adjust wire-wire distance if required. One key concept here is the separation of the assembly steps from the fabrication procedures. I can manipulate free magnetic nanowires into desired patterns without being concerned with the template confinements. Researchers have already shown that a long-range force, even a very weak one, leads to a quasi-long-range ordered structure, a 1-D Wigner structure, instead of an amorphous structure [9]. I, for the first time, fabricated standing magnetic nanowire arrays with Wigner structures using a weak long-range magnetic force. The semi-periodic patterns of these free standing nanowires were tunable in-situ during the fabrication procedures. The adjustable mean lattice constant of the self-assembly patterns was controlled, measured, and shown to be theoretically predictable.

3.2   Theories on Tunable Self Assembled Wigner Structures

3.2.1   Formation of Close-packed Wigner Lattice Structures

Studies have shown that multiple dipoles (like electrons, plasma clouds or, in our case, magnetic dipoles) inside a radially symmetric potential confinement will self-assemble in closely packed ordered patterns, and specifically, it is well known that paramagnetic particles form a semi-periodic lattice under suitable magnetic confinement [5, 10-14]. However, the use of ferromagnetic nanowires to form predictable super-lattice structures has not been reported.

21

The permalloy nanowires used in this dissertation were ferromagnetic (Chapter 2). Similar to paramagnetic particles, they can form close-packed patterns in a magnetic field with a parabolic profile. Before discussing this pattern based on scaling arguments, it is interesting to see the visualized simulated self assembly patterns of multiple magnetic nanowires based on a Monte Carlo simulation.

The Monte Carlo simulation method I used here was first introduced by Nicholas Metropolis [15, 16] and then applied to a 2-D plasma system [17]. If we know the positions of N particles in a finite space, it is easy to calculate the potential energy of the whole system. I simplified the simulation by treating my magnetic nanowire system as N identical magnetic dipoles starting from a perfect hexagonal lattice in a parabolic-shaped magnetic field, $E = A+(x^2+y^2)/B$, where A and B are two parameters defining the shape of the magnetic field, x and y are the dimensionless 2-D coordinates, and E is the dimensionless field potential.

If we assume the balanced dipole-dipole distance is much larger than the nanowire radial size, we can simplify the pair-interaction between these nanowires as,

$$E_{\text{int}} = \frac{\mu_0}{4\pi} \sum_{i<j} \frac{M_i M_j}{\left|r_i - r_j\right|^3} \quad (1).$$

Here, M_i, r_i are dipole strength and position respectively. The field energy is then

$$E_{field} = \frac{\mu_0}{4\pi} \sum_{i=1}^{N} M_i B(r_i) \quad (2).$$

The energy of the whole system can then be written as,

$$E = E_{\text{int } er} + E_{field} = \sum_{i=1}^{N} MB_i + \frac{\mu_0}{4\pi} \sum_{i<j} \frac{M^2}{\left|r_i - r_j\right|^3} \quad (3).$$

In 2D case, the new position S_1 is given as,

$$X \to X + \alpha\xi_1$$
$$Y \to Y + \alpha\xi_2 \quad (4)$$

Here the parameter α is the maximum allowed displacement, and ξ_1, ξ_2 are random numbers between -1 to 1. This means the movement of any particle in my simulation is equally likely to be anywhere within a square of α^2. For each move, I calculate the energy change ΔE. If $\Delta E < 0$, I accept this new position due to its lower energy; if $\Delta E > 0$, the move will be taken based on the comparison between a new random number $\xi_3 \in [0,1]$ and the probability $\exp(-\Delta E/kT)$. When $\xi_3 < \exp(-\Delta E/kT)$, the new position is accepted and when $> \exp(-\Delta E/kT)$, the old position is retained. ξ_3

The simulated dipole pattern shown in figure 3.1 exhibits a hexagonal feature.
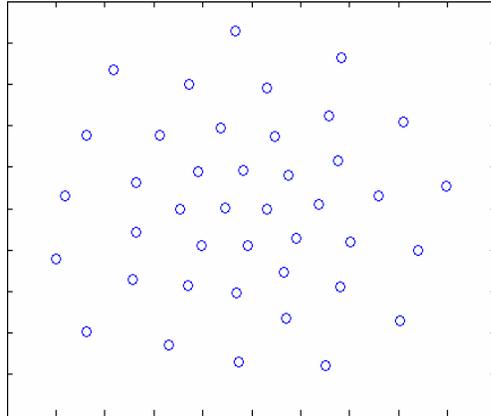
Figure 3.1, A self-assembled Wigner lattice structure of ferromagnetic dipoles from Monte Carlo simulations. The dimensionless simulated result is based on uniform ferromagnetic dipoles in a magnetic field with an arbitrary parabolic profile.

Besides ferromagnetic nanowires, I studied the case of multiple paramagnetic spheres in a magnetic field with a parabolic profile to further understand this assembly mechanism. Ferromagnetic particles behave as superparamagnetic entities if they are smaller than a

minimum single domain size at a specific temperature. The characteristic coercive field and the remanence in the hysteresis loop (dashed loop in figure 3.2) of bulk ferromagnetic materials will not appear in an ideal superparamagnetic material (solid loop). Under relatively low magnetic field strength, when the majority of the atomic dipoles are not aligned with the field, paramagnetic materials exhibit magnetization according to Curie's Law,

$$M = C\frac{B}{T} \tag{5}$$

where M is the resulting magnetization, B is the magnetic flux density of the applied field, T is absolute temperature, and C is a material-specific Curie constant. For the simulation of superparamagnetic beads, the only difference is that, instead of a $M = C\frac{B}{T}$ constant, in the Permalloy nanowire case. Again, this simulation was only for the purpose of a qualitative comparison, and was done on an arbitrary scale. The similarity between the simulated patterns in both of the ferromagnetic and the paramagnetic cases are obvious, both showing a hexagonal structure (figure 3.3).
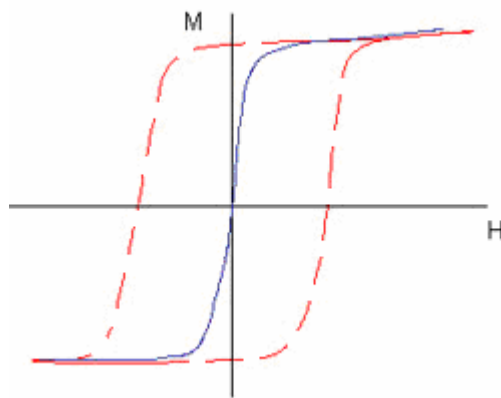
Figure 3.2, Schematic of typical hystersis loops of ferromagnetic materials (dashed line) and paramagnetic materials (solid line).
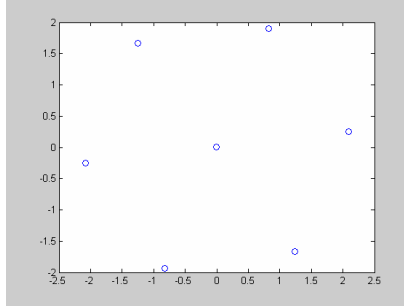
Figure 3.3, A self-assembled Wigner lattice structure of paramagnetic spheres from Monte Carlo simulations. The dimensionless simulated result is based on uniform paramagnetic dipoles in a magnetic field with an arbitrary parabolic profile.

3.2.2   Mean Lattice Constant Manipulation

One unique feature of my magnetic self-assembly procedure as compared to other self-assembly techniques is that the dipole-dipole distance of the final self-assembled patterns is tunable [11-13]. The mean lattice constant correlates to the magnetic field strength by a simple power law relation as revealed below.

There are two methods of calculating the mean scale value a_0 from a 2D position coordinate matrix. In the first, by using a pair distribution function (PDF), it is possible to find the mean dipole-dipole distance from the first peak position. The second is by triangulation. I adopted Delaunay Triangulation of 2D data for its straightforwardness (figure 3.4). One of its properties is that the edges of every triangle do not contain any other data point [18].
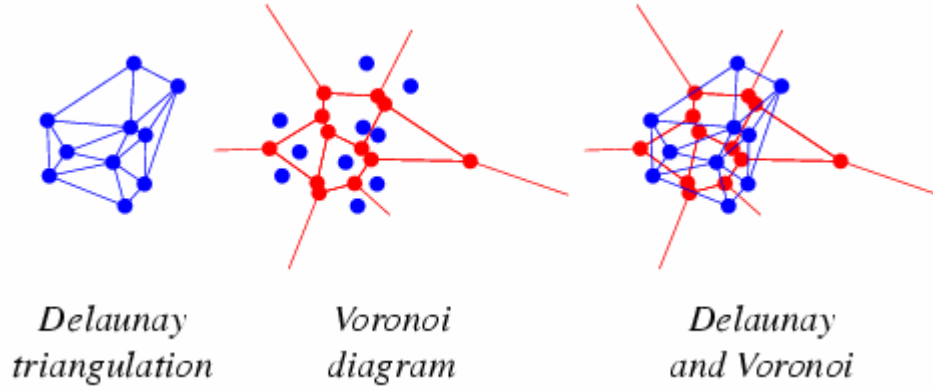
Figure 3.4, Demonstration of the Delaunay Triangulation process and its relation to Voronoi diagram in 2D (copy from [18]).

Based on a custom modified, double precision arithmetic, open executable C++ package by Hua yang (which has been tested extensively for its correctness) which reads a file of point coordinates in 2-D, I produced a PostScript file containing an image of the Delaunay Triangulation of the data points. I also obtained the mean lattice constant, which is calculated by

$$a_0 = \frac{1}{N}\sum_i^N L_i$$ (6).

Here a_0 is the mean lattice constant, N is the particle number and L_i is

$$L_i = \sqrt{(X_{i+1} - X_i)^2 + (Y_{i+1} - Y_i)^2}$$ (7).

The X and Y values are the readouts from the Delaunay Triangulation.

The ferromagnetic dipole configuration is obtained from the coordinate dependent part of the Hamiltonian, which can be written as,

$$H \approx -C_1 \sum_{i=1}^N MB_{oI} r_i^2 + \frac{\mu_0}{4\pi}\sum_{i<j} \frac{M^2}{\left|r_i - r_j\right|^3}$$ (8)

26

based on equation (3) and an assumed external magnetic field with a parabolic profile

$B = B_{oI}(C_o - C_1 r^2)$ (as in equation 11). Here r is the radial distance to the longitudinal axis of the tapered core, B_{oI} is the field strength at the center of the sample plane, and C_0 and C_1 are two constants defining the parabolic shape of the field. Scaling considerations yield a power law relationship

$$a_0 \propto (\frac{\mu_0 M}{B_{0I}})^{\frac{1}{5}} \quad (9)$$

In the ferromagnetic nanowire case (M being a constant), the dimensionless lattice distance scale a_0 is tunable by tuning field strength B_{oI} with a simple scaling law $a_0 \propto (\frac{1}{B_{0I}})^{\frac{1}{5}}$.

3.3   Experiments with Standing Nanowire Structures

3.3.1   Self Assembled Standing Nanowires in Liquid

Figure 3.5 outlines the setup for nanowire array fabrication. Through a custom-designed magnetic field with a parabolic profile, nanowires first aligned along the magnetic field direction. Then, the convergent magnetic gradient pulled the nanowires toward the tip position. During the entire procedure, the nanowires were relatively parallel with each other and would repel each other when they were too close. The competition between the attractive and the repulsive forces would lead to a balanced structure.

The magnetic field at the sample area was realized by a solenoid with a magnetic core at the center. The core material is soft iron with a high saturation field strength and small remanence. The core was designed with a sharp tapered tip (6 mm in diameter and 15 mm in height) to produce the desired magnetic field. Measurements showed the tip end was a 50 μm

diameter flat plane. The magnetic field strength at the sample area (100 μm above the cone tip of the home-made solenoid) was simulated using FEMLAB (Comsol Group) with MATLAB (Mathworks) as (figure 3.5)

$$B = 0.196 - 6.5 * 10^6 r^2 \ (|r| \leq 100 \mu m) \ (10)$$

$$\text{or } B = B_{oI}(C_o - C_1 r^2) \ (|r| \leq 100 \mu m) \ (11).$$

Here r is the radial distance to the longitudinal axis of the tapered core, B_{oI} is the field strength at the center of the sample plane, C_0 and C_1 are two constants defining the parabolic shape of the field. The input is 300 Amp-turns. Both experiments and simulations showed B_{oI} was linearly related to the surface current density of the solenoid with moderate current inputs (0.1 A to 2 A). Simulations also showed that the parabolic shape of the magnetic flux density would not change in this input range. In other words, C_0 and C_1 are constants in the linear region. This parabolic potential can exert a vertical force to drive nanowires down toward the solenoid tip and a spherical contractive confinement to densely pack them at the same time.

Self-assembled nanowire arrays were planted in a soft polymer supporting layer for actuation purposes which are discussed in detail in the next chapter. An aqueous nanowire suspension was dropped inside a PDMS well which was placed on top of an uncured polymer layer as in figure 3.5. The substrate was a #0 glass cover slide which had undergone an intensive O_2 plasma treatment. By controlling the spin speed, a thin layer (<5 um) of uncured Sylgard 184 (Dow Corning) PDMS mixture was coated on this cover slide. It is worth noting that to produce PDMS thin films without bubbles as defects, the PDMS pre-mixture should undergo an intensive vacuum de-gassing procedure. Stable self-assembled patterns appeared within seconds after we turned on the assembly field. During this time, the polymer mixture

was still uncured and worked as a lubricant between the nanowires and the cover slide, allowing the nanowires to move laterally. By setting the sample on a 70 °C hot plate overnight, the roots of the free standing nanowire array were cured inside the PDMS film. To limit the water evaporation, a layer of mineral oil or a lid on the sample was necessary. For better adhesion between the polymer mixture and the cover slide, a layer of HMDS (spin-coated with 4k rpm for 50 s) was applied beforehand. In our moderate magnetic fields, typically no more than 0.2T, these magnetic dipoles oriented parallel with each other and stood perpendicular to the polymer substrate. Figure 3.6 is a top view image of this patterned structure taken by a CCD camera. Here each black dot is a standing nanowire pointing toward the viewer.
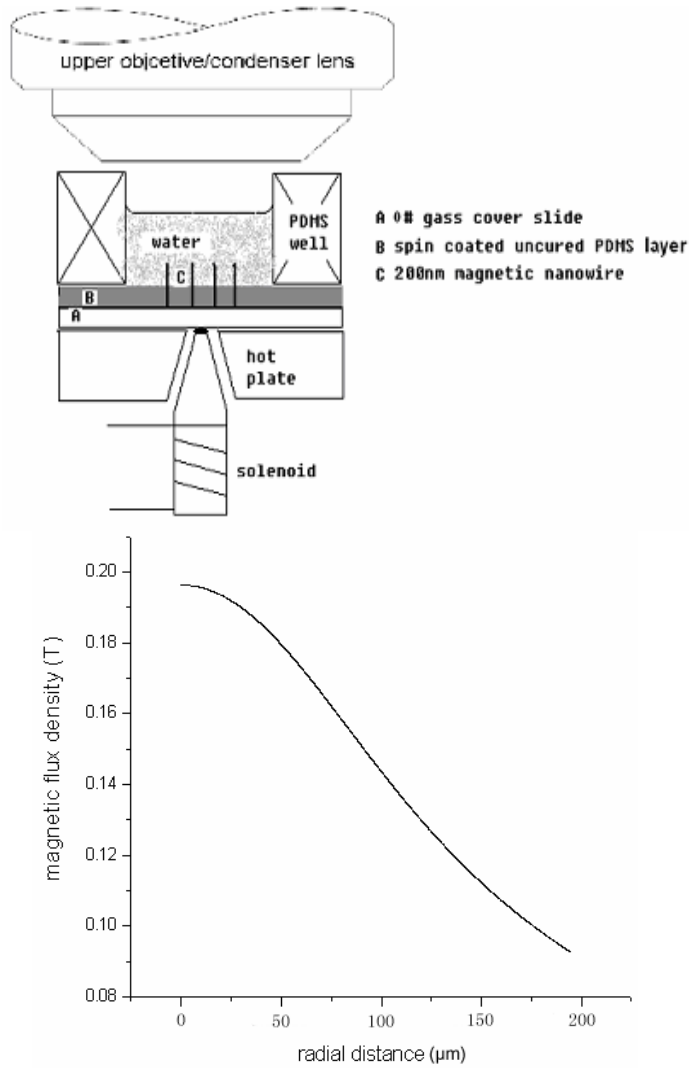
Figure 3.5, Top, schematic setup for standing magnetic nanowire device fabrication. The solenoid was made of a lead iron core (15 mm long tapered end on a 6 mm(diameter) X 40 mm(height) cylinder) with 300 turns of copper wire. A hot plate with a thermal couple feed back control was used as sample holder. Through normal and lateral (not shown here) CCD video microcopy, self assembly fabrication procedures and the subsequent actuation were recorded; bottom, magnetic field at the sample plane (300A) as simulated by Femlab. In the sample area ($|r| \leq 100\mu m$), and with medium field strength (H < 0.2T), the magnetic field strength could be approximated by a parabolic confinement very well.
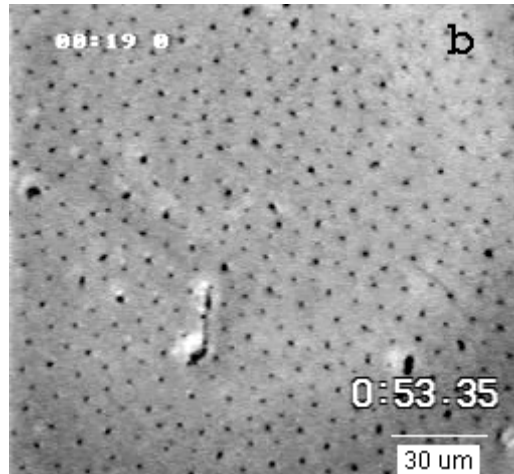
Figure 3.6, Top view of the self-assembled magnetic nanowire array rooted inside an uncured PDMS supporting layer. The black dots represent standing nanowires pointed toward the viewer. As seen in this image, there was some irregular debris still inside the sample. This might be one of the reasons that the lattice pattern was not very regular.

3.3.2 Standing Nanowire Arrays in Air

Many applications have been suggested for free standing structures. For example, researchers have already demonstrated that similar structures fabricated either by photolithography or by self-assembly of magnetic fluids can be used as surface property controllers, optical switches and separation devices[19] [20] [21].

I have tried to make self-assembled standing magnetic nanowire arrays in air to explore applications other than stirring in fluidic channels. CO_2 critical point drying is a routine process used to dry delicate structures. The water used for standing array fabrication was replaced with CO_2. And CO_2 has a critical temperature 35 °C at pressure 1200 psi [22]. Ethanol was used to aid the mixing between CO_2 and water. Therefore, if the water was replaced with liquid CO2 and the temperature was then raised to above the critical temperature, the liquid CO2 would change to vapor without surface tension effects which

31

might have otherwise distorted the morphology of my devices. However, CO_2/ethanol solution swells the PDMS, limiting the effectiveness of this critical point drying procedure. Other problems may also contribute to the poor survival rate of the nanowires after drying. For example, the poor wetting between the PDMS and the magnetic nanowires might not form a strong enough bond between the nanowires and the supporting PDMS layer. Therefore, I made standing devices using epoxy based photo resists AZP 4620 and Su-8 series as the supporting layer.

The details of the procedures were similar to the procedures that used PDMS. First, a thin layer of photo resist was spin-coated on a cover slide. The solvent in AZP 4620 dried out quickly during spin coating which might have made the uncured polymer film too hard to be penetrated by nanowires under moderate field gradient. Hence, I spin coated AZP 4620 with 4000 rpm for only 20 s in order to retain its softness. This coated cover slide was placed on the hot plate shown in figure 3.1. Because epoxy photoresists harden when heated, a subsequent heating at 70 °C would hold the roots of the patterned nanowires firmly. I used a solenoid to generate a magnetic field with a parabolic profile as described earlier in this chapter. Ideally the final standing devices would have mimicked the pattern shown in figure 3.6. Figure 3.7 are the SEM images of my best results using AZP 4620 as the supporting layer. The original close packed self assembly patterns seen in liquid were not shown because most of the nanowires were pulled down during the drying procedure. In most cases, only several individual nanowires survived, standing inside the SEM chamber. It is of interest to us to find appropriate supporting materials that can sustain the drying process while bonding strongly to the roots of the nanowires inside, in the future.

One interesting finding is that the standing nanowires on top of a rigid supporting layer like AZP 4620 and Su-8 never showed detectable actuation by an external actuating field around 0.2 T. This is further discussed in the next chapter.
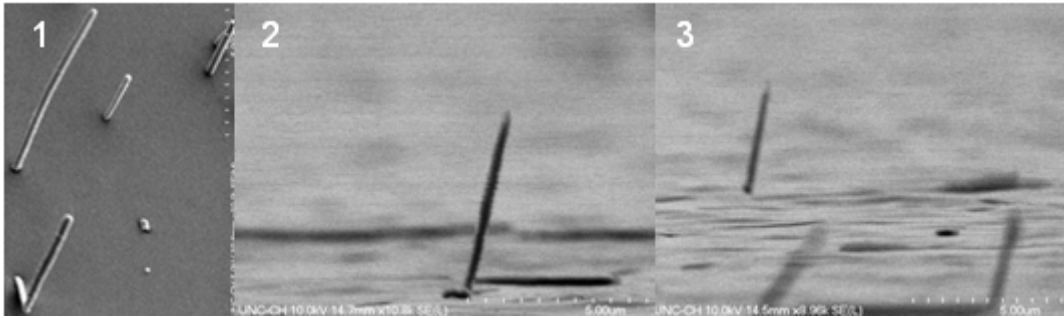
Figure 3.7, SEM pictures of magnetic nanowire standing from an AZP 4620 supporting film in vacuum. 1. SEM image from a 45 degree stage; 2. and 3., SEM images from a 90 degree stage.

3.4   Discussion

Figure 3.8 is another experimental self-assembly pattern of a much smaller number of magnetic nanowires than in figure 3.6. In Chapter 3.2, I have mentioned that the mechanism for this regular structure is due to the balance between a contraction force due to the external magnetic field and a repelling force due to the parallel magnetic dipoles.

Both experimental and simulated results (figure 3.8 and figure 3.1) showed a close packed Wigner lattice. Due to the fact that magnetic properties of a single nanowire were hard to measure, and the difficulties in measuring the magnetic field strength at this small scale, the simulation was only performed to show a qualitative similarity. The scales in the simulated data are arbitrary. Noticed "defects" (biased from a perfect hexagonal lattice structure) in the experimental results were caused by:

(1) the competition between two types of ordering, one into a radial symmetric shell lattice and the other into a Wigner lattice[10, 23];

(2) the distribution of rod length, and therefore the dipole strength. For example, in experiments, the strongest dipole will be attracted to the lowest energy position, repelling the near neighbors further away. This explained the reason why we sometimes saw longer dipole-dipole distance in the center instead of the shortest dipole-dipole distance predicted by the simulation.
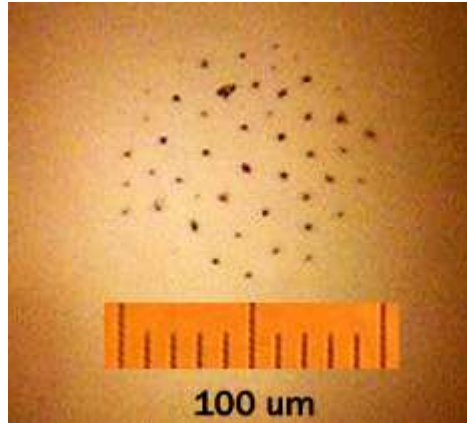
Figure 3.8, Self-assembled Wigner lattice structures of ferromagnetic dipoles in a magnetic field generated by a sharp taper-shaped solenoid from my experiments. Each black dot here represents a standing nanowire pointing toward the viewer.

Mean lattice constants of my experimental results were calculated by the exact method demonstrated earlier in Chapter 3.2. Figure 3.9 is the triangulation result of part of the figure 3.6.
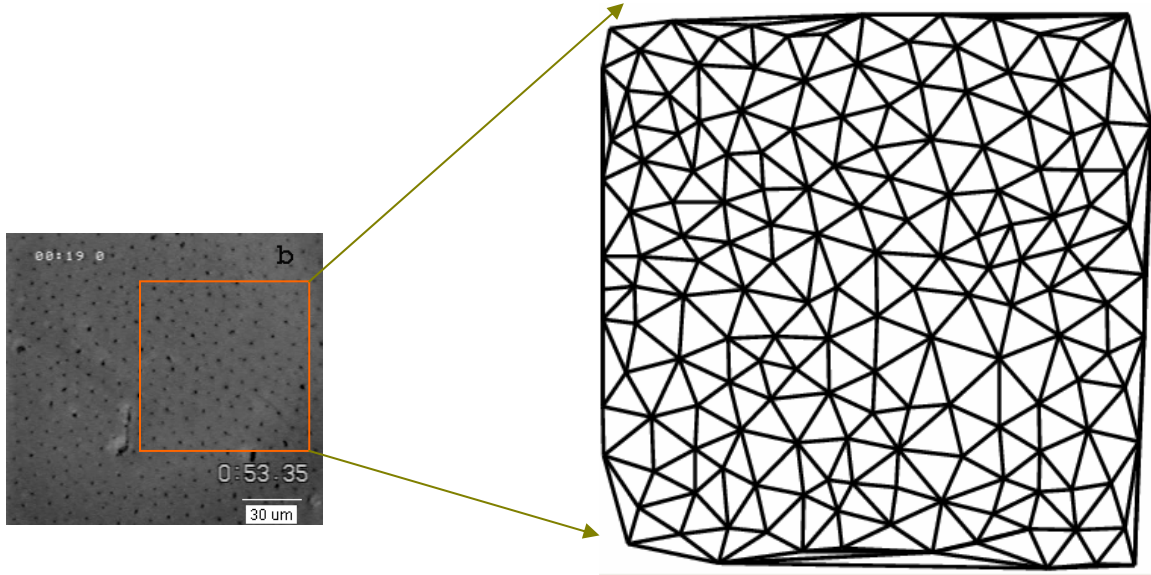
Figure 3.9, Delaunay Triangulation of part of a self-assembled pattern image in figure 3.2. Every apex position is where a standing nanowire is pointing toward the viewer.

I used a home-made solenoid as shown in figure 3.5 to assemble and fabricate ordered standing nanowire arrays. Scaling considerations of function (9) can be further derived to

$$a_0 \propto (\frac{\mu_0 M}{B_{0I}})^{\frac{1}{5}} \propto (\frac{\mu_0 M}{I})^{\frac{1}{5}} \quad (12)$$

as long as the B_{oI} and input current I maintain a linear relationship (where a_0 is a mean dipole-dipole distance scale, B_{oI} is the magnetic field strength at the radial symmetric center under current input I). In the ferromagnetic nanowire case (M being a constant), the dimensionless lattice distance scale a_0 is tunable by tuning field strength B_{oI}. So, in the ferromagnetic case, as long as the linear relationship between the input current I and the field strength B holds (in our set up, this corresponds to the current input from 0.1A to 2A X 300 turns), this simple -0.2 power law relation between the lattice constant scale a_0 and the input current I is valid. The linear Ln-Ln fit of the experimental mean lattice constant a_0 vs. input

current I showed a power law relation of -0.19 (figure 3.10), close to the theoretical calculation of function (9). It is worth noting that when the input current approaches 0 A, the remanence of the core will be the dominant component. The scaling law may likely be biased from this simple scaling argument in that case. This bias, due to measurement difficulties has not been studied.

In the paramagnetic case, unlike what was predicted by Golosovsky [23], we found the mean lattice constant of 2.8 μm paramagnetic beads also varied with changing current inputs. There is no simple scaling relationship such as that found in function (9) in the paramagnetic case. This is because M_i is a position dependant variable, and so there is no simple coordinate dependent Hamiltonian function such as (8) and the scaling argument in function (9) is no longer valid.

This scaling argument is a general guide for assembling mesoscopic ferromagnetic materials by parabolic magnetic confinement. By designing magnetic fields with desired profiles or artificially inducing pre-patterned magnetic lattices, we believe modifications of this self-assembly procedure can lead to more complicated assembled structures and lattice structures with a wider range of tunable lattice constants.
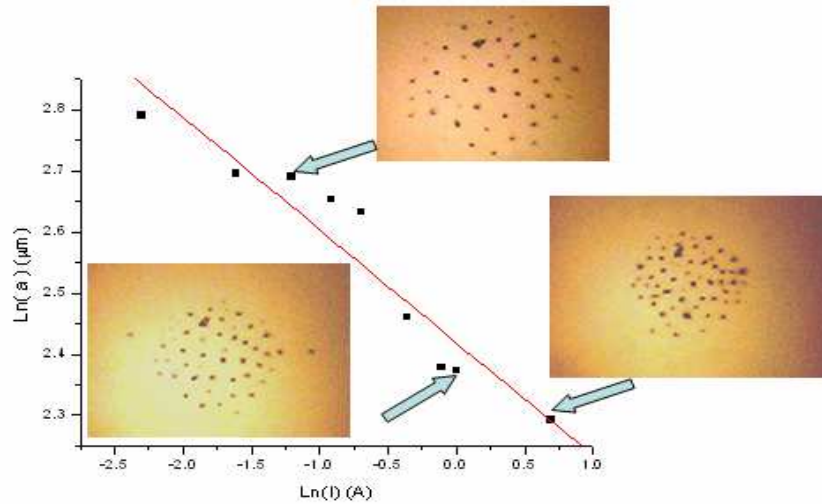
Figure 3.10, Dependence of the mean lattice constant on the current input. Ln-Ln plot of nanowire array average lattice distance vs. current input shows a -0.19 power law decay relation.

3.5   Summary

In this chapter I, for the first time, demonstrated and explained the possibility of self-assembling magnetic nanowires into a predictable close-packed Wigner lattice structure. The fundamental mechanism was interpreted based on the coordinate dependent part of the Hamiltonian of this system.

One unique advantage of the self-assembly technique introduced in this chapter is that the dipole-dipole distance of the final self-assembly pattern is tunable in situ. This is the first controllable self-assembly experiment demonstrated by using magnetic nanowires. I found that the mean lattice constant followed a simple power law relationship with the solenoid input current. My experiments demonstrated the possibility of using relatively simple methods to efficiently manipulate the self-assembly of sub-micron diameter nanowires for real applications. This may inspire the idea of using magnetic dipoles for more complicated and regulated structures.

3.6   References

1.   Fischer, P.B., et al., *10 Nm Si Pillars Fabricated Using Electron-Beam Lithography, Reactive Ion Etching, and Hf Etching.* Journal of Vacuum Science & Technology B, 1993. **11**(6): p. 2524-2527.

2.   Loechel, B., *Thick-layer resists for surface micromachining.* Journal of Micromechanics and Microengineering, 2000. **10**(2): p. 108-115.

3.   Martin, J.I., et al., *Ordered magnetic nanostructures: fabrication and properties.* Journal of Magnetism and Magnetic Materials, 2003. **256**(1-3): p. 449-501.

4.   Rajic, S., J.L. Corbeil, and P.G. Datskos, *Feasibility of tunable MEMS photonic crystal devices.* Ultramicroscopy, 2003. **97**(1-4): p. 473-479.

5.   Bizdoaca, E.L., et al., *Magnetically directed self-assembly of submicron spheres with a Fe3O4 nanoparticle shell.* Journal of Magnetism and Magnetic Materials, 2002. **240**(1-3): p. 44-46.

6.   Bal, M., et al., *Nanofabrication of integrated magnetoelectronic devices using patterned self-assembled copolymer templates.* Applied Physics Letters, 2002. **81**(18): p. 3479-3481.

7.   Chien, C.L., et al., *Electrodeposited magnetic nanowires: arrays, field-induced assembly, and surface functionalization.* Journal of Magnetism and Magnetic Materials, 2002. **249**(1-2): p. 146-155.

8.   Tanase, M., et al., *Magnetic alignment of fluorescent nanowires.* Nano Letters, 2001. **1**(3): p. 155-158.

9.   Wigner, E., *On the Interaction of Electrons in Metals.* Physical Review, 1934. **46**: p. 1002–1011.

10.   Bedanov, V.M. and F.M. Peeters, *Ordering and Phase-Transitions of Charged-Particles in a Classical Finite 2-Dimensional System.* Physical Review B, 1994. **49**(4): p. 2667-2676.

11. Golosovsky, M., Y. Saado, and D. Davidov, *Self-assembly of floating magnetic particles into ordered structures: A promising route for the fabrication of tunable photonic band gap materials.* Applied Physics Letters, 1999. **75**(26): p. 4168-4170.

12. Saado, Y., et al., *Tunable photonic band gap in self-assembled clusters of floating magnetic particles.* Physical Review B, 2002. **66**(19): p. -.

13. Saado, Y., et al., *Fabrication of artificial crystals with tunable lattice constant via self-assembly of floating magnetic particles.* Synthetic Metals, 2001. **116**(1-3): p. 427-432.

14. Xu, X.L., S.A. Majetich, and S.A. Asher, *Mesoscopic monodisperse ferromagnetic colloids enable magnetically controlled photonic crystals.* Journal of the American Chemical Society, 2002. **124**(46): p. 13864-13868.

15. Jorgensen, W.L., *Perspective on "Equation of state calculations by fast computing machines" - Metropolis N, Rosenbluth AE, Rosenbluth MN, Teller AH, Teller E (1953) J Chem Phys 21 : 1087-1092.* Theoretical Chemistry Accounts, 2000. **103**(3-4): p. 225-227.

16. Nicholas Metropolis, e.a., *Equation of State Calculations by Fast Computing Machines.* The Journal of Chemical Physics 1953. **21**((6)).

17. Gann, R.C., S. Chakravarty, and G.V. Chester, *Monte-Carlo Simulation of the Classical 2-Dimensional One-Component Plasma.* Physical Review B, 1979. **20**(1): p. 326-344.

18. http://mathworld.wolfram.com/DelaunayTriangulation.html.

19. Bao, G. and S. Suresh, *Cell and molecular mechanics of biological materials.* Nature Materials, 2003. **2**(11): p. 715-725.

20. Sanchez, C., H. Arribart, and M.M.G. Guille, *Biomimetism and bioinspiration as tools for the design of innovative materials and systems.* Nature Materials, 2005. **4**(4): p. 277-288.

21. Doyle, P.S., et al., *Self-assembled magnetic matrices for DNA separation chips.* Science, 2002. **295**(5563): p. 2237-2237.

22.   http://www.spaceship-earth.org/REM/cp-dry.htm.

23.   Golosovsky, M., Y. Saado, and D. Davidov, *Energy and symmetry of self-assembled two-dimensional dipole clusters in magnetic confinement (vol E 65, 061405, 2002).* Physical Review E, 2002. **65**(6): p. -.

CHAPTER 4 – Actuating Standing Nanowires by External Actuation Magnetic Fields

4.1   Introduction

As discussed in Chapter 1, one of my research interests is to precisely manipulate sub-micron magnetic nanowires in 3-D. Researchers have suggested using a single free floating magnetic nanowire or a chain of paramagnetic beads as stirrers in microfluidic systems[1] [2]. As far as we know there have been no successful attempts to use standing magnetic nanowires (as introduced in Chapter 3) as sub-micron actuators. These standing magnetic nanowire arrays could be actuated in a microfluidic device by a home-made three-dimensional magnetic force microscope (3DFM) system[3]. We believe they can find direct applications as active micro-mixers in microfluidic systems, surface property modulators or prototypical man-made rigid cilia.

Figure 4.1 demonstrates how these ideal structures could be used as mechanical actuators. The inherent magnetic dipoles of these ferromagnetic nanowires will align to an external magnetic field. By programming the magnetic field, these magnetic nanowires can realize complicated and time variant 3D orbits. In this chapter I describe the actuation experiments and discuss the mechanism of this actuation.
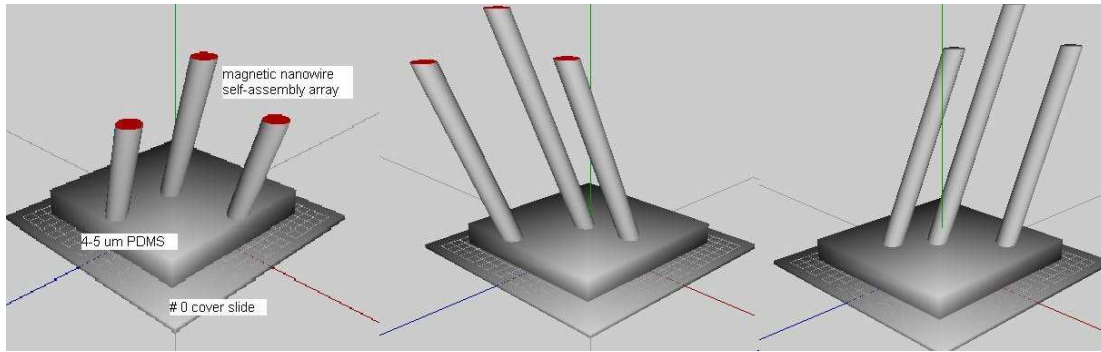
Figure 4.1, Schematic of patterned magnetic nanowire arrays working as actuable devices.

Our 3DFM combines a conventional optical microscope with a custom designed magnetic force subsystem. Forces are exerted through thin magnetic pole pieces by a set of computer controlled coils. The subsequent responses of magnetic tracers inside the sample cell are then able to be measured. This enables 3-D mechanical manipulations and measurements to be performed on specimens in a noninvasive way [3].

There are several advantages to using magnetic forces over other manipulation methods. For example, due to the fact that most of the samples relevant to biologists have very limited magnetic permeability, magnetic force exertion offers us the ability to treat samples without direct contacts. It offers the capability to exert larger forces than other noninvasive techniques, such as laser trapping, as well [3].

In our lab, we are attempting to explore forces related to many biological functions. Some of the experiments require maximum force, but not the ability to exert forces in three dimensions. Others require the application of a complex 3D torque to the sample while not requiring a large force. Obviously it is not possible to fulfill all these requirements with just one pole piece design. In this chapter I demonstrate the design and fabrication of thin Permalloy magnetic pole pieces.

The major challenge in the design of pole plates is spatial coexistence of imaging and the application of forces. In the 3DFM, the imaging and tracking subsystems share the same optical path near the specimen, both traveling through the objective and condenser lens. A typical high numeric aperture lens has very limited working distance (specifically, one of the 3DFM setups, *Hercules*, when using a water immersed Nikon 60X1.20 WI Plan Apo objective lens, has a total working distance of around 220 μm). Hence, thin film, high permeability magnetic pole pieces are necessary. Even though most of our pole pieces are laser cut today, we have developed a procedure to fabricate thin film pole pieces of different complex designs with superior accuracy that may find application in the future.

4.2   Materials and Methods

4.2.1   Design of Thin Film Magnetic Pole Pieces

One specific force subsystem is a so-called "6 pole design" which is under patent application by our group [4]. Figure 4.2 demonstrates the conceptual setup of this design, the purpose of which is for applying a time variant, 3D magnetic force and torque in the sample area. Six poles sit at the centers of the six faces of a cube in a face centered cubic (FCC) geometry. Thin magnetic films with high permeability can guide magnetic flux generated from a set of flat cores to the tapering tips. Complex, time variant magnetic fields can be realized by controlling magnetic flux in between the poles through a computer controlled interface program called "Blender" [5].

For a superparamagnetic sub-micron particle, the induced moment m is proportional to the incident field $m = \frac{\pi d^3}{2\mu_0}(\frac{\mu_r - 1}{\mu_r + 2})B$, where μ_0 is the permeability of free space, μ_r is the

relative permeability of the bead, and d is the diameter of the bead [6]. $F = \mu m \nabla B$, so the force applied by the pole tips is highly dependant on the field strength B. To get a better force response, the distance between these six pole tips was small, typically 200-400 μm away from each other according to the experimental requirements.

Optical axis (dashed line) is perpendicular to two planes, each containing three face-centered-cubic (FCC) points.

These points form a pair of parallel equilateral triangles with a cylindrical working volume between them.

Magnetic flux is conducted by thin film cores in two parallel planes to the pole tips having centers at the FCC locations
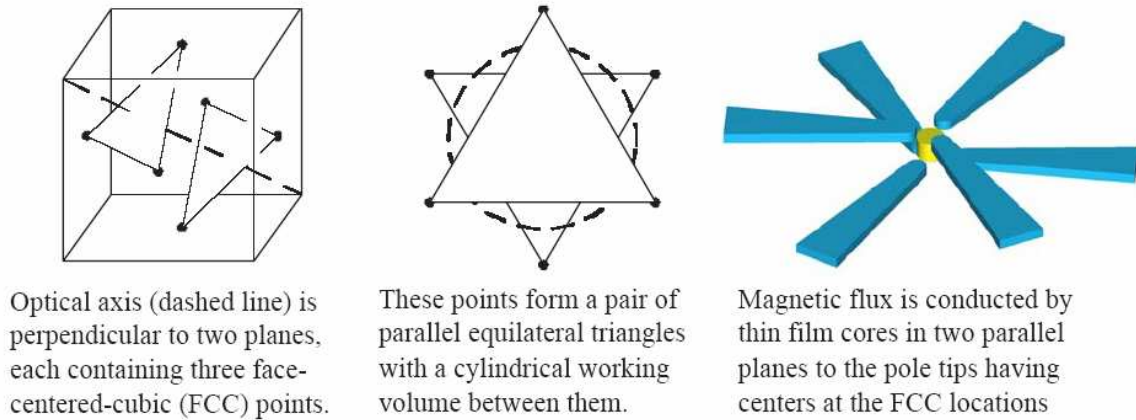
Figure 4.2, Schematic of the face-centered-cubic thin film magnetic pole pieces placement in two closely spaced parallel planes. (Published image from [3])

Another design was a so called 'comb' design which is illustrated in figure 4.3. The six feet guiding magnetic flux to the sample area can be divided into two groups. The comb design can apply force to relatively large area. Instead of applying the force in a 3D manner as described above, this design uses pole pieces in only one plane and exerts an essentially 2D magnetic force.
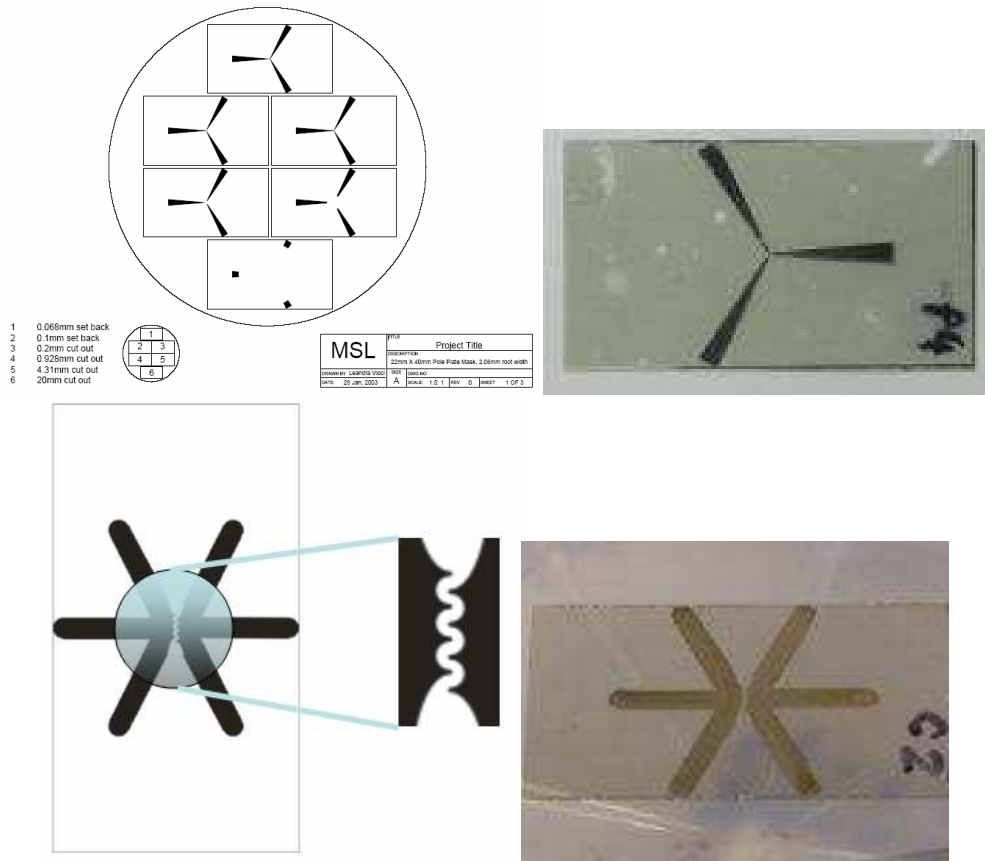
Figure 4.3, Designs for thin film magnetic pole pieces used in force subsystem in 3DFM. Top, 6-pole design and the actual fabricated pole piece; bottom, 'comb' design and the actual fabricated pole piece.

4.2.2 Magnetic Pole Piece Fabrication

The masks used for photolithography were designed in CorelDRAW[R], offered by the Corel Corporation. Due to our resolution requirements, we used a laser spray printing technique to print negative or positive designs on transparent sheets depending on what kind of photoresists were to be used. These transparent sheets act as the masks in contact mode

photolithography. Both the positive and negative photoresists were used for magnetic pole piece fabrication.

1.   negative tone photoresist NANO^{TM} Su-8 2000 series (MicroChem), near UV (350-400 nm); epoxy based resist, used for thick film MEMS application

2.   positive thick film photoresist AZP 4620

The fabrication procedures associated with each photoresist are very similar. Both were first spin-coated on a plasma treated surface (for AZP 4620, in order to improve the adhesion between the photoresist and the substrate, a Hexamethyldisilizane (HMDS) EtOH solution (kindly offered by MCNC-RTI with unknown concentration) was spin-coated at around 3000 rpm over 60 s prior to applying the photoresist. HMDS is widely used to form a strong bond to the surface by silylation process[7].). Then, after a careful pre-baking procedure, cover slides with photoresists were contact exposed with optimized dosages of near field UV radiation. Depending on the positive or negative nature of the photoresists used, complementary masks were chosen. A subsequent hard baking procedure was required especially for AZP 4620 for better mechanical properties and faster chemical reactions inside the polymer. After using suitable developer, and rinsing carefully, the templates were ready for electrodeposition [8].

In Chapter 2, I mentioned that electrodeposition is a common method for fabricating Micro-Electro-Mechanical Systems (MEMS). Bare glass is an insulating material. The successive plating of metal inside the template mentioned above requires coating a layer of metal prior to the plating procedure. We thermally evaporated 40 nm of Cu on the cover slide surface as a conductive layer with a 10 $\overset{o}{A}$ of Cr as an adhesive layer between the Cu and the glass. Not only does the inner stress between the thermally deposited Cu and glass need to be

released here, but the interfacial stress between the plated Permalloy and this Cu layer was also carefully released by adding organic additives. Typically, electro deposited Ni:Fe (80:20) alloy is a mixture of FCC and BCC polycrystalline material [9]. I noticed that without fine tuning of the chemical bath, the composition of the final magnetic plated film was not stable and the plated film did not adhere well to the substrate. By using some organic additives as stress releasers, using a pure Ni sacrificial anode, and screening through different electrolyte recipes, I deposited shiny Ni:Fe $\approx$ 80:20 permalloy films inside the templates (Chapter 2). The bonding strength between the plated film and its substrate was high. Even under intensive chemical and mechanical processing and usage, the final plated pole pieces would not peel off of the Cu substrate. Figure 4.4, shows the improved composition stability of the deposited Permalloy films.
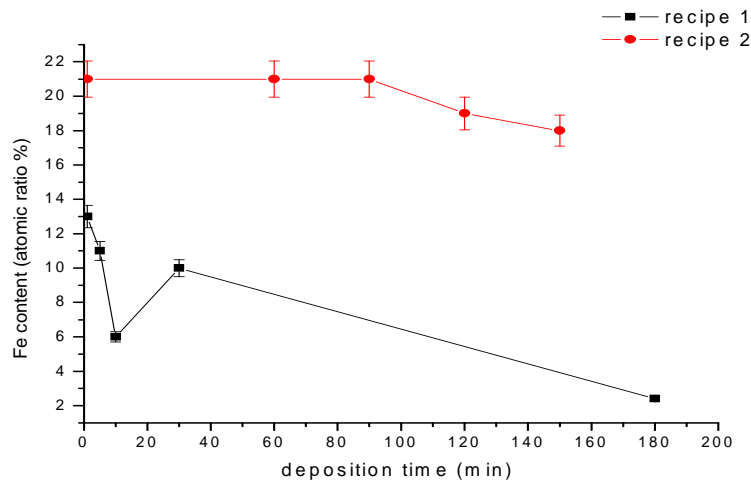
Figure 4.4, Fe content of deposited Permalloy films vs. deposition time. Improved recipe 2 shows much better composition stability compared with the starting recipe. Recipe 2 is available in Table 2.1.

The reasons for using Cu as a conductive layer for electrodeposition are the following: first, CuO itself can react with HMDS, causing a photoresist such as AZP 4620 to bond to it well; and second, Cu can be easily etched away by a saturated ammonia solution without damgaging any plated Permalloy parts. The thin layer of the HMDS will not insulate the Cu surface, so this Cu layer can act as the working electrode for plating Permalloy on Cu. The chemical bath I used was the same as listed in Chapter 2, table 2.1. The final plated permalloy film had a composition Ni:Fe atomic ratio of around 80:20 as measured by EDAX (in Appendix). It was a shiny silvery metal layer.

After these steps, I etched away the photoresist to obtain pole pieces. AZP 4620 was easily dissolved away by acetone or other polar organic solvents. Su-8, however, was much harder to wet etch without damaging the plated metal layer. I peeled the Su-8 template off by placing the specimen in a vacuum oven and raising the temperature to 200 ^{o}C - 250 ^{o}C at a rate of 50 ^{o}C/min and leaving it in the oven overnight. The Su-8 turned to a dark brown film full of cracks after this treatment and was easily blown off afterward. This procedure was also shown to be practical for Su's application [10].

The detailed procedures are listed below as "Procedure A" for the AZP 4620 based system and "Procedure B" for the Su-8050 system in the Appendix.

4.2.3 Pole Piece Force Measurements

The plated pole pieces were all tested for magnetic force exerting capability. The force measurements were performed under the assumption that there were no inertial effects in the system, so there was no acceleration when micro paramagnetic beads were pulled by plated pole pieces. In other words, $F_{pulling} = F_{dragging}$ at all times. This was satisfied because

the dimensionless number Reynolds Number, Re <<1 (which will be explained in Chapter 5) in this experiment. Therefore, based on the tracks of microbeads inside the sample cell, we can determine the magnetic pulling force by the Stokes function $F_{pulling} = F_{dragging} = 6\pi\eta av$, where η is the viscosity, a the bead radius, and v the bead velocity [11]. We found that for a specific pole piece, the force measurements were relatively repeatable (figure 4.5). The force exerted by a typical plated pole piece can range up to 50 pN on a 4.5 µm paramagnetic bead at a radial distance of 20 µm away from the pole tip end.

The near field about the tip ends is where the largest magnetic force can be applied. The magnetic field strength, however, is very sensitive to the geometry of the plated pole tips in this near field. Our pole fabrication is not so precise as to make the fabricated poles exactly the same each time, and so each magnetic pole piece must be calibrated before use in the 3DFM. Without fine-tuning the magnetic flux among the six poles in our 6 pole setup, it is not possible to generate a repeatable 3D complex magnetic field from the same current input set with different pole pieces. The plot shown in figure 4.6 is a force measurement of paramagnetic beads being pulled by two different plated pole pieces. We applied a magnetic force to one of the three poles to pull paramagnetic microbeads through Karo syrup. The other two poles were not activated during the experiment. The difference in the force exerted by each of the two pole pieces was at least partially caused by the pole piece fabrication (other reasons, including not being normalized to the same relative spatial positions, differences in the bead diameters, and imaging processing errors when the beads were too close to the tip ends, might also contribute to this difference).
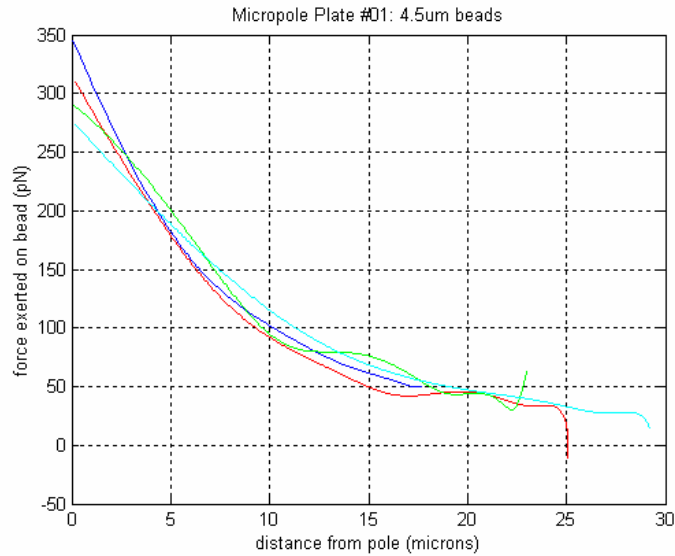
Figure 4.5, Force measurements in Karo syrup on 4.5 μm paramagnetic beads by the plated pole piece #1; the input current was 2 A.
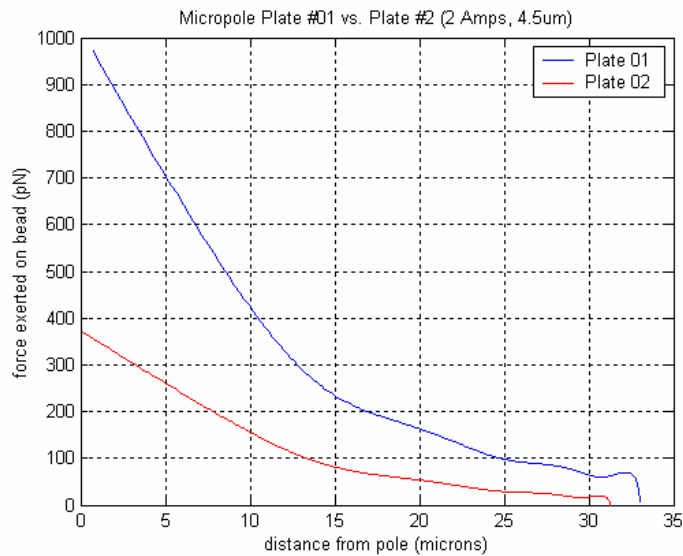
Figure 4.6, Force measurements in Karo syrup on 4.5 μm paramagnetic beads by 2 plated pole pieces starting at approximately the same radial distance from the tip end; the input current was 2 A.

4.3   Actuation and Actuation Mechanisms

4.3.1   Torque-Tilting Nanowires with a Soft PDMS Supporting Layer

There are two mechanisms which could be used to actuate standing magnetic nanowires:

1) the nanowire can be actuated as a bending cantilevered beam;

2) the nanowires can be anchored in a soft substrate and can be tilted without bending.

We demonstrated for the first time that a nanowire rooted in a soft polymer could be actuated by a moderate external actuating magnetic field. The experimental setup shown in figure 4.10 is a lateral microscope with a CCD video output focusing through a liquid reservoir with two parallel glass walls. The external actuating magnetic field was generated by moving a permanent magnetic bar (NdFeB Disc, 2" dia x 0.25" thick) in the same plane of the sample, toward and away from the sample, which corresponded to a field strength ranging from 291G to 6G normal to the nanowire dipole direction. The snapshots from recorded movies are also shown in figure 4.7.

The supporting film materials were not limited to PDMS. Photoresists like AZP 4620, UV curable silicon coating and other materials were also tested, but only the nanowire arrays with a PDMS substrate were actuable.

Due to the fact that the actuating magnetic field was normal to the nanowire easy axis, the dot product of the force, $F = m\nabla B$ is trivial. Therefore the external actuating magnetic field applied a torque to the nanowire instead of a force. The tip end displacement of the nanowire in figure 4.7 could either be caused by cantilever bending or tilting of a rigid body due to the softness of its supporting substrate. In the cantilever case (figure 4.8), the displacement of the rod projected in y direction, u_y, is then [12],

$$u_y(x) = \frac{\tau}{2EI_z} x^2 \tag{1}$$

Or rewriting it in terms of torque per volume τ_v, and $I_z = \int y^2 dA = \frac{2}{3} r^4$ (I_z is the area moment of inertia of the rod),

$$u_y(x) = \frac{3}{4} \frac{\tau_v L}{E r^2} x^2 \quad (2)$$

Here E is Young's modulus; L is nanowire length; r is nanowire radius; and x,y are the coordinates illustrated in figure 4.8.
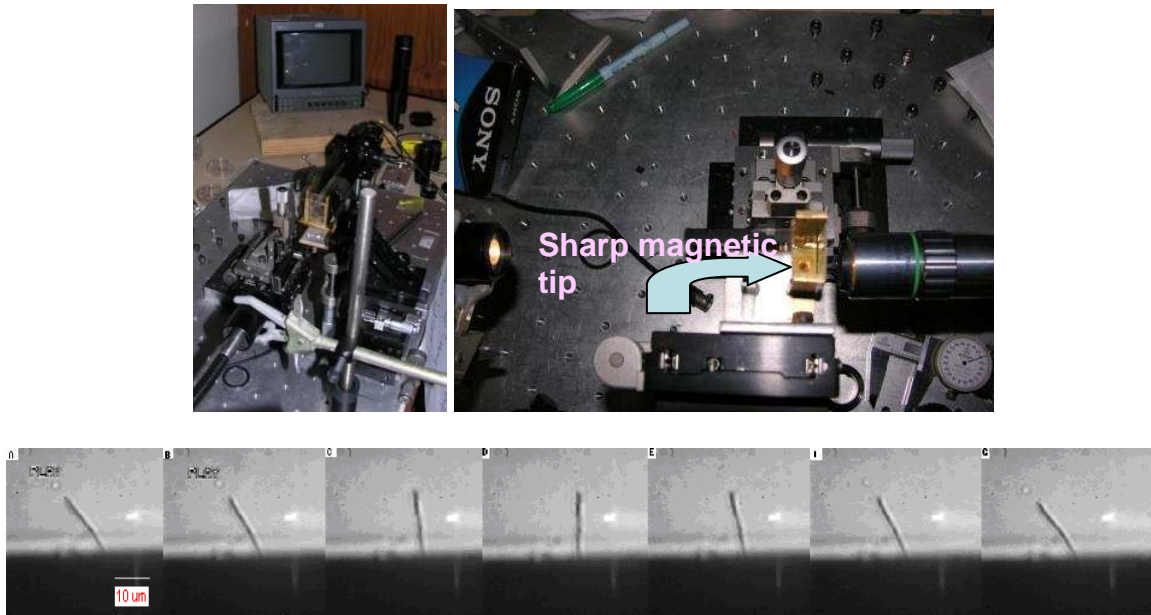
Figure 4.7, The lateral microscopy system to explore actuation mechanisms. Top, lateral microscopy video system with 20X objective used to record the movements of nanowires actuated by an external magnetic field. The central yellow part is the sample cell with two glass walls. The sharp tip at the bottom can generate a magnetic field with parabolic profile in the sample area. The actuation was realized by moving a permanent magnetic bar on a micro-stage. The CCD video output was recorded by a video tape; bottom, side view snapshots show a standing magnetic nanowire rooted in PDMS layer actuated by an external magnetic field (from image A 291 Gauss to image D 6 Gauss and then back to G 291 Gauss). The length of this nanowire is 22 um.

In the Stoner and Wolfarth model for the total energy of a magnetic ellipsoid of revolution, the energy is the sum of magnetization and shape anisotropy energies [13]:

$$E_{rod} = -BM_s \cos\phi - \frac{\mu_0 M_s^2}{2}(N_b - N_a)\cos^2(\phi - \theta) \quad (3)$$

where ϕ is the angle between the field and the magnetization moment of the nanowire and θ is the angle between the field and the easy axis of the rod; Ms is the saturation magnetization; N_b and N_a are demagnetizing factors along the width and longitudinal directions respectively. For a high aspect ratio nanowire, N_b-N_a = 0.5 [14]. Taking the derivative with respect to ϕ to be zero,

$$0 = B\sin\phi + \frac{\mu_0 M_s}{2}(N_b - N_a)\sin[2(\phi - \theta)] \quad (4)$$

and solving for ϕ at small $\phi - \theta$ (at week field, $\phi \sim \theta$[15]), and small θ,

$$\phi \cong \theta * \left[1 + \frac{B}{\mu_0 M_s (N_b - N_a)}\right]^{-1} = \theta * (1 + \frac{2B}{\mu_0 M_s})^{-1} \quad (5)$$

For B<0.3T, which was satisfied in my experiments, we noticed that this approximate solution holds well even when θ approaches $\pi/2$. The direction of the magnetic moment of a Permalloy nanowire is basically the same as its longitude axis direction when the field strength is small and the nanowire itself is very slender.

$$\tau = M_s VB\sin\phi \quad (6)$$

So we found

$$u_y(x) = \frac{3}{4}\frac{M_s BLx^2}{Er^2}\sin\left[\theta * (1 + \frac{2B}{\mu_0 M_s})^{-1}\right] \quad (7)$$

from equation (2) for the projected nanowire displacement in the X direction. Here V is the nanowire volume. Using $M_s = 8.33 \times 10^5$ A/m for a pre-saturated Permalloy magnetic nanowire shown in figure 4.7 (200nm wide, 22μm long), the displacement of the rod tip is 30 nm under a field of 0.03T, and θ approaches $\pi/2$. This is negligible compared to the 11.8 μm

displacement measured in my experiments. I therefore concluded that the displacement in figure 4.7 must be due to the rigid rotation of the nanowire in the soft PDMS substrate.
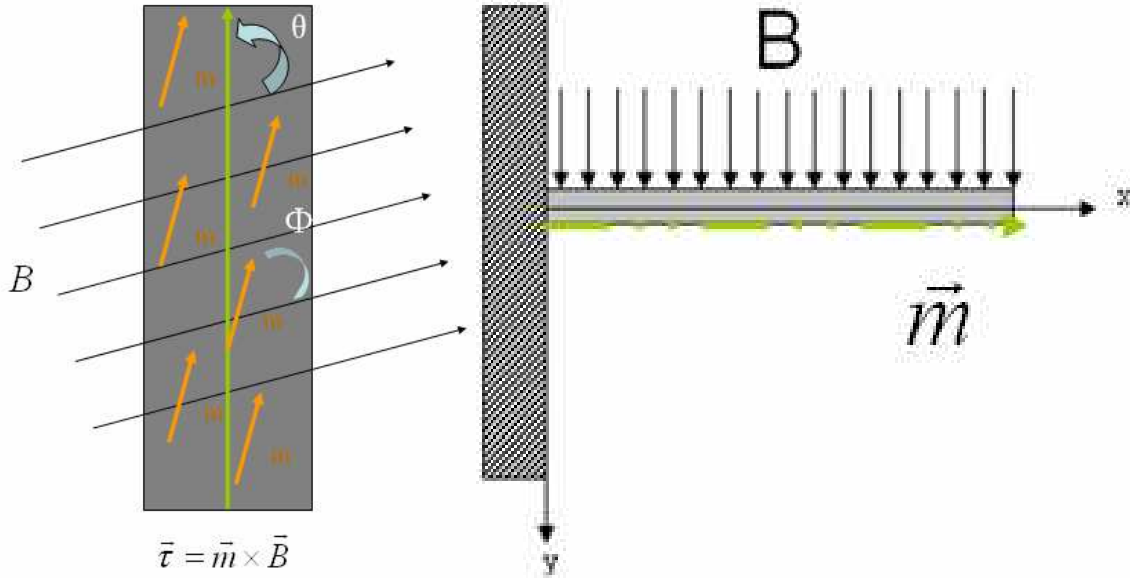
Figure 4.8, Schematic of field bending of a high aspect ratio magnetic cantilever, where ϕ is the angle between the field and the magnetization moment of the nanowire, θ is the angle between the field and the easy axis of the rod, m is magnetic dipole, and B is the magnetic field.

4.3.2   Actuating Standing Nanowire Arrays in 3DFM

In our lab, we have had a long-time interest in cilium movement in living creatures. To imitate mobile primary cilia such as the nodal cilia inside vertebrate embryos, we generated a complex external 3D time variant actuating magnetic field with a computer controlled "six-pole" magnetic force sub-system in our custom made 3DFM. One set of the base functions for the oscillating current inputs is sampled in figure 4.9 (note that, for each pair of pole pieces, a fine-tuning based this base function is necessary). This specific current input was designed to make a nanowire precess with a cone-shaped orbit. Magnetic poles

54

were glued to only the upper coils of coils pairs 1, 3, and 5, and to only the lower coils of coil pairs 2, 4, and 6. The glue used was Elmer's Glue-All. This magnetic field arrangement worked so well that in most cases a supporting polymer layer to hold the roots of the nanowires was not necessary to prevent the nanowires from sliding on the bottom cover slide during actuation. By using either a thin layer of Si grease or plasma treating the bottom cover slide surface, the friction between the nanowire roots and the bottom cover slide due to the downward force was strong enough to hold the nanowires in place.

Following procedures similar to those mentioned in Chapter 3, I fabricated standing magnetic nanowire arrays inside a flow chamber. The two ends of the flow chamber were connected to an external reservoir. Driven by PC controlled current inputs through an interface program, "Blender," written by Ben Wilde, standing magnetic nanowire arrays beat as sub-micron mechanical actuators inside this flow cell. Figure 4.10 contains the snapshots of an array of nanowires beating inside a flow chamber.
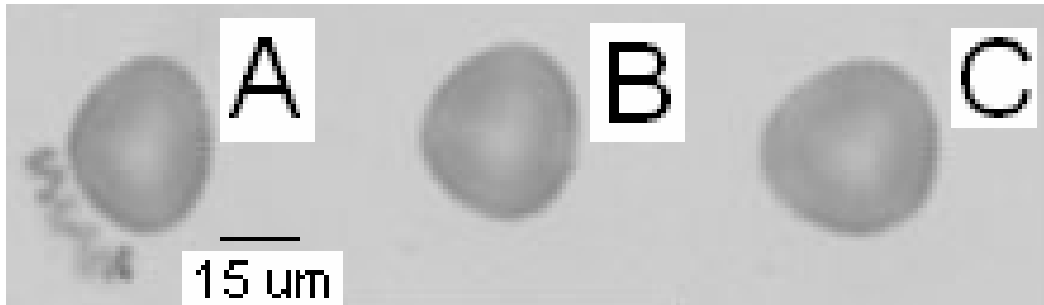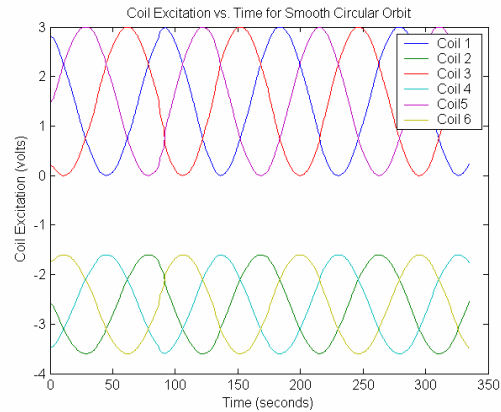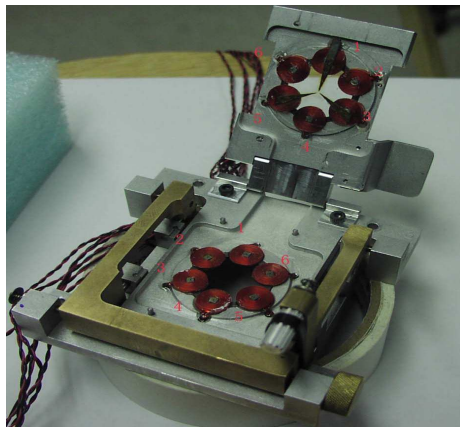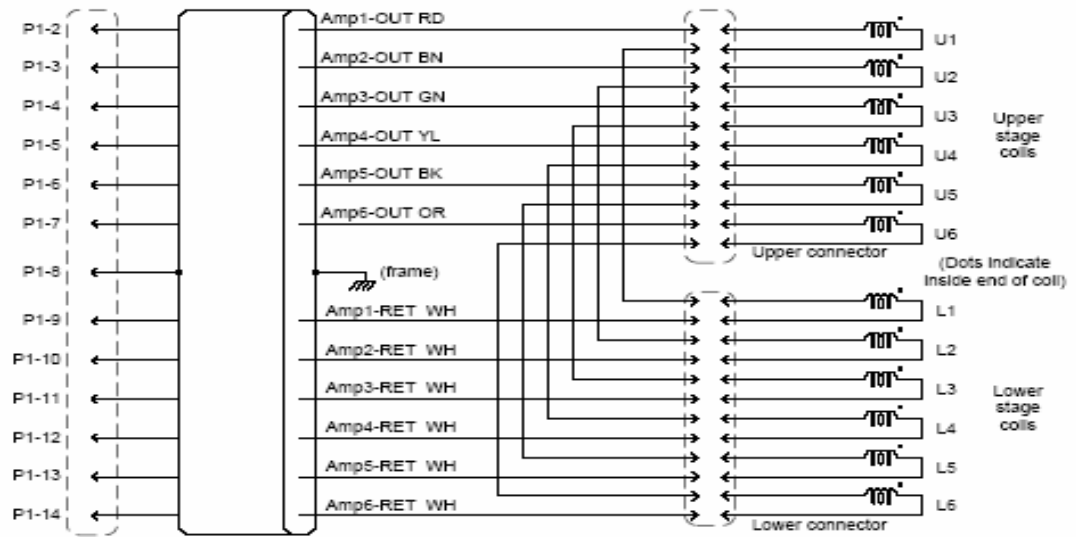
Figure 4.9, The 6 pole force subsystem used to generate a precessing movement. Top, coil wiring scheme (courtesy of Leandra Vicci); middle left, coil pairs coding in a real 3DFM 6 pole stage. Thin film magnetic pole tips were glued to the top 1,3,5 and the bottom 2,4,6 coils forming a 6 pole design; middle right, a current input set for 6 pole design in 0.011 Hz; bottom, superimposed images of a precessing nanowire without a supporting PDMS layer showed improved precessing orbits from A to C with a 1 Hz precession rate.

Figure 4.10, An array of magnetic nanowires rooted inside a supporting PDMS layer, beating with a triangular orbit inside a flow channel. Snapshots were taken by a built-in CCD camera in 3DFM *Betty* 1. The time sequence was pre-set so that a triangular orbit beating with 2/3 Hz could be performed. Each short black rod feature is a tilted nanowire projected in 2D. Arrows shown here are the schematic actuating magnetic field directions which are projected to the image plane.

Mixing is of fundamental importance for the successful development and application of lab-on-a-chip devices[16]. However, micrometer-scale microfluidic devices typically operate in low Reynolds number creeping flow regimes (Re <1). In creeping flow, diffusive mixing is a rather slow process and can require a substantial amount of time and space to achieve complete mixing [17]. Our devices can work as active micro-mixers like magnetic micro-stirrers or as prototypical man-made rigid cilia.

4.4   Conclusion

Standing nanowire devices have been actuated by our home made 3DFM as a demonstration of their use as mechanical actuators inside micro-fluidic systems. By fabricating magnetic dipoles with different properties, it is possible to adapt this idea not only

for the fabrication of mixers but also for the fabrication of a large number of sensors/actuators or optoelectronic devices.

Appendix,

Procedure A: AZP 4620 as photoresist

1. Mask designing and printing

2. Thermal deposition
- cleaning the substrate: UV plasma clean 1 min under the "high" power; Acetone, DI water, Methanol rinse
- thermal depositions: first, a 10 A Cr adhesive layer; then a 40-50 nm Cu conductive layer with a deposition speed 1-2 A/S.

3. Photoresist spin coating

Sec	RPM	Funct.	Comment
10	500		pre-treated with HMDS
30	3000	AZP4620	400 rpm/s ramp
10		Dry	
35	2000	Spin-out	

4. Pre-baking
30 sec at 60 ^{o}C then 90 sec at 125 ^{o}C on hot plate

5. Second layer of AZP 4620

Sec	RPM	Funct.	Comment
30	3000	AZP4620	
10		Dry	
35	2000	Spin-out	

Repeat step 4

6. Photolithography for AZP4620 resist with 25-30 µm thickness
- Exposing: with a power meter reading 10mJ/s, total exposure time is 7 min, 10' + 60' cooling time
- Developing: concentrated AZ400K with gentle stirring

7. Electroplating
- Recipe
  - NiSO4   200g
  - FeSO4   9g
  - NiCl2   5g
  - Boric Acid   25g
  - Saccharin Sodium   3g
  - H2O   1000g
- Using HCl to adjust the pH to 4
- Magnetic stirrer 200 rpm

- Using Ni as counter electrode
- pulse 1 KHz, square wave deposition with Peak-to-Peak potential = 4 V and $t_{on} : t_{off} = 1:1$ in each period

8. Dissolving AZP 4620
- Acetone rinse
- DI water rinse

9. Dissolving Cu
- Saturated Ammonia rinse, 10 min
- DI water rinse

Pole characterization
- File thickness was around 20-25 um (profilometry measurements in MCNC-RTI)
- Saturation field strength 0.84 T (SQUID Magnetometer), at 300K
- Coercive force was around 10 G
- Composition of the deposited film was Ni:Fe = 80:20 (EDAX in dental school of UNC-CH)
- Shape
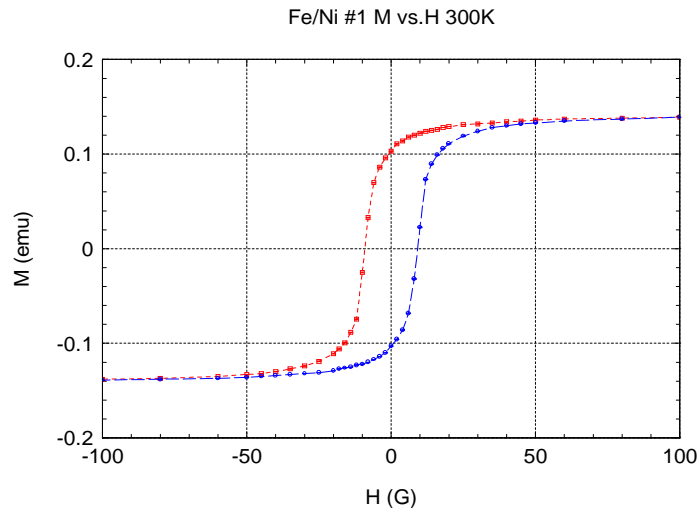
Figure 4.11, Magnetic and chemical properties of plated Ni:Fe alloy thin film. Top, SQUID measurement of a deposited Permalloy thin film pole piece; bottom, plated metal composition by EDAX measurements
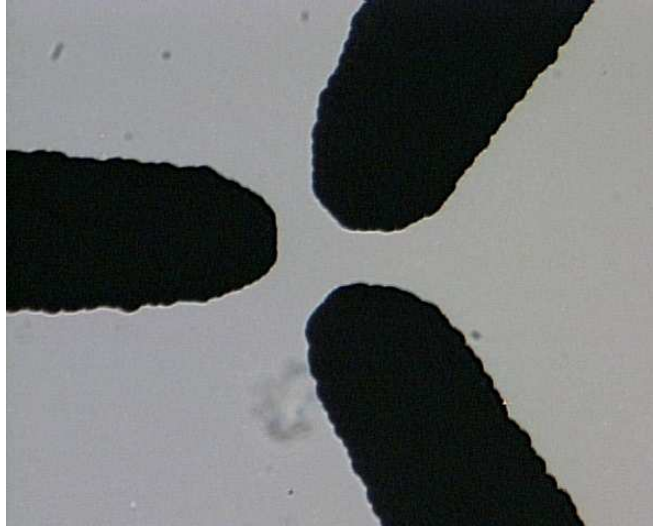
Figure 4.12, Optical image of the tip ends of one finished thin film pole piece

Procedure B: Su-8 2050 as photoresist

1. Mask designing and Printing
    The same as **Procedure A**

2. Thermal deposition
    The same as **Procedure A**

3. Photoresist spin coating

Sec	RPM	Funct.	Comment
60	2000	Su-2050	

4. Pre-baking
- 1 min 60 ^{o}C on hot plate
- 7 min 90 ^{o}C on hot plate untill the surface of the polymer coating is not sticky

6. Photolithography for Su-2050 resist with 40-50 µm thickness
- Using our equipment (10mJ/s), total exposure time is 20 Sec , 10' + 60' cooling time

7. Post Exposure Baking
- 1 min 60 ^{o}C hot plate
- 10 min 90 ^{o}C pre-set oven then cooling slowly

8. Developing
- MicroChem Su-8 Developer untill IPA rinsing is not cloudy and two point conductive measurements showing bare Cu appear

- IPA rinsing

9. Electroplating
the same as **Procedure A**

8. Su-8 removal
- Vacuum Oven 250-300 $^{\circ}$C over night
- CO_2 blow

9. Dissolving Cu
The same as **Procedure A**
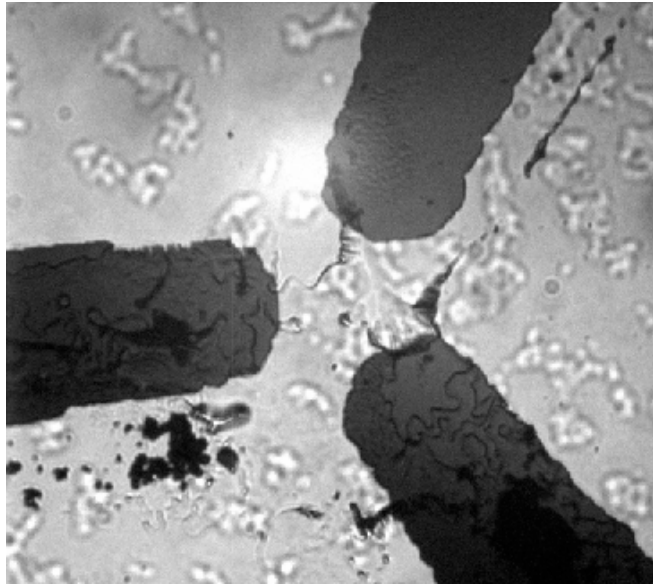
Figure 4.13, Optical image of the tip ends of one completed thin film pole piece.

4.5   Reference

1.   Vuppu, A.K., et al., *Phase sensitive enhancement for biochemical detection using rotating paramagnetic particle chains.* Journal of Applied Physics, 2004. **96**(11): p. 6831-6838.

2.   Hultgren, A., et al., *Cell manipulation using magnetic nanowires.* Journal of Applied Physics, 2003. **93**(10): p. 7554-7556.

3.   Fisher, J.K., et al., *Thin-foil magnetic force system for high-numerical-aperture microscopy.* Review of Scientific Instruments, 2006. **77**(2): p. -.

4.   *Methods and Systems for Controlling Motion and Tracking of a Mechannically Unattached Probe*

5.   Vicci, L., *Analytical bead force model for the 3DFM TR03-029.*

6.   Nayfeh, M.H. and M.K. Brussel, *Electricity and magnetism*. 1985, New York: Wiley. xiv, 619.

7.   http://microlab.eecs.berkeley.edu/labmanual/chap4/4.6.html.

8.   MCNC, *unpublished processing manual.*

9.   Osaka, T., T. Momma, and T. Yokoshima, *Research and development of high performance soft magnetic thin films.* Electrochemistry, 1999. **67**(9): p. 894-899.

10.   Oh, S.J., et al., *Liquid-phase fabrication of patterned carbon nanotube field emission cathodes.* Applied Physics Letters, 2004. **84**(19): p. 3738-3740.

11.   White, F.M., *Fluid Mechanics*. 5 ed. 2004: Mc-Graw-Hill.

12.   Atanackovic, T.M. and A. Guran, *Theory of elasticity for scientists and engineers*. 2000, Boston: Birkhèauser. xii, 374.

13.   Stoner, E.C. and E.P. Wohlfarth, *A Mechanism of Magnetic Hysteresis in Heterogeneous Alloys (Reprinted from Philosophical Transaction Royal Society-*

London, Vol 240, Pg 599-642, 1948). Ieee Transactions on Magnetics, 1991. **27**(4): p. 3475-3518.

14.   Osborn, J.A., *Demagnetizing Factors of the General Ellipsoid.* Physical Review 1945 **11-12**: p. 351-358.

15.   Evans, B., *78 Permalloy Rod in B-Field at Saturation*.

16.   Lu, L.H., K.S. Ryu, and C. Liu, *A magnetic microstirrer and array for microfluidic mixing.* Journal of Microelectromechanical Systems, 2002. **11**(5): p. 462-469.

17.   Vuppu, A.K., et al., *Modeling microflow and stirring around a microrotor in creeping flow using a quasi-steady-state analysis.* Lab on a Chip, 2004. **4**(3): p. 201-208.

CHAPTER 5 – Hydrodynamics about a Precessing Nanowire in Viscous Flow

5.1   Introduction

Many biological mixing and transportation processes are generated by the motion of a slender body in viscous media. However, both the experimental and theoretical works related to this motion are overlooked. We have known that all of the cellular scale feeding, swimming, mixing, and transporting functions happen in an over-damped viscous environment, and on this scale, thermal noise is comparable to or even larger than the active motions themselves [1]. A better understanding of fluidics on this scale requires that challenging experiments and modeling be done in order to separate the inherent flow nature from Brownian motion. My research in this chapter demonstrates, for the first time, fluidic experiments on the sub-micron scale which reveal the nature of the flow about a precessing slender body in a low Re environment.

Cilia and flagella appear very early in evolutionary processes, providing unicellular organisms with motility in water. They also take part in many functions such as the left–right asymmetric embryo development, cerebrospinal fluid flow, and mucociliary clearance in human body [2]. Researchers have not developed necessary hydrodynamic solutions related to cilia beating without external parameters until this thesis work.

Cilia and flagella are highly ordered structures. In general, there are four subcategories of cilia structures, which are motile 9+2 cilia, motile 9+0 cilia, sensory 9+2 cilia, and sensory 9+0 cilia [2]. Figure 5.1 illustrates the internal structure of a cilium with 9+2 structure.
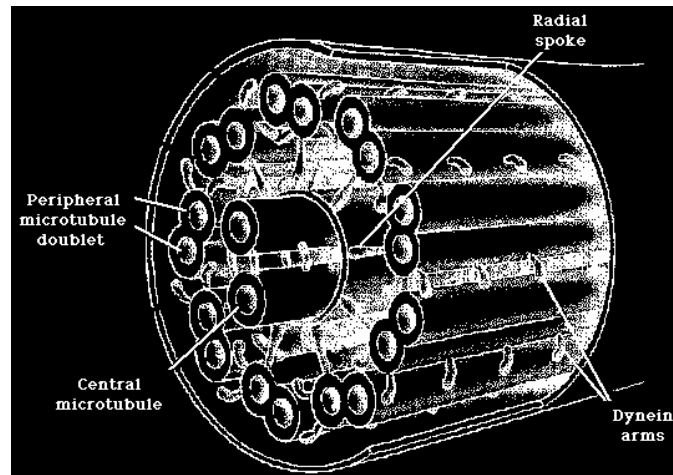
Figure 5.1, Schematic of microtubules within the shaft of a cilium. The movement of cilia and flagella is due to interactions between the peripheral microtubule doublets. These interactions require energy in the form of ATP (copy from[3]).

One specific example of interest is the presence of motile primary cilia in the node of mouse embryos. These nodal cilia have a 9+0 architecture. One landmark experiment done by Shigenori Nonaka proved that artificial rightward nodal flow can reverse the intrinsic leftward nodal flow and subsequently lead to the reversal of the right and left symmetry in wild-type mouse embryos. In addition, this is the first time a definite example of motile primary cilia was proved to exist [4, 5]. Essner proposed that this nodal flow is the basic reason for left–right symmetry breaking among vertebrates since the nodal cilia were found in other vertebrate embryos [6]. However, the mechanism of this leftward flow is still under discussion. Citing Shigenori Nonaks's, "of the questions that remain unanswered, one of the

most important concerns the mechanism by which the vectorial flow is generated by the rotational movement of the cilia." [7] For example, Nobutaka Hirokawa's group argued that the shape of the node explained the reason that we only saw leftward flow in nodal space (figure 5.2 A) [8, 9]. About the same time, a research group in Spain discussed that the leftward flow that has been experimentally observed may be produced by an array of nodal cilia tilted toward the posterior (figure 5.2 B) [10]. Other researchers claimed that primary cilia beat with the same pattern as 9+2 motile cilia, which beat in a nonplanar path (figure 5.3 C) [11]. In regard to all these controversies related to the right-left determination mechanisms in embryo developments, the key issue is the absence of an exact study of the flow pattern about a precessing slender body. Without an understanding of the flow pattern about a single precessing slender body, it is impossible to build up a model to explain the leftward nodal flow in the vertebrate embryos.

In my research, I focused on the hydrodynamics about a precessing nanowire. The actuable devices based on the method introduced in Chapter 3 offered us a solid experimental platform to reveal the flow pattern about a precessing nanowire. It is the first time a complex flow pattern was characterized with a comparable Brownian component.
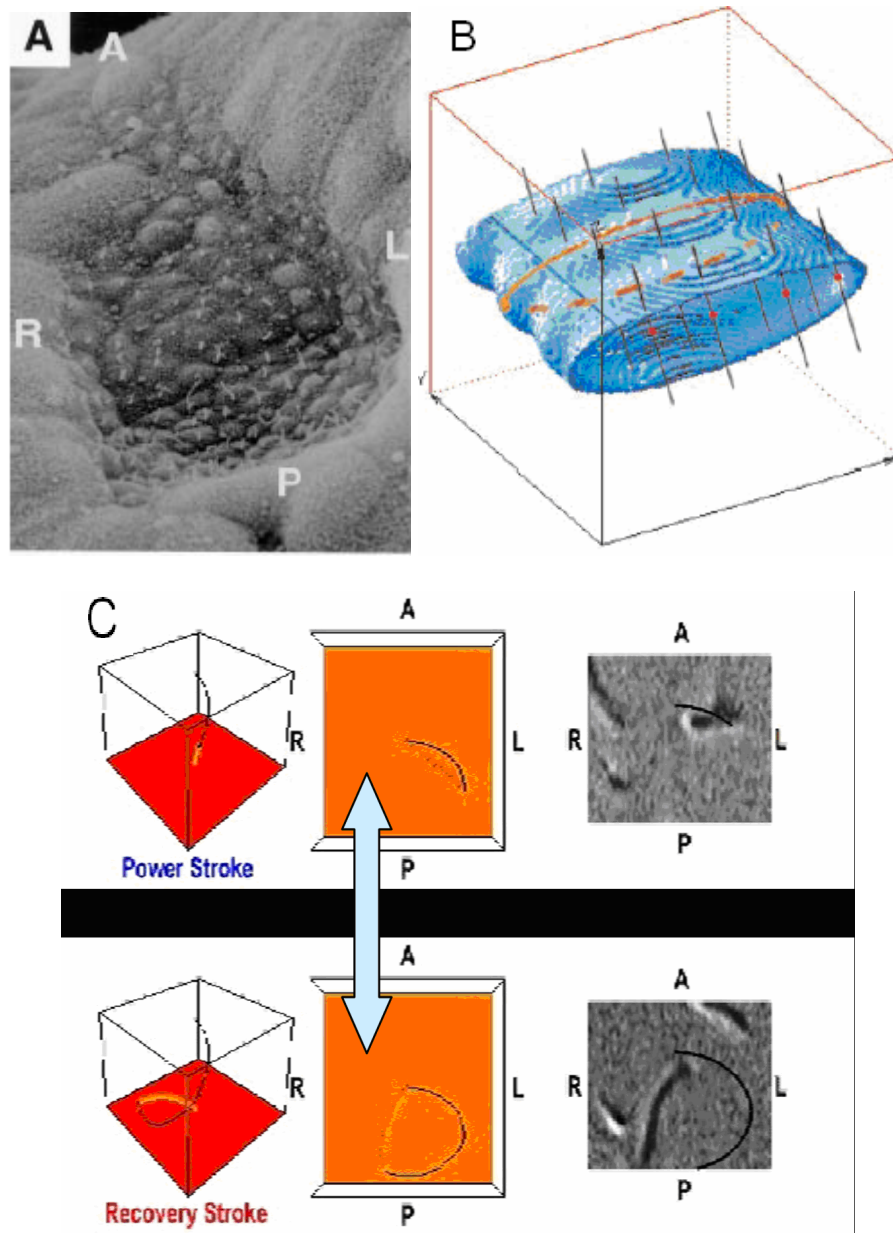
Figure 5.2, Hypothesis explaining the apparent leftward flow observed in wild type mouse embryos; A, triangle shaped node confines the nodal flow patterns; B, primary cilia tilted toward the posterior direction generates leftward flow in a closed space; C, two-phase asymmetric beating induces a net leftward advection. (A, anterior; P, posterior; L, left; R, right) (copy from [8-11])

5.2   Fluid Dynamics at the Sub-micron Scale

5.2.1   Continuum Hydrodynamic Model

A basic assumption of fluid dynamics is the Continuum Condition. Liquids are aggregations of molecules, which by the definition of a liquid which are not fixed on a lattice but move relative to each other. Properties like density and mass can only be treated as constants when the total number of the molecules inside a unit volume remains unchanged. A generally accepted value for this number density is 10^{-9} mm^3 for both liquid and air at atmospheric pressure [12]. Below this criterion, it is not appropriate to treat these ensemble averages as constants. To use the Navier-Stokes equation, we first assumed that this elimination of discreteness holds in sub-micron scale fluid dynamics. The comparison between the experimental and theoretical results will verify the correctness of this continuum assumption.

5.2.2   Navier-Stokes Equations and Hydrodynamic Similarity in Viscous Flows

For a Newtonian fluid, the viscous stresses are proportional to the strain rates and the coefficient of viscosity. We can write down the 3D incompressible flow differential momentum equation as,

$$\rho g_x - \frac{\partial p}{\partial x} + \mu(\frac{\partial^2 u}{\partial x^2} + \frac{\partial^2 u}{\partial y^2} + \frac{\partial^2 u}{\partial z^2}) = \rho \frac{du}{dt}$$

$$\rho g_y - \frac{\partial p}{\partial y} + \mu(\frac{\partial^2 v}{\partial x^2} + \frac{\partial^2 v}{\partial y^2} + \frac{\partial^2 v}{\partial z^2}) = \rho \frac{dv}{dt}$$

$$\rho g_z - \frac{\partial p}{\partial z} + \mu(\frac{\partial^2 w}{\partial x^2} + \frac{\partial^2 w}{\partial y^2} + \frac{\partial^2 w}{\partial z^2}) = \rho \frac{dw}{dt} \quad (1).$$

These are the incompressible flow Navier-Stokes equations named after C.L.M.H. Navier and Sir George G. Stokes [13]. This may also be written as

$$\rho \frac{dV}{dt} = \rho g - \nabla p + \mu \nabla^2 V \quad (2).$$

This can be further simplified as a set of dimensionless equations for simple formatting and easy understanding. Choosing two reference constants: Reference Velocity ≡ U, Reference Length ≡ L, it is possible to rewrite the variables as

$$V^* = V/U \qquad \nabla^* = L\nabla \qquad x^* = x/L \qquad y^* = y/L \qquad z^* = z/L$$

$$t^* = tU/L \qquad p^* = (p + \rho g z)/(\rho U^2)$$

(the choice of p^* is not hard to understand if we use the integral relation in the steady incompressible flow, $\dfrac{p_2 - p_1}{\rho} + \dfrac{1}{2}(v_2^2 - v_1^2) + g(z_2 - z_1) = 0$). Thus, the new momentum equation is

$$\frac{dV^*}{dt^*} = -\nabla^* p^* + \frac{\mu}{\rho U L}\nabla^{*2}(V^*)$$
(3).

Named after Osborne Reynolds, the dimensionless number Reynolds Number (Re) is defined as $\text{Re} = \dfrac{\rho \upsilon l}{\mu}$, where ρ is the liquid density, υ is the fluid velocity, l is the characteristic length and μ is the dynamic fluid viscosity [13]. This dimensionless parameter Re can be interpreted as the ratio of inertial force to viscous force,

$$\text{Re} \equiv \frac{InertialForce}{ViscousForce} \propto \frac{\rho u \dfrac{\partial u}{\partial x}}{\mu \dfrac{\partial^2 u}{\partial x^2}} \propto \frac{\rho U^2/l}{\mu U/l^2} = \frac{Ul}{\nu} \text{ (4).}$$

For a typical primary cilium in a wild type mouse node, 300 nm diameter, 5 um long and beating at 5 Hz, using the η of water for the nodal medium, Re = $1.6\text{X}10^{-3} \ll 1$. This is a flow called low Re flow or viscous flow.

The Reynolds Number is the most important dimensionless number for any discussion of hydrodynamic similarity. To be able to compare two flows, it is necessary to

keep their Re values the same. For example, by keeping Re constant we can study sub-micron fluidics in larger table-top scale experiments as long as we are not concerned with the influence of Brownian motion. Note that dynamic similarity even in Newtonian environments may require matching other dimensionless numbers as well. This dynamic similarity is the fundamental assumption in all my discussions in this chapter.

Many phenomena in viscous flow differ from our everyday experiences. I have demonstrated that inertia plays no role whatsoever for Reynolds number as low as 10^{-3}. What happens to an object at one moment is entirely determined by the forces that are exerted on that object at that moment, with no memory of the past. This low Re environment is typical in the biological world of cells. Swimming at low Reynolds number is a general way in which many microbes move, feed, and communicate with their environments [1]. In all the cilia movements mentioned above, the viscous drag force dominates.

In Newtonian environments, as long as Brownian motion is not taken into account, everything works 'reciprocally' or 'conservatively' [14]. An imaginary experiment can tell this story well enough: if we draw an ink cycle in a cone and plate tank full of very viscous syrup, and make sure to rotate the cone slowly clockwise and then counter clockwise the same number of revolutions (the angular speed should satisfy Re << 1), what we see is that this ink cycle will return to its original shape as if nothing had happed! But in real mucus or nodal fluid, a non-Newtonian model is appropriate.

There are other dimensionless numbers needed to capture the fluidic dynamic nature of a non-Newtonian liquid. Groisman and his group generated turbulent flows in a high molecular weight polymer solution with Re as low as 0.06 [15, 16]. This is very interesting since it is somewhat difficult to understand why turbulence can happen in this low Re

71

environment (as discussed above, the inertia is trivial when Re << 1). To obtain the correct description of the dynamic nature, a dimensionless number called the Deborah number, De is needed. This will be further discussed in Chapter 6.

5.2.3 No-slip boundary condition

Viscous flow can be treated as "no-slip", "slip", or "partially slip" at the boundary depending on the nature of the physics. Even though at the molecular level mechanisms related to the whole boundary conditions are still a mystery, researchers often assume the no-slip condition holds in sub-micron biological systems due to the low Re in these environments.

Mathematically, the no-slip condition can be written as $[\ \mathbf{v}_\| \ ] = \mathbf{0}$, where $\mathbf{v}_\|$ is the component of $\mathbf{v}$ parallel to the interface at the boundary. Here I assume the no-slip boundary condition holds well in all my microbead experiments in Newtonian environments, but still leave the question open until solid experimental evidence is available.

5.3   Model Cilium Hydrodynamic Experiments

5.3.1   Model Cilium Fabrication and Actuation

One of the purposes of my research is to build a robust system, which can be an experimental platform for the study of flows related to a beating cilium. Figure 5.3 demonstrates a model primary cilia beat pattern inside a mouse node [11]. The similarity between this and my precessing magnetic nanowire is clear. The differences between the two are listed below:

1. My magnetic nanowires are very rigid. Neither the magnetic torque nor the hydrostatic drag force will be able to bend them;

2. I purposely allow the magnetic nanowire precess about a vertical axis for simplicity. Research suggests, however, that motile primary cilia in nodes may precess along a tilted rotation axis [10].

My sample cell was composed of two cover slides with two to three layers of double face tape as a spacer. The bottom number 0 cover slide was cleaned by a 1 min 100 W plasma treatment and a subsequent rinsing procedure. Two techniques were used to modify the bottom cover slide so that the nanowire could precess on top of it. The first was spreading a thin layer of vacuum grease on the glass surface with a stainless blade. Measurements from SEM images showed that this left a sub-micron layer of grease (in most cases it was not a continual film). This was a simple way to get a magnetic nanowire to precess without sliding while being actuated under 3-D oscillating driving fields. The net force down toward the bottom would hold nanowires in their positions. This technique, however, leaves an uneven bottom boundary. The other method was to plant nanowires inside a soft supporting layer. Soft rubbery PDMS was first spin-coated its pre-polymer form; then later cured. This thin supporting layer would hold the roots of the nanowires in place (figure 5.3).

Figure 5.4 shows the top view of superimposed projections of a nanowire in a precessing orbit without a supporting layer. Clearly, we succeeded in producing a conical orbit by finely adjusting our 3DFM driving fields. The uprightness of the beating cone space has been verified in real time by ensuring that the root of this nanowire is precisely at the center of the projected cycle.
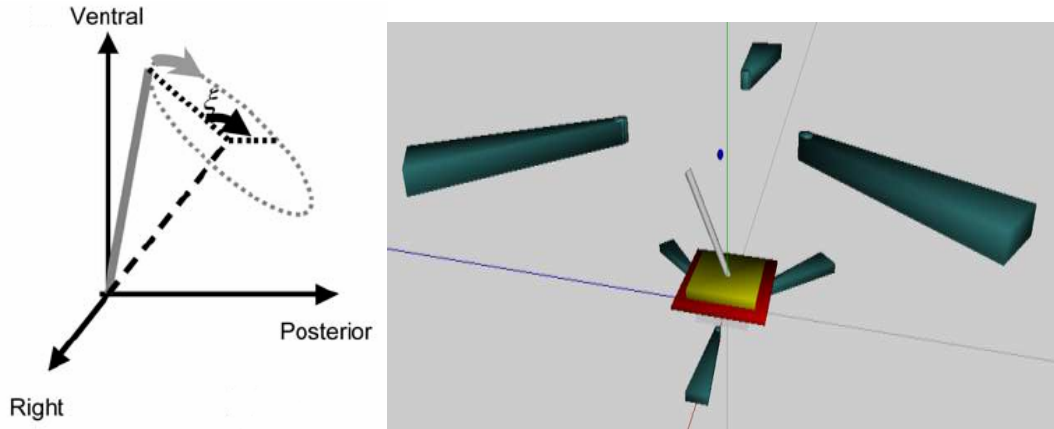
Figure 5.3, Schematic model for nodal cilium beating inside a wild mouse node. Left, a tilted rigid cilium model (copy from [11]); Right, the ideal placement of a upright precessing rod with a tracer nearby. The green structures are thin film magnetic poles; the red square is a 0# cover slide; and the yellow layer is the soft PDMS supporting film. The magnetic nanowire will orbit on its root to generate an epicyclical flow which can be tracked by passive tracers.
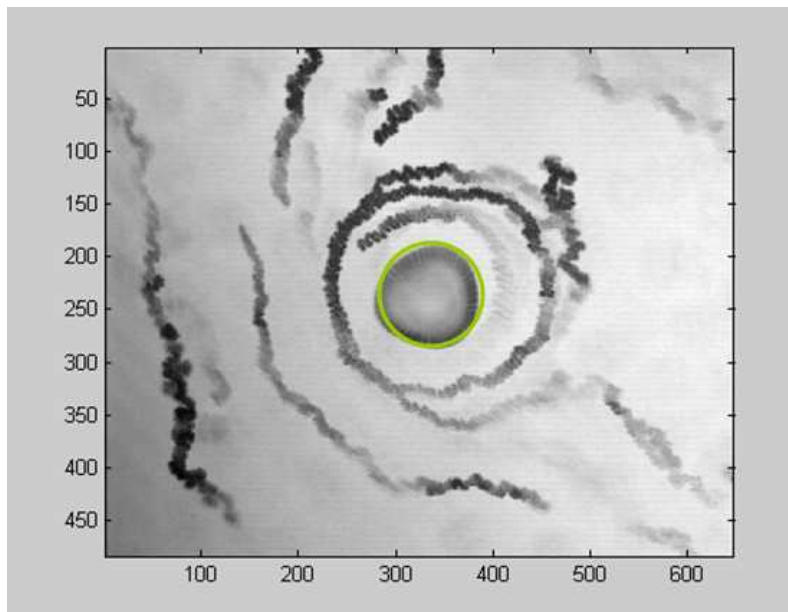
Figure 5.4, Top view of a precessing nanowire and the tracers near it. The image is a 2-D minimum intensity projection from a brightfield movie. The projected track of the precessing nanowire is highlighted by a solid cycle; and the outer gyrating dark tracks are the tracks of passive tracers. X and Y axis are pixel values.

74

Two to three layers of double face tape separate the bottom and the top cover slide by at least 100 μm. After injecting the nanowire suspension inside the sample space, a number 1, 20mmX20mm square cover slide was placed on top of the spacer. To minimize macroscopic flow due to evaporation, I used nail polish to seal two ends of the sample. The resulting optically clear sandwich structure was placed inside the sample holder of 3DFM for further experimentation.

5.3.2   Passivity of Tracers

To study the nature of a flow, researchers have used a variety of tracers to reveal flow patterns. For example, by electrolysis, we can leave H_2 bubbles along the electrolyte streams. By recording bubble movements, flow patterns can be revealed. Similar techniques have been developed using ink, beads and smoke (common in air dynamics) as tracers. I chose Polystyrene Microbeads (Polysciences, Inc.) as micro-tracers for sub-micron fluid dynamics research because of their inert nature and availability.

To ensure that our designs are experimentally sound, I first checked whether the beads acted as passive tracers. Basically, passivity means that the tracers can exactly follow the flow patterns as if they were point sources within the flow. If thermal motion is neglected, this question can be answered by checking for differences in motion between particle trackers and the flow field without tracers inside.

One obvious concern is gravity, or what I refer to as the "settling problem" in my thesis. As discussed previously, this is a low Re regime (10^{-3}). Without inertia, the net movement induced by the density difference between the media (water) and the tracers (in this case PS beads, CAT#24062 from Polysciences, Inc. $\rho = 1.05$mg/cc, Diameter = 0.932

μm) can be expressed as the gravitational force, F_g, which is always equal to the drag force, F_D on the tracers,

$$F_g \equiv F_D \ (5).$$

$$M = \frac{4}{3}\pi R^3 \rho_{tracer}$$

$$F_g = Mg \frac{\rho_{tracer} - \rho_{media}}{\rho_{media}} \ (6)$$

$$F_D = 6\pi\eta RV$$

$$F_g \equiv F_D$$

Here M is the mass of the tracer; ρ is the relative density; η is the medium viscosity; V is the tracer velocity; and R is the tracer radius. Solving these functions for V gives

$$V = \frac{Mg \dfrac{\Delta\rho}{\rho}}{6\pi\eta R} = \frac{2}{9}\frac{R^2 g}{\upsilon} \times 0.05 = 0.0875 \times 10^{-6} \text{ m/sec } (7).$$

During my typical sampling time scale, 300 frames over 2.5s, the net displacement V • t = 0.22×10^{-6} m is less then the tracer diameter 10^{-6} m and is less than the root mean square of the Brownian motion displacement, which is around 1.45×10^{-6} m in 2.5 sec. It is therefore reasonable to treat these PS beads as passive tracers regarding the settling problem, given my experimental time scale.

Heat convection can be an unwanted source of fluid flow. When a dimensionless number, the Rayleigh number, Ra [1] exceeds a critical value, there will be convective flow. This critical value can depend on boundary conditions. In my case, the sample cell is always closed with the top liquid surface in contact with a fixed surface. According to the literature,

---

[1] $Ra \equiv \dfrac{\alpha g \Delta T d^3}{k\nu}$ where α is the thermal expansion coefficient; ν is the kinematic viscosity; and κ is the thermal diffusivity.

the onset value for convection in this situation is around $R_a \sim 1700$ [17]. My sample cell is approximately 150 μm in Z. The material parameters α, κ and ν are 4×10^{-4} k^{-1}, 1.5×10^{-7} $m^2 s^{-1}$ and 10^{-6} $m^2 s^{-1}$ respectively. The Ra$\sim 10^{-6}$ is therefore far less than 1700 in my set up. So even though the bottom coils in the 3DFM may create a small heat gradient in Z direction in my sample, it is very safe to assume that there is no convective flow in these sample cells.

However, thermal noise or Brownian motion will always be present. The well-established Stokes function gives $\sqrt{< R^2 >} = \sqrt{\dfrac{kT}{\pi \eta R} t}$. Taking the tracer diameter to be 10^{-6}m, the root mean square of the Brownian displacement is around 0.8 μm in water on a time scale of 200 ms, which is the nanowire precession period in most of my experiments ($\eta = 1$ cp, T = 300 k, R = 0.5 μm). This is already comparable with the epicycle size which will be addressed more clearly later this chapter. How this noise will affect the flow patterns near a beating cilium is also an interesting topic we are trying to resolve.

It is also important to address the effect of the size of the tracers on their passivity. The force on a particle in a flow is obtained by integrating the local pressure over the surface of the particle. If the flow velocity field is constant or linear, the tracer can be treated as a passive tracer since the surface integration of a constant or linear pressure around the sphere divided by the surface area will give the same constant or mass-center pressure value. But if the flow velocity field is not a linear differentiable function, the integration is geometry-dependent. Depending on the local concavity or convexity of the velocity field profile, the sub-micron tracer velocity may be lower or higher than the velocity at the tracer mass center in the same flow without tracers. Detailed calculations can be performed only if we have the full flow field. Here I first assume the size of the tracer is negligible.

5.3.3   In Situ Viscosity Measurement and Correction

Two kinds of cameras were used to record Brownian motion of sub-micron tracers for viscosity data. For brightfield, the camera was a high speed CCD Pulnix camera connected to a high speed blade hard disc, with the ability to take 120 frame per second (fps), full frame, and progressive scan. The fluorescent movies were captured by a frame transfer, cascade Roper camera. Under circular buffer, frame transfer and fast capture mode, it is possible to capture a stream of full frame movies near 30 fps under 1 X 1 binning and near 100 fps under 2X2 binning. By analyzing tracer tracks with a custom "Spot Tracker" tool, it is feasible to measure tracks to sub-pixel accuracy. Media viscosity is directly derived from the Stokes-Einstein relation, $\eta = \dfrac{kT}{6\pi DR}$ (D, the diffusion constant, is derived from $\langle R^2 \rangle = 4\,D\,t$ for 2 dimensional projections). Figure 5.5 is an experimental data set taken to show how we determine the viscosity in situ (in this sample, $\eta = 0.79$ cp).
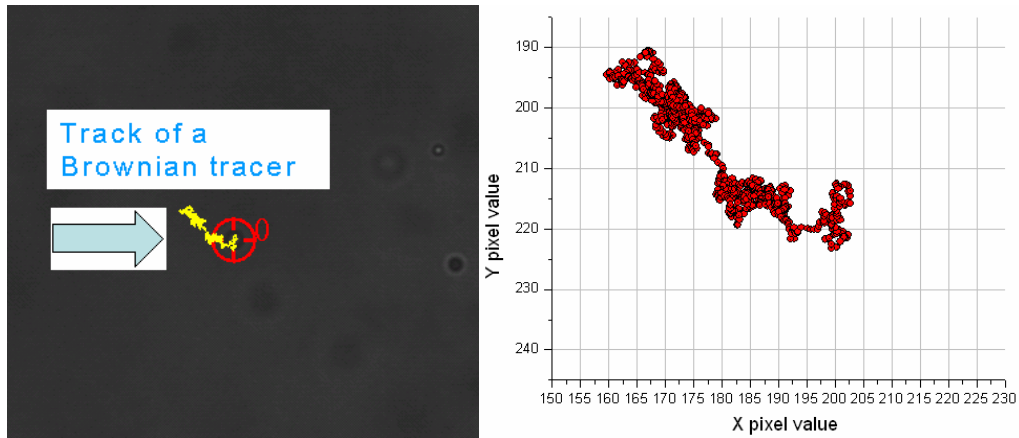
Figure 5.5, Schematic of how the viscosity is measured in situ. Left, tracks of a tracer by "Spot Tracker"; right, the output of the Brownian tracks.

There are two hydrodynamic coupling effects which must be taken into account for all of these Brownian motion measurements. The first is the wall effect. Researchers [18] have convincingly demonstrated that the track of the Brownian motion of a spherical particle near a wall is coupled hydrodynamically to the bounding surfaces. This effect may influence the particles' motion to a great extent and over a relatively long range. The correction introduced by Brenner [19] in 1965 shows

$$\frac{D_{(z)}}{D_{0(z=\infty)}} = 1 - \frac{9}{16}(\frac{r}{r+z}) + \frac{1}{8}(\frac{r}{r+z})^3 - \frac{45}{256}(\frac{r}{r+z})^4 - \frac{1}{16}(\frac{r}{r+z})^5 \quad (8).$$

Here r is the bead tracer radius, $D_{(z)}$ is diffusion constant at a distance Z away from a 2D infinite flat surface, and D_0 is the free space diffusion constant. If choosing a tracer with radius 1 μm, the plot of $D_{(z)}$ /D_0 to Z shows a more than 10% loss due to the hydrodynamic coupling by the wall when beads are 2 μm away from the bottom substrate (figure 5.6). To be safe, the Brownian motion tracks were all taken at least 10μm away from both the bottom and the top cover slides.
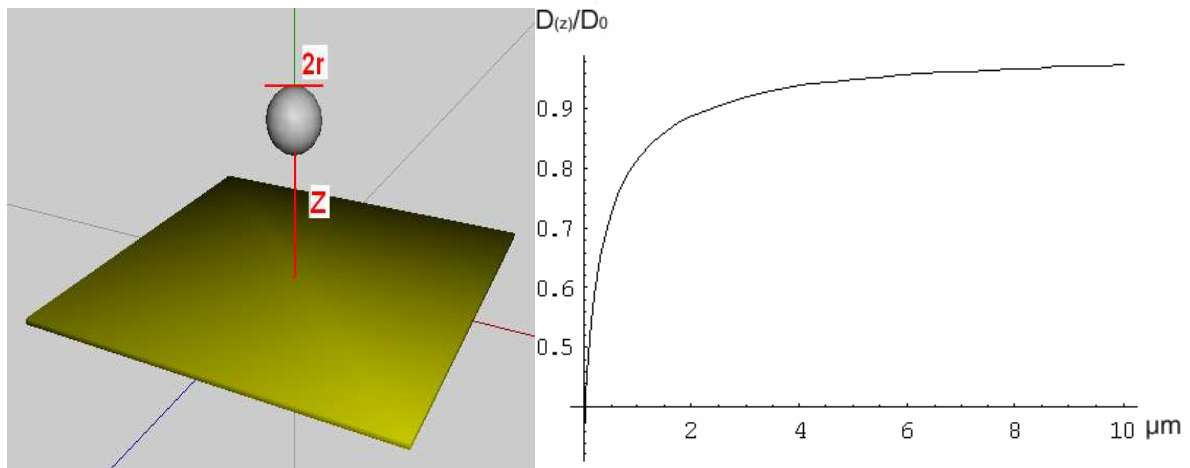
Figure 5.6, Schematic of the wall effect on a Brownian spherical particle. Left, a confined self-diffusing bead near wall; right, plot of $D_{(z)}$/D_0 vs. the Z distance between the bead and the nearby wall.

The second hydrodynamic correction term is the coupling between two spherical tracers close to each other [20]. In the most ideal case, both spheres have the same radius and freely respond to each other's flow field (including the freedom to rotate) without external torques. Batchelor [21] calculated the diffusion constants in two directions as,

$$D_{cm}^{\Uparrow} = \frac{D_0}{2}[1 + \frac{3}{2\rho} - \frac{1}{\rho^3} - ...]$$
$$D_{cm}^{\perp} = \frac{D_0}{2}[1 + \frac{3}{4\rho} + \frac{1}{2\rho^3} + ...]$$
(9)

The diffusion constants of the center of mass itself, $D_{cm}^{\Uparrow}$ is the diffusivity along the center-center line between the two spheres and $D_{cm}^{\perp}$ is the diffusivity in the plane perpendicular to this central line. Here ρ is a dimensionless number, $\rho \equiv$ (sphere-sphere distance) / sphere radius. I must set a minimum bead-to-bead distance to ensure the correctness of the passive tracer assumption in order to be able to treat the PS microbeads as individual passive tracers. In my dissertation, I generally let $\rho > 10$ (unless otherwise noted) based on my calculation (figure 5.7). In other words, the microbead number density is no higher than 1 per 100 μm^2 in 2D when using 500nm radius microbeads.

In general, the PS microbeads I used to characterize the flow patterns about a precessing magnetic nanowire proved to be almost entirely passive. Due to the robust design, this sample was a reliable platform for repeatable physical measurements.
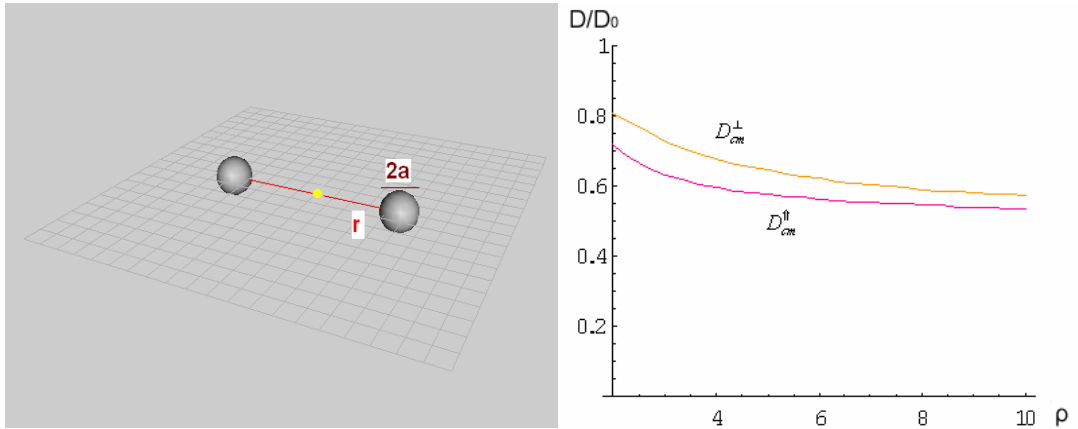
Figure 5.7, Schematic of hydrodynamic coupling between two Brownian spherical particles. Left, the hydrodynamically coupled dipole diffusion; right, a plot of D/D_0 vs. the dimensionless value ρ.

5.4 Hydrodynamic Discussions of the Flow Field about A Precessing Nanowire

Before we analyze the tracer tracks, it is very important to determine how well we can control our experimental parameters. I always used tracks of passive tracers in situ to measure the viscosity. Figure 5.8 is a diagram showing key parameters in the model cilium experiments.
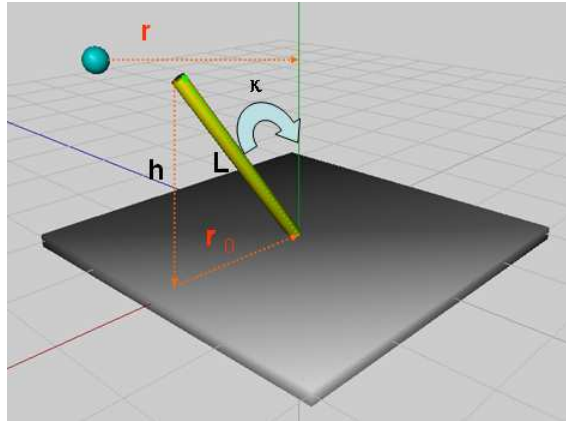
Figure 5.8, Key parameters of the microbead experiments. The magnetic nanowire (L in length) orbits along the Z axis sweeping a cone structure with tilt angle κ, cone height h, and top cone radius r_0. The microbead is r away from the precessing axis. Due to the viscous flow nature (dilute PS bead/water suspension), it is possible to model the whole flow field based on linear Stokes functions. The bead tracks unveiled this sub-micron fluid pattern near a precessing nanowire.

5.4.1 Angular Speed of the Flow Field about a Precessing Nanowire

In figure 5.4 we show a 2-D super imposed image of spherical tracers about a precessing nanowire. It is clear that the tracers travel with a large orbit around the precessing nanowire, and that the angular traveling arc length decays when the tracer's initial position is further away from the nanowire precessing center (figure 5.9). This is a feature of the flow pattern about a precessing nanowire.

To study how this angular velocity (V_θ) decays, I processed the data based on a time window sized to contain an integer number of epicycles. Three hundred consecutive frames (corresponding to 2.5 sec under a 120 fps capture rate) were selected to calculate the radial angles traversed by the microbead tracers. A dimensionless radial distance $\dfrac{r}{r_0}$ was defined by

the mean radial component of all 300 frames (<r>) divided by the precessing cone radius (r_0).

A linear fit of the log scale of the angles traveled vs. $\dfrac{r}{r_0}$ reveals a power decay rate of -2.8

(figure 5.9). Since the movie only recorded 2D information, the precessing cone height h_0

and the tracer Z direction height h were measured by focusing in Z with the stage in the

3DFM, which reports the Z position with a +/- 1 μm uncertainty. Tilt angle κ of the

nanowire was calculated from the relation tan(κ) = h / r_0. The tracer precessing angle θ was

computed based on a triangle composed of the cone center and the starting and ending tracer

positions ((x_0,y_0),(x_n,y_n)).

The flow field of a uniform flow past a sphere is,

$$V_\theta = -U \sin \theta (1 - 3a/4r - a^3/4r^3) \ (10)$$

here U is a uniform external flow, θ is the radial angle between flow velocity V and U, and a

is the sphere radius [13]. Substituting variable r, and normalizing give radial velocity V_θ' of

the flow which is generated by a sphere with velocity U in an otherwise still flow,

$$V_\theta' = U \sin \theta (3a/4r + a^3/4r^3) \ (11)$$

when a sphere is moving with velocity U in an unbounded viscous flow. As seen from

function (11), flow field V_θ' decays as 1/r in the far field. Similarly, flow outside of an

infinitely long cylinder rotating inside an unbounded viscous flow gives

$$V_\theta = \frac{\omega a^2}{r} \ (12),$$

where ω is the rotation frequency, a is the cylinder radius and r is the radial distance [13].

Obviously, the decaying speed of V_θ about a precessing nanowire is slower than both of

these flows (note here, the angle traveled decaying as $1/r^3$ suggests that the V_θ decays as $1/r^2$

since $V_\theta = \omega r$).
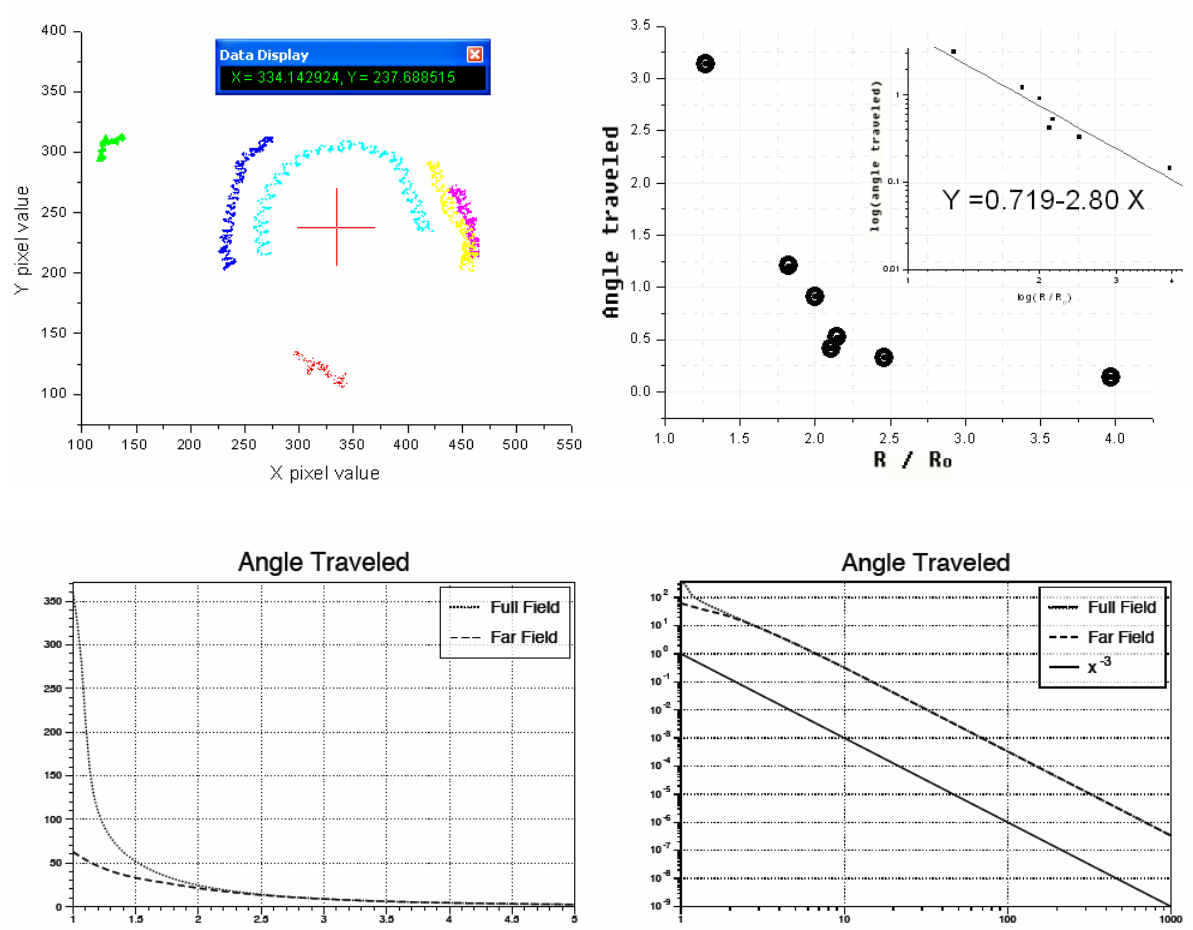
Figure 5.9, Angular speed decays in the radial direction in the flow field of a precessing nanowire. Top left, tracks of 1 μm PS micro beads around a precessing nanowire. The tracks here are superimposed from different experiments but are all about the same nanowire. The time scales of the data are all the same: 300 frames, 2.5 s. The cross center indicates the location of the nanowire precessing center; top right, tracer angle traveled vs. dimensionless tracer radial distance. R_0 is the precessing cone radius and R is the tracer radial distance to the precessing center. The inset reveals a -2.8 ratio from the log-log linear fit. The nanowire here orbited a cone structure with $R_0 = 12.61$ μm, h = 14.5 μm. Movies were taken at 14.5 μm above the bottom plane. Bottom, log-log linear fit of an angle traveled by a passive tracer around an arbitrary sweeping spheroid (x is the tracer initial radial position r/r_0 and y is the arbitrary velocity magnitude) to its dimensionless radial distance r/r_0 (courtesy from Terry Jo Leiterman's Ph.D. thesis figure 3.19).

Terry Jo Leiterman reported in her thesis that for a spheroid (an ellipsoid with two of its axis equal) sweeping out a double cone in free-space, at an arbitrary tilt angle θ and spheroid eccentricity e (for a spheroid $\frac{x^2}{a^2} + \frac{y^2 + z^2}{b^2} = 1$ (a > b), the eccentricity is expressed as e $= \sqrt{1 - (b/a)^2}$), the angle traveled in the far field decays as $1/(r/r_0)^3$. This matches my measurements (figure 5.11). Her theory of a slender body precessing on a no-slip plane predicts that the far field angle traveled decays by a $1/(r/r_0)^4$ power law, which does not match my experiment results [22]. As discussed above, the non-slip boundary condition is supposed to be met, so why this difference exists is a question which needs to be explored in the future.

I only measured the tracks outside the precessing cone structure because of the technical difficulties of capturing and analyzing tracers inside, but based on Terry Jo Leiterman's theory, large angular speeds occur inside the cone space. Following the dynamic similarity argument, table-top macro scale experiments are being explored extensively by a collaborating group to reveal the flow patterns inside the cone space.

5.4.2 Epicycles of the Flow Field about A Precessing Nanowire

Another feature of this flow is the epicycles shown in the tracer tracks (figure 5.10 A). The periodic epicycles we see are very interesting. This is the first time, both experimentally and theoretically, that this very unique attribute of the fluid pattern about a beating cilium has been unveiled. Even though this feature has been completely ignored in the literature, I found evidence of the existence of epicycles in nodal flows from previously published results [5, 7, 9, 10]. Some of their movies of beads (both in brightfield and fluorescence models) in nodal

flow suggest a flow pattern very similar to the epicycle structures seen in my magnetic nanowire experiments [23]. Attempts to simulate the nodal flow patterns [11] have also suggested epicyclical features in their results. Based on the experimental and theoretical studies of flow patterns about a precessing nanowire, I conjecture that the ignored epicycle structure is ubiquitous in all these mobile primary cilia flows, and it is natural to ask why these epicycles exist and what consequences may result from them.

When passive tracers flow around a precessing nanowire, they do not precess in smooth radial orbits like the creeping irrotational flow outside a rotating infinite cylinder in free space. A sub-micron sized particle at room temperature will definitely exhibit Brownian motion. However, in the near field, the Brownian motion is dominated by other regular secondary orbiting features which we call epicycles in this thesis due to their periodic orbiting apart from the obvious bigger primary orbits. Figure 5.10 B shows the variation of the radial components of this passive tracer with respect to the precessing center due to the flow generated by a precessing nanowire. The amplitude of the epicycle (in this specific case, around 1μm) is larger than the thermal diffusion root-mean-square distance in one dimension

$\sqrt{<R^2>} = \sqrt{2Dt}$ =0.42 μm ($D = \dfrac{kT}{6\pi\eta R}$) within 1/5 sec which is the duration time of one

epicycle.

I found this radial epicycle amplitude to be a function of several parameters. The variation of the epicycle amplitude due to different initial positions can be studied by either setting the focal plane still to record tracers at different 2D initial positions, or by setting the radial distance unchanged while recording tracer tracks at different h. Our optical microscopy system has much better resolution in radial direction (<0.226 μm) than the resolution in height (>1 um), so my experimental protocol is to set my observation plane near the top of

the nanowire to record the tracks of the microbeads in that plane. As demonstrated in figure 5.11, three tracers with different mean radial distances from the nanowire precessing center (but around the same precessing nanowire) showed different mean epicycle amplitudes. This suggests that, if choosing one specific nanowire (which means defined length, tilt angle, and orbiting features), epicycle amplitudes of tracers outside the precessing cone space decay with distance away from the precessing center.
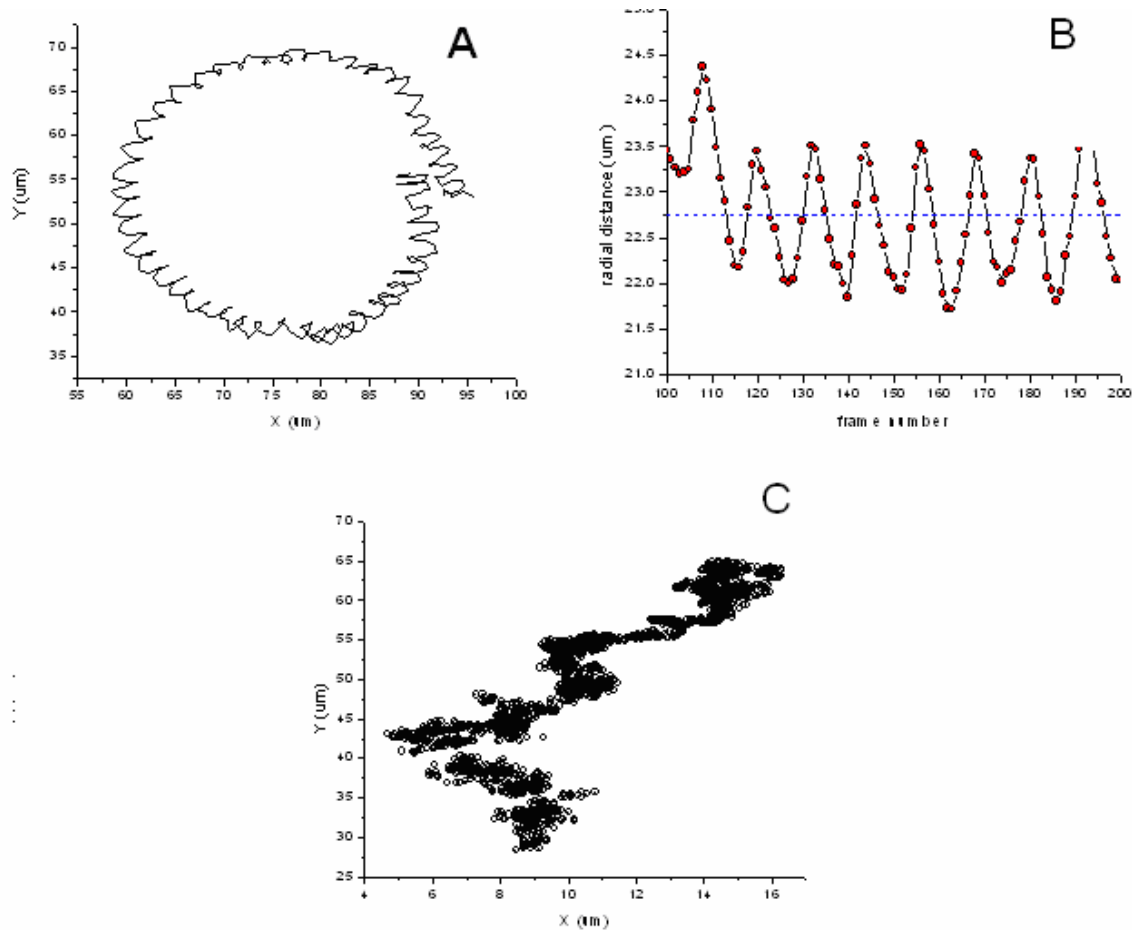
Figure 5.10, Epicycles in the flow fields generated by a precessing nanowire. A, a top view of a tracer track at $r/r_0 = 1.27$, $h/h_0 = 1$, closer to the precessing nanowire; B, radial positions of a tracer in frame sequence (time sequence) at $r/r_0 = 1.27$, $h/h_0 = 1$. Blue dash line is the mean radial value of the tracks; C, a top view of a tracer track at $r/r_0 = 3.9687$, $h/h_0 = 1$, further away from the precessing nanowire.

It is also clear that the tracer tracks in figure 5.11 are not held at a constant mean radial value. The "drifting" effect, shown as the bias of the tracer away from their mean radial distance on a time scale much longer than a single precessing orbit time, happens to every tracer in every radial position. I conjecture that Brownian motion is the main reason for this, since:

1.   The nature of a low Re Newtonian system (viscous flow) predicts the system will return back to its original state as long as the movements reciprocally return to the original position in the absence of Brownian motion.

2.   FFT of tracer radial position data did not show peak positions other than the harmonic frequencies close to nanowire precessing frequency.

To be safe, I also calculated the net "drifting distance" of the green track in figure 5.11 to be 4.5 μm in 200 frames, which was within the ability of a 3D Brownian motion (root mean square distance $\sqrt{<R^2>}$ = 7.3 μm, in water, 300 K, 1μm diameter tracers).

Figure 5.11 straightforwardly reveals that the epicycle amplitudes of tracers at different radii are different: the further way from the driving nanowire, the smaller the epicycle amplitude is. Another way to look at this decay phenomenon is by the standard deviation (STD) of the data within individual epicycles vs. their mean radius (figure 5.12). There is a clear trend indicating that the larger the radius of the tracer, the smaller the epicycle amplitude will be. Also notable is the wide distribution of the STD values around similar mean radial positions due to the Brownian motion.
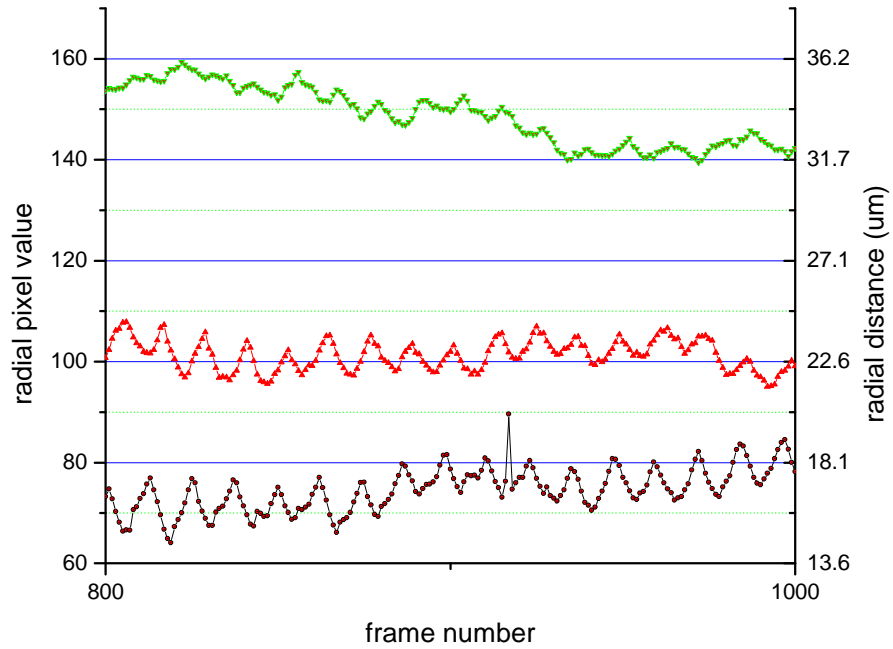
Figure 5.11, Epicycle amplitudes of tracers at different radial distances away from the magnetic nanowire rotation axis. From top to bottom, the three tracks are tracers respectively with mean radial distance to the precessing center of 33.6 μm, 22.89 μm, and 16.86 μm.
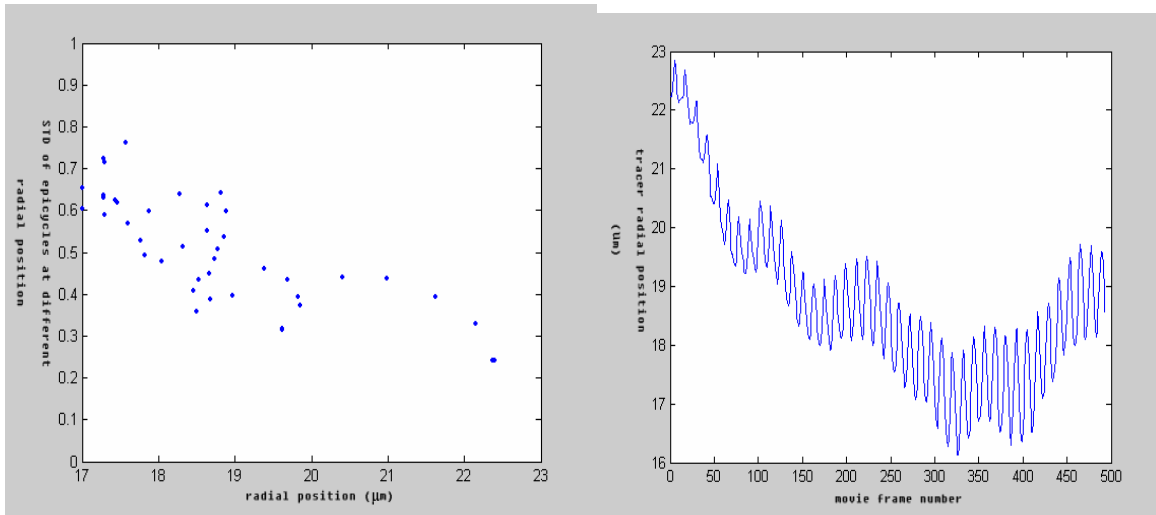
Figure 5.12, Epicycle amplitudes decay in the radial direction in the flow field generated by a precessing nanowire. Left, standard deviation of individual epicycles vs. their mean radius; right, experimental data consisting of 500 consecutive frames recording a tracer "drifting" in radial position.

The epicycles will, however, not be very obvious when tracers are further away from the precessing nanowire as in figure 5.10 C. Since the Brownian motion is of a comparable magnitude to the epicycles, it is hard to quantify the epicycle amplitudes based on direct measurements. By defining the radial value of the tracer track as

$$R_n = \sqrt{(x_n - x_0)^2 + (y_n - y_0)^2} \ \ (13),$$

we can compute the square root of the Fourier transform intensity of the projected R_n about the nanowire driving frequency as

$$P(\omega, \delta) = (\int_{\omega - \delta}^{\omega + \delta} \hat{R}_n(\kappa, t) d\kappa)^{1/2} \ \ (14),$$

as an indictor for epicycle amplitude. When the driving frequency is $\omega = 5$ Hz, $(\omega + \delta, \ \omega - \delta)$ is set to $(4.5, 5.5)$ [22]. Figure 5.13 is a plot of experimental epicycle amplitude intensity at different radial distances together with the free space theoretical results. The agreement between the experimental data and the theoretical predictions is good in the near field.

Experimental data, however, are systematically higher than the free space solutions in the far field. The reasons are still under discussion. One possible reason is that more than one nanowires exist in the sample cell during my experiments. Although they are outside the field of view, they may contribute to the epicycle amplitude. For the sample in figure 5.13, the cone radius was 12.61 um. The whole view area was approximately 11-12 times the cone radius. In Terry Jo Leiterman's thesis [22], she calculated that the epicycle amplitude decays as $1/(r/r_0)^3$ with a non-slip boundary, or as $1/(r/r_0)^2$ in the free space model (both with a 500 nm radius nanowire). No matter which model is used, it is possible that the existence of another nanowire within 8 radii (8.23 radius away if it is $1/(r/r_0)^3$ or 8.35 radius away if it is $1/(r/r_0)^2$) could cause the far field theory peak intensities to match the experimental results. It could be more complicated if there are multiple nanowires, and those nanowires might orbit

90

as a cone tilted toward the view area due to the symmetric nature of the driving magnetic field.
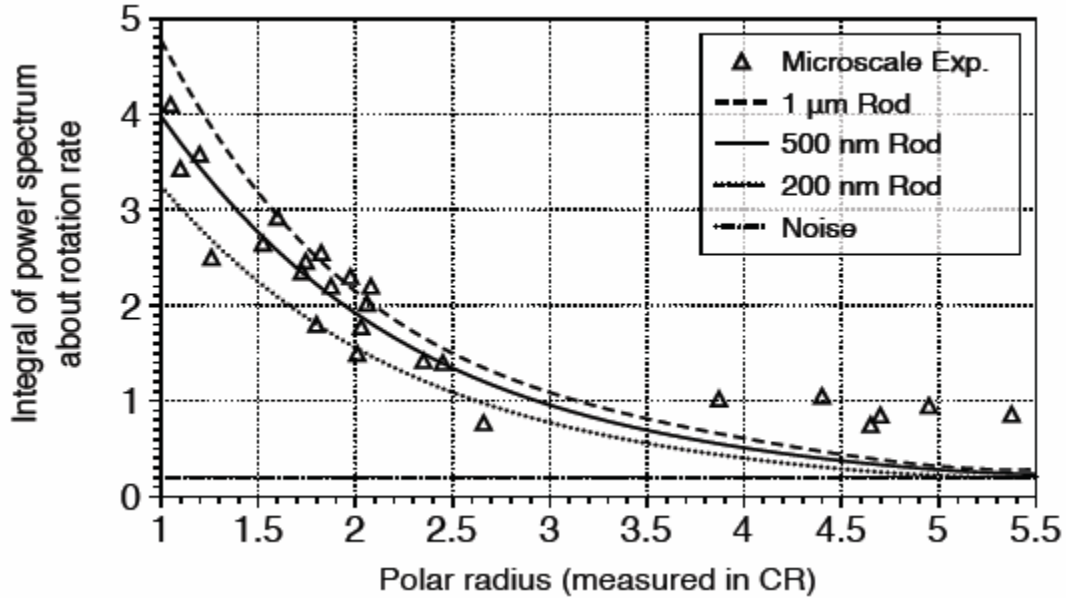
Figure 5.13, Experimental and theoretical epicycle power spectrum intensity about the nanowire precessing frequency (courtesy from Terry Jo Leiterman's Ph.D. thesis figure 6.2).

Also interesting is the periodic nature of the epicycle and its relation to the nanowire driving frequency. It is easy to falsely assume that the epicycle frequency would simply be commensurate with the nanowire precessing frequency. But Terry Jo's simulation revealed the periodic nature of the idea passive tracers is normally biased from the nanowire driving frequency (figure 5.14). One possible reason for this phenomenon is the following: as the tracer bead traverses an epicycle, it also continues in its orbit about the nanowire precessing center. Therefore, when the nanowire completes its orbit and returns to the original position, the bead has traversed some net angular distance about the its initial position and the rod must complete more than one full rotation in order to catch up to the bead after each epicycle. It follows then that the difference between the epicycle frequency and the rod driving

frequency should be equal to the orbital frequency of the tracer, or $f_{epicycle} + f_{orbit} = f_{rod}$.

Terry Jo Leiterman explored the parameter space and found that the epicycle structures were very sensitive to the initial positions of the tracers. For example, in figure 5.14, by setting tracers all at the same height, and the same starting cylindrical rotation angle but different radial distances, the track periods differ from each other. Terry Jo Leiterman's simulation pointed out that the difference in tracer trajectories after a single nanowire revolution is most notable inside the cone structure [22]. Trajectories outside this cone structure (where my experimental tracers were) appeared to change relatively little with changing initial radial position. Hence, with the thermal noise in this sub-micron experiment, this period mismatch phenomena is not very prominent in the outside area. In most of my experimental data, driving frequency (5 Hz in most of my experiments) can be a good approximation of the epicycle frequency. We have not yet explored different initial angular positions at a set radius, but we believe this will also give us an incommensurate period.
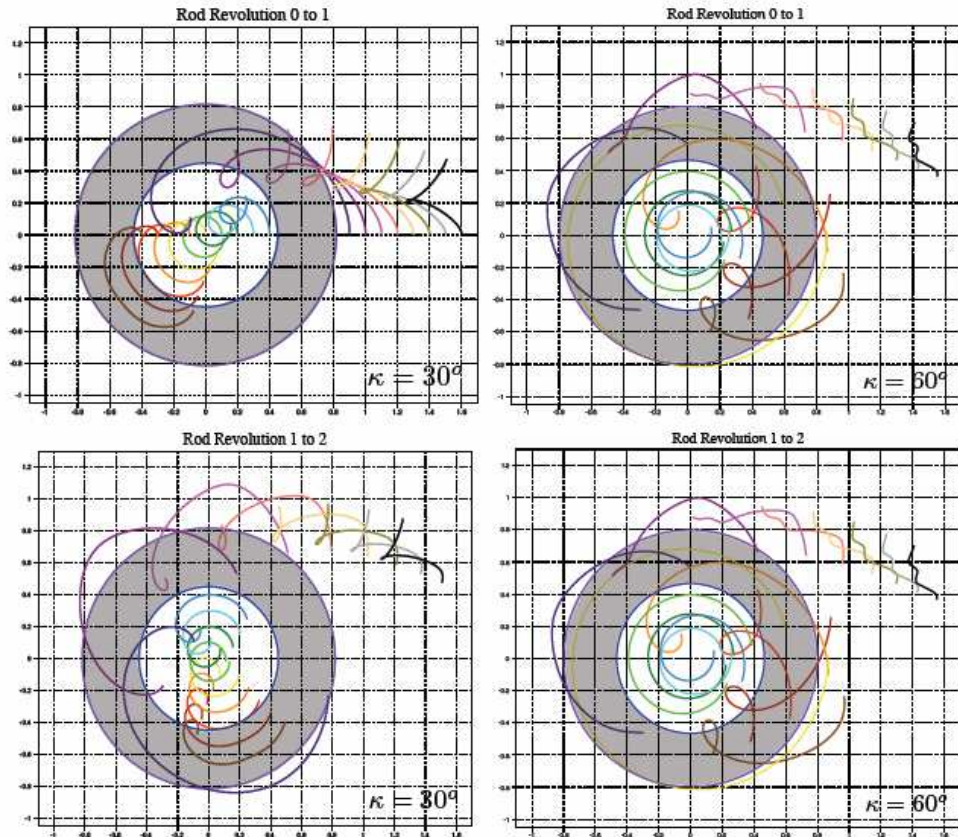
Figure 5.14, A top view of particle trajectories over consecutive spheroid revolutions for different initial positions for cone angle 30^0 (left column) and 60^0 (right column). The X and Y axes are in units of r/r_0. The paths are shown for spheroid revolutions 0 to 1, 1 to 2. The gray region is the annulus swept out by the spheroid with eccentricity e = 0.995 at the same height. (Courtesy of Terry Jo Leiterman's Ph.D. thesis figure 3.4)

5.5   Conclusion

In this chapter, experimental designs were presented to study sub-micron fluid dynamics of the flow pattern about a precessing magnetic nanowire. I discussed the features of this epicycle flow including the angular speed and the epicyclical amplitude. From my data, I find that the angular speed decays as $1/r^{-2.8}$, which is a faster decay than a uniform

flow passing a sphere or flow generated by a rotating cylinder. The experimental results match Terry Jo Leiterman's free space calculation well in the near field.

For the first time, I have revealed a ubiquitous epicyclical feature of the flow about a precessing slender body. By pointing out that the epicycle amplitude decays with distance away from the driving nanowire and exploring the periodic nature of these epicycle structures, unique features of nodal flow can be understood. The previously ignored epicycle structures from both experimental and theoretical results should be reviewed in order to build up a predictable hydrodynamic model for mobile primary cilia.

5.6   Reference

1.   Purcell, E.M., *Life at Low Reynolds Number*. 1976, Harvard University.

2.   Ibanez-Tallon, I., N. Heintz, and H. Omran, *To beat or not to beat: roles of cilia in development and disease.* Human Molecular Genetics, 2003. **12**: p. R27-R35.

3.   http://tidepool.st.usm.edu/crswr/ciliumxsect.html.

4.   Nonaka, S., et al., *Randomization of left-right asymmetry due to loss of nodal cilia generating leftward flow of extraembryonic fluid in mice lacking KIF3B motor protein.* Cell, 1998. **95**(6): p. 829-837.

5.   Nonaka, S., et al., *Randomization of left-right asymmetry due to loss of nodal cilia generating leftward flow of extraembryonic fluid in mice lacking KIF3B motor protein (vol 95, pg 829, 95).* Cell, 1999. **99**(1): p. -.

6.   Essner, J.J., et al., *Conserved function for embryonic nodal cilia.* Nature, 2002. **418**(6893): p. 37-38.

7.   Nonaka, S., et al., *Determination of left-right patterning of the mouse embryo by artificial nodal flow.* Nature, 2002. **418**(6893): p. 96-99.

8.   Hirokawa, N., et al., *Nodal flow and the generation of left-right asymmetry.* Cell, 2006. **125**(1): p. 33-45.

9.   Okada, Y., et al., *Mechanism of nodal flow: A conserved symmetry breaking event in left-right axis determination.* Cell, 2005. **121**(4): p. 633-644.

10.   Cartwright, J.H.E., O. Piro, and I. Tuval, *Fluid-dynamical basis of the embryonic development of left-right asymmetry in vertebrates.* Proceedings of the National Academy of Sciences of the United States of America, 2004. **101**(19): p. 7234-7239.

11.   Buceta, J., et al., *Nodal cilia dynamics and the specification of the left/right axis in early vertebrate embryo development.* Biophysical Journal, 2005. **89**(4): p. 2199-2209.

12.   White, F.M., *Fluid Mechanics*. 5 ed. 2004: Mc-Graw-Hill.

13.   Schlichting, H., *Boundary layer theory*. 1960, New York: McGraw-Hill.

14.   Macosko, C.W., *Rheology : principles, measurements, and applications*. Advances in interfacial engineering series. 1994, New York: VCH. xviii, 550.

15.   Groisman, A. and V. Steinberg, *Elastic turbulence in a polymer solution flow*. Nature, 2000. **405**(6782): p. 53-55.

16.   Groisman, A. and V. Steinberg, *Efficient mixing at low Reynolds numbers using polymer additives*. Nature, 2001. **410**(6831): p. 905-908.

17.   Turner, J.S., *Buoyancy effects in fluids*. Cambridge monographs on mechanics and applied mathematics. 1973, Cambridge Eng.: University Press. xv, 367.

18.   Pralle, A., et al., *Local viscosity probed by photonic force microscopy*. Applied Physics a-Materials Science & Processing, 1998. **66**: p. S71-S73.

19.   J. Happel, H.B., *Low Reynolds Number Hydrodynamics*. 1965: Prentice Hall, Englewood Cliffs,.

20.   Dufresne, E.R., et al., *Hydrodynamic coupling of two Brownian spheres to a planar surface*. Physical Review Letters, 2000. **85**(15): p. 3317-3320.

21.   Crocker, J.C., *Measurement of the hydrodynamic corrections to the Brownian motion of two colloidal spheres*. Journal of Chemical Physics, 1997. **106**(7): p. 2837-2840.

22.   Leiterman, T.J., *Exact and asymptotic low Reynolds, time-varying solutions for spinning rods with a comparison to experiments on the micro and macroscale*. 2006 University of North Carolina Chapel Hill

23.   Kramer-Zucker, A.G., et al., *Cilia-driven fluid flow in the zebrafish pronephros, brain and Kupffer's vesicle is required for normal organogenesis*. Development, 2005. **132**(8): p. 1907-1921.

CHAPTER 6 – Bio-macromolecules in Epicyclical Flow

6.1   Introduction

Researchers agree that disruption of the normal flow patterns of beating cilium in biological environment leads to a wide variety of malfunctions and diseases such as polycystic kidney disease, left-right asymmetry defects and retinal degeneration [1] [2]. In chapter 5, I have demonstrated that the epicyclical flow is one ubiquitous feature of the flow patterns about a beating cilium. For experimental and theoretical simplicity, I did all the hydrodynamic measurements in Chapter 5 in a Newtonian, viscous flow environment. It is important to explore the flow patterns in more biologically-related environments.

I approached this question with two strategies. One experiment used a low number density bio-macromolecule suspension (but still Newtonian) instead of the microbead water suspension used in Chapter 5. Since the solute concentration was so low (much lower than the overlap concentration, which will be explained later in this chapter), the low Re viscous flow assumption should hold well. The flow patterns should not change from the patterns revealed in Chapter 5. The conformation of the macromolecules themselves, however, might exhibit interesting features to reveal the hydrodynamic nature of the epicyclical flows.

Another experiment performed was to substitute the viscous liquids with more biologically-related viscoelastic fluids. Most known extra-cellular tissues are viscoelastic

materials with various high-molecular-weight polysaccharides [3, 4]. It is of interest to us to explore the flow patterns in these viscoelastic media and compare them to those found in Newtonian systems.

The fundamental understanding of non-linear rheology is still incomplete. The lack of standard experimental guidance even in the macro scale makes experimental design for rheology measurements on the sub-micron scale extremely difficult. Not only is there a need to face the challenge of the measurement uncertainty, but biological materials are by themselves vastly heterogeneous [5, 6]. The goal of my work is to trigger more interest in the area of beating cilium rheology. Much more work needs to be done to better interpret my results in this chapter.

6.2 Materials and Experiments

In this Chapter, I demonstrate the use of two macromolecules, λ-DNA and hyaluronan as model materials to study the nature of the epicyclical flow in more biologically-related environments.

Deoxyribonucleic acid (DNA) is a double helix polynucleotide molecule which contains genetic information. This double strain structure is composed of a pair of single chain molecules joined by hydrogen bonds. λ-DNA (Invitrogen (cat# 25250-010) of 0.25-0.6 μg/μL), specifically, is a double strain DNA segment isolated from an aam$^+$ dcm$^+$ E. coli LE597 losogen. Each λ-DNA has 48512 base pairs, which corresponds to a molecular weight of 32 X 10^6 daltons (Da) and a contour length (linear end to end distance) of 16-17 μm. DNA is a polyelectrolytic molecule. The charges on its backbone repel each other making the

molecule very stiff, with a persistence length of 50nm or a Kuhn Length 100 nm if λ-DNA is treated with the ideal chain model [7] [8].

Hyaluronan (hyaluronic acid, HA) is a high-molecular-weight polysaccharide belonging to the glycosaminoglycans class and found in the extra cellular matrix [3]. It is a unique biopolymer which is found in all tissues and bodily fluids of every mammalian species, as well as in microorganisms. The chemical structure of HA is simple. The repeat unit is a disaccharide, -D-glucuronic acid-beta-1, 3-N-acetylglucosamine-beta-1,4 (figure 6.1). It is worth noting that the polymer backbone has one base and one acid functional group per repeat unit. The effective charge of the polymer is very sensitive to the environmental pH.
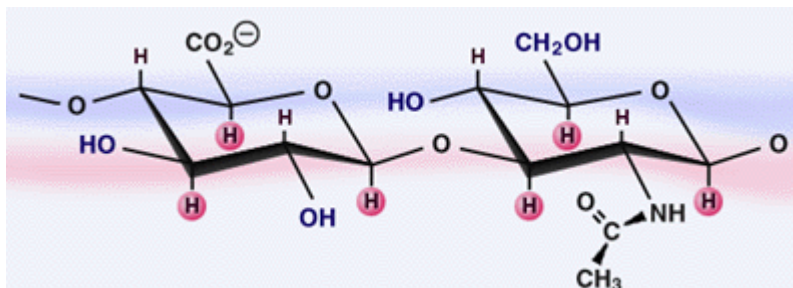
Figure 6.1, Schematic of disaccharide repeat unit of HA -D-glucuronic acid-beta-1, 3-N-acetylglucosamine-beta-1,4 (copy from [9])

6.2.1   YoYo-1 Dyed λ-DNA

I used fluorescently labeled DNA as tracers for imaging purposes. When stained, the contour length changes from 16-17 μm to 22 μm, based on Perkins's measurements [10]. Due to the entropic elasticity, the neutral status of a dyed DNA (low concentration environment) in still aqueous media is spherical with a radius of gyration of 0.5-0.7 μm according to the literature [11] [12]. Hagerman's research showed that the radius of gyration

of DNA decreases monotonically with increased ionic strength and finally reaches a plateau once the concentration of NaCl reaches 10 mM [13]. Therefore we made our sample in a 10 mM NaCl buffer in all the measurements in this thesis. The details of this staining procedure are listed here. The as-purchased DNA solution was heated to 65ºC for more than 15 min. (Since λ-DNA has two dangling single strand complementary with each other at its two ends (short 12 bp single-stranded ends), a heating procedure is necessary to disrupt the hydrogen bonds in between. Sometimes, it may be necessary to block the dangling ends with a 1000X stoichiometric complementary oligonucleotide (5' – GGG CGG CGA CCT – 3' or 5' – AGG TCG CCG CCC – 3' from UNC Oligonucleotide Synthesis Core Facility) for better dissociation effects. The extra oligonucleotide should be centrifuged away with Microcon filtration (cutting off M_w = 100,000).) Then, the dilute λ-DNA solution (1:1000 of origin stock, in Tris-EDTA buffer) was mixed with stoichiometric 4bp:1 YOYO-1 dye (Molecular Probes, 1 μM). Then we added β-mercaptoethanol (1:100, v/v), glucose oxidase (0.05 mg/ml), and Catalase (0.01 mg/ml) to stained λ-DNA solution to prevent bleaching. The final mixture was kept in a dark environment at room temperature for fresh experiments [14].

6.2.2   5-aminofluoresein Labeled Hyaluronan

The commercially available fluorescently labeled HA (f-HA) is not designed to be used as a fluidic tracer. Its molecular weight is low and normally without detailed polymer physical measurements of its molecular weight distribution. There are papers which introduce several procedures for f-HA synthesis [15] [16] [17] [18]. Based on the availability of raw materials and synthesis facilities, we succeeded in the synthesis of f-HA by modifying a recipe from Hiroyuki Nagata [17].

A mixture of HA (Sigma Hyaluronic acid sodium salt from rooster comb, Mw $\sim 10^6$ Da, 100 mg), 5-aminofluoresein (140 mg, 1.6 eq) and EDC hydrochloride (0.5 g, 10 eq) was mixed with pyridine-HCl (5 mL, a 1:1 mixture of pyridine and 12 N HCl, PH~4.5). This mixture was swollen at room temperature for 12 hr and dialyzed via deionized water several times until no free dye was released into the water. The product was then treated with 0.1 N NaOH for 4 hr, and further dialyzed four times to obtain a yellow solution.

6.3   Conformation of a Single λ-DNA in Epicyclical Flow

Over the past 10 years, a new technique called single molecule imaging has gained a great deal of attention. Beginning with Perkins [10], methods of imaging the conformations of isolated DNA molecules by fluorescence microscopy in well-defined flows have become increasingly important for single molecule polymer physics, rheology, and biophysical studies [19]. In particular, a series of Science papers from Chu's group built up a solid understanding of how a single high-molecular-weight DNA would respond to several simple viscous flows [8, 20-23] [24]. Both experiments and simulations have been discussed, and the common understanding is that the conformations adopted by DNA in these simple steady viscous flows can be well explained and predicted by classic Flory theory [25]. The key dimensionless parameter which unambiguously defines the flow strength in different flow patterns is the Weissenberg number (W_i) or Deborah number (D_e) which is the product of the longest relaxation time of the polymer chain and the strain rate, $W_i = De = \tau * \dot{\gamma}$ [26]. Our purpose here is to explore the effects of a cilium epicyclical flow on a high-molecular-weight bio-macromolecule in the near field, based on a discussion of the Weissenberg number.

Both experimental and theoretical studies point out that the onset W_i value of drastic

conformation changes of DNA varies in different flow patterns [20-23, 27, 28]. The conformations adopted by each DNA are random, but the statistical mean fractional stretch length $\langle X \rangle$ ($X = L/L_0$, the ratio between the stretched length to the contour length), leads to consistent results. Until now, the only flow patterns to have been studied by single molecule imaging studies are simple shear flows, one- or two-dimensional extensional flows, and combinations of the two [19, 20, 23, 27]. There have been no published results related to conformations of a single polymer in a time-variant flow. Larson [27] analyzed the published data of a single λ-DNA in both extensional flows and shear flows to get the plot shown in figure 6.2. It is clear that the extensional flow is much more efficient in stretching the DNA than a steady shear flow.
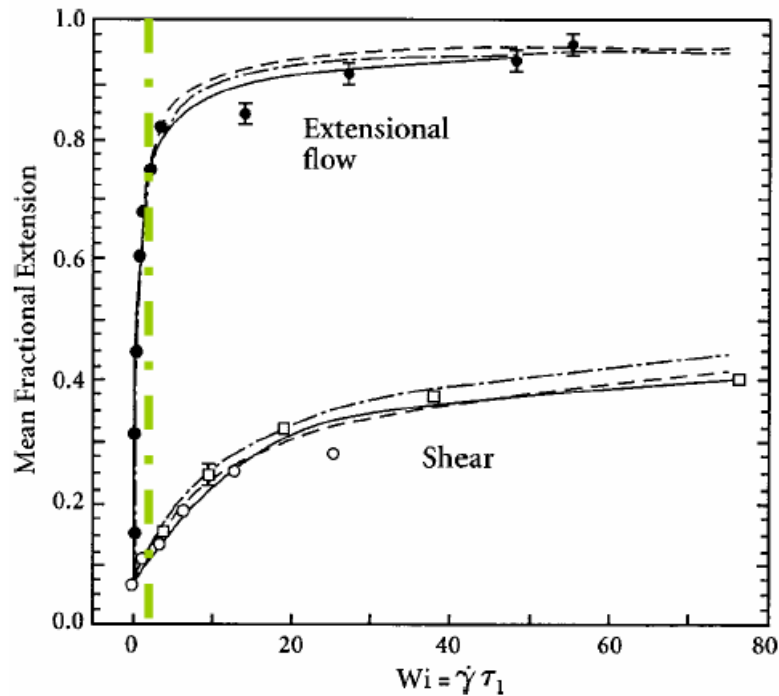
Figure 6.2, Mean fractional extension $\langle X \rangle$ of λ-DNA vs. W_i in both simple shear and extensional flows. The solid lines are guide lines through experimental data and the dashed lines are from numerical simulations. The green dash line is a guidance line of $W_i = 2$, which is a typical value in my nanowire experiments. (modified from [27])

As discussed above, in order to treat the flow field as a Newtonian epicyclical flow, it is important to make the DNA buffer very dilute. Pervaded volume V is the volume of solution spanned by one polymer chain $V \propto R^3$. The volume fraction of a single molecule inside its pervaded volume is called the overlap volume fraction δ. The concentration corresponding to $\delta = 1$ is the overlap concentration C^* [25]. The radius of gyration of an ideal λ-DNA polymer chain, which is the case in dilute λ-DNA in a 10 mM NaCl water solution, is

$$R^2{}_g = \frac{Nb^2}{6} \quad (1)$$

The overlap concentration is then,

$$C^* = \rho b^d N / R^d = \frac{M / N_{Av}}{\frac{3}{4}\pi R_g^3} \propto M^{1-3\nu} \quad (2)$$

where N is the number of repeat units; b is Kuhn length of the DNA, which is around 100 nm; and ν is the dimensionless scaling exponent. Water is a good solvent for DNA on length scales as large as λ-DNA in ideal chain model. From ideal chain model theory, ν = 0.6, or from a more detailed scaling argument of a worm-like-chain (WLC) model, ν = 0.588, and $C^* \approx 0.04$ mg/ml. Equation (2) also suggests that when ν = 0.6, C^* is proportional to $M^{-4/5}$ as in Flory's mean field theory [25].

The viscosity η of a dilute hard sphere suspension as a function of the volume fraction of the dispersed hard spheres, Φ, is,

$$\frac{\eta}{\eta_0} = 1 + \frac{5}{2}\Phi + f(\Phi^2) \quad (3) \text{ [25]}.$$

So as long as aqueous λ-DNA suspensions have a concentration well below 0.04 mg/ml ($\Phi \ll 1$), we can treat them as Newtonian liquids with basically the same viscosity as their buffer.

We used a 10^{-3} C^* YoYo-1 dyed λ-DNA buffer solution as the medium to run the same experiments introduced in Chapter 5. Here the microbead tracers were substituted with the 500-700 nm fluorescent λ-DNA. We recorded the conformational changes of dyed λ-DNA inside epicycles hoping to reveal the biological consequences of a beating primary cilium to bio-macromolecules in the near field. However, experiments with short exposure times (5 ms and 1 ms) did not provide any convincing images of fully-stretched DNA. Driven by nanowires (in 2 cp buffer with the same precessing frequency as wild mouse nodal cilia at 5 Hz, but with much longer cilia), the epicyclical flow at 1.1 fractal radii away from a nanowire as long as 37 μm, at about a 45° tilt angle may not have the ability to fully stretch a λ-DNA in its steady state. It seems that the only reasonable conclusion is that, even when λ-DNA can be stretched by the epicyclical flow, the stretching mean fractal length <X> is only a small value, where $<X> \equiv L/L_{contour}$.

Bird predicted that, in extensional flows, an abrupt coil-stretch transition for polymers would occur at a dimensionless flow strength number of $W_i = 0.5$ [29]. Terry Jo Leiterman's numerical simulation of the maximum eigenvalue of the stress tensor in the above example suggested that, at the near field, $W_{imax} \approx 0.8$ (in 2 cp media, $\tau \approx 0.2$ s) (figure 6.3). Hence, the absence of obvious stretching of λ-DNA close to a precessing nanowire leads to the conclusion that this epicyclical flow pattern is not as efficient as a pure elongation flow in deforming bio-macromolecules. The fundamental reason for this may be related to the fact that the maximum eigenvalue direction changes within every epicycle. Most of the time, this

eigenvalue direction does not align with the DNA precession direction, so once a DNA is stretched in the larger eigenvalue area, it may quickly be compressed? within one epicycle. The fluctuation of DNA conformation changes we observed in the epicyclical flows is similar to what happens in the simple shear flow where the rotational component in the stress tensor leads to a polymer molecule irregularly stretching, tumbling, and coiling. The direct observation by Smith et al. 1999 [23] revealed that stretching in simple shear flow was not as monotonic as stretching in an extensional flow. Unlike in a simple shear flow, however, the "compression" effect of epicyclical flow is a periodic effect. It may make a full stretching movement difficult to realize in epicyclical flows.
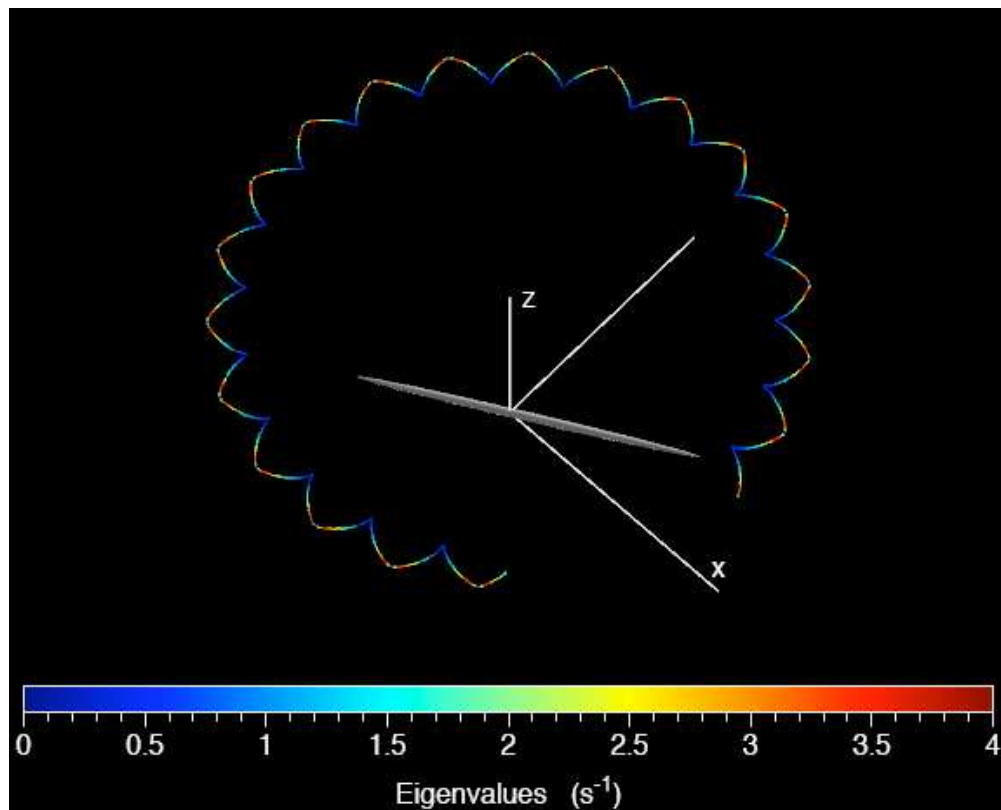
Figure 6.3, Maximum eigenvalues along the trajectory (Lagrangian) from the slender (asymptotic) free space theory simulation. This was a 500 nm diameter rod precessing with a cone height 27 um, a cone radius 26 um; the starting radial position of the DNA tracer was 31 um, and the height was 24.85 um. (unpublished results from Terry Jo Leiterman)

6.4   Epicyclical Flow Field in a Viscoelastic HA Solution

HA aqueous solution is well known for its very non-linear viscoelastic properties [30]. Theoretical and experimental results from the literature are not consistent about the persistence length of HA in an aqueous buffer solution. I chose Mendichi's results with an intrinsic persistence length of 7.5 nm, based on his intrinsic viscosity data [31]. Compared with the persistence length of DNA of 50 nm, HA is much softer. The radius of gyration of a 10^6 Da single HA in still water in an ultra low concentration is around 126 nm according to the measurements performed by Mendichi et al [31]. According to the equation

$$C^* = \rho b^d N / R^d = \frac{M / N_{Av}}{\frac{3}{4} \pi R_g^3}$$, the overlap concentration of my HA sample is around 0.35

mg/mL.

I prepared a HA pH 7.0 aqueous solution by dissolving 4.3 mg HA in 1 ml miliQ water with 0.1 M NaCl which is more than 10 times the overlap concentration[2]. Figure 6.4 reveals that the HA solution (4.3 mg/ml) started a clear shear thinning trend at shear rate $\dot{\gamma}$ higher than 10 Hz. We also looked at the frequency sweep cone and plate data to check the cross point of real and imaginary moduli. From figure 6.5, it is clear that, at frequencies higher than 2 Hz, the elastic component is prominent in this HA solution.

---

[2] With a 0 shear complex viscosity around 60 cp according to cone and plate measurements at 23 ℃.
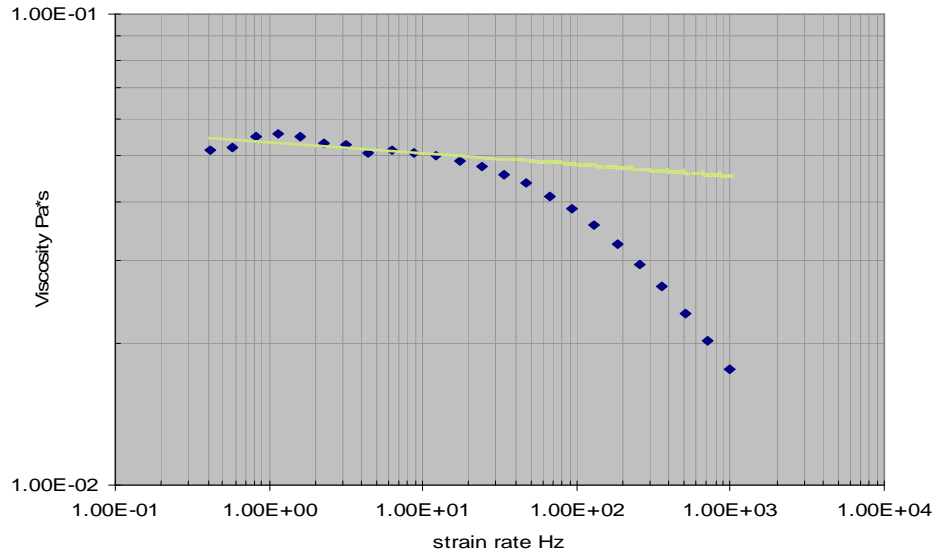
Figure 6.4, Log-log plot of apparent viscosity vs. strain rate based on a 1° cone and plate measurement at 23 ℃, 5 Hz. There is a clear shear thinning at strain rates over 10 Hz in HA 4.3 mg/ml buffer.
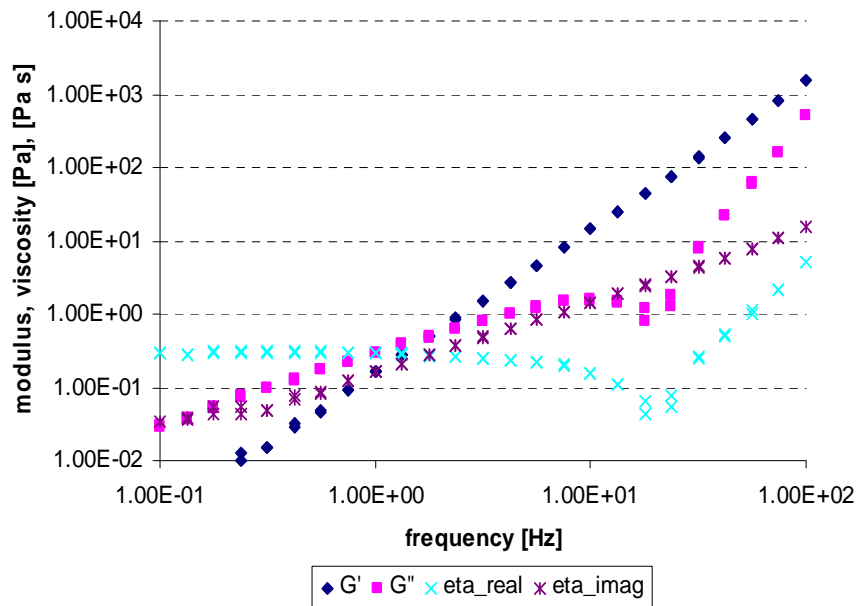
Figure 6.5, Log-log plot of modulus and viscosity vs. sweeping frequency based on a 1° cone and plate measurement at 23 ℃ with constant strain amplitude of 2%. The elastic modulus is prominent when the oscillating frequency is higher than 2 Hz in HA 4.3 mg/ml buffer.

The flow patterns about a precessing magnetic nanowire after mixing 0.1% v/v 500 nm fluorescent microbeads inside the HA solution (4.3 mg/ml) was recorded. Figure 6.6 is a superimposed image revealing the flow nature about a precessing nanowire in this HA solution. Due to a much higher viscosity than water, the Brownian motion is highly restrained, with the trade off that it was much more difficult to find a long precessing nanowire because of the large hydrodynamic dragging force generated when the nanowires move. Again, based on $\frac{\eta}{\eta_0} = 1 + \frac{5}{2}\Phi + f(\Phi^2)$, a solute of less than 0.1 % v/v microbeads will not lead to a significant change in viscosity from the original solution, so I used a higher bead number density for more efficient measurements in the far field.
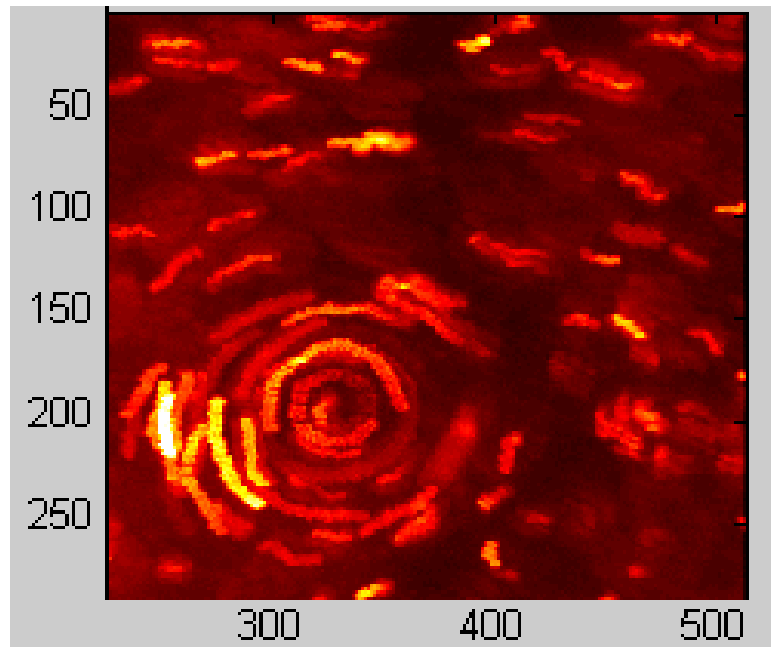
Figure 6.6, Superimposed image of 500 nm fluorescent tracer tracks in HA (4.3 mg/ml) about a precessing nanowire. The cone radius was 11.66 μm; the cone height and the observation plane were both at 13.2 μm; and the exposure time was 1 ms. X and Y are pixel values.

It is clear that the tracers in HA also show a decay in their angular traveled distance

as radial distance increases. Instead of processing the data with Spot Tracker, which had difficulty with differentiating two beads bypassing each other, I superimposed the frames of the experimental movies to calculate the angular speed at different dimensionless radial distances r/r_0. The angular speed data were then plotted in log scale and compared with the same values from the water microbead experiments in figure 6.7.

The slower decay of angular speed in the radial direction in this epicyclical flow is revealed here for the first time. For a typical nanowire with a precessing cone radius of 15 μm, a tilt angle of 45°, and a precessing frequency of 5 Hz, the strain rate at the precessing cone plane can be determined based on Terry Jo Leiterman's scaling arguments which point to a $1/(r)^3$ radial velocity decay rate as,

$$\left|\dot{\gamma}\right| = \left|\frac{dv}{dr}\right| = \left|d(\frac{2\pi\omega r}{r^3})/dr\right| \approx \frac{62.8}{r^3} \quad (4)$$

Here $\dot{\gamma}$ is the strain rate, ω is the precessing frequency, and r is the dimensionless radial distance $\frac{r}{r_0}$. This leads to a $\dot{\gamma}$ value of 40-50 s^{-1} at 1.1 cone radii away from the nanowire tip. Obviously, at this shear rate, the HA solution has already shown shear thinning properties from figure 6.4. We proposed that the complicated viscoelastic nature of the HA solution might contribute to this phenomenon.
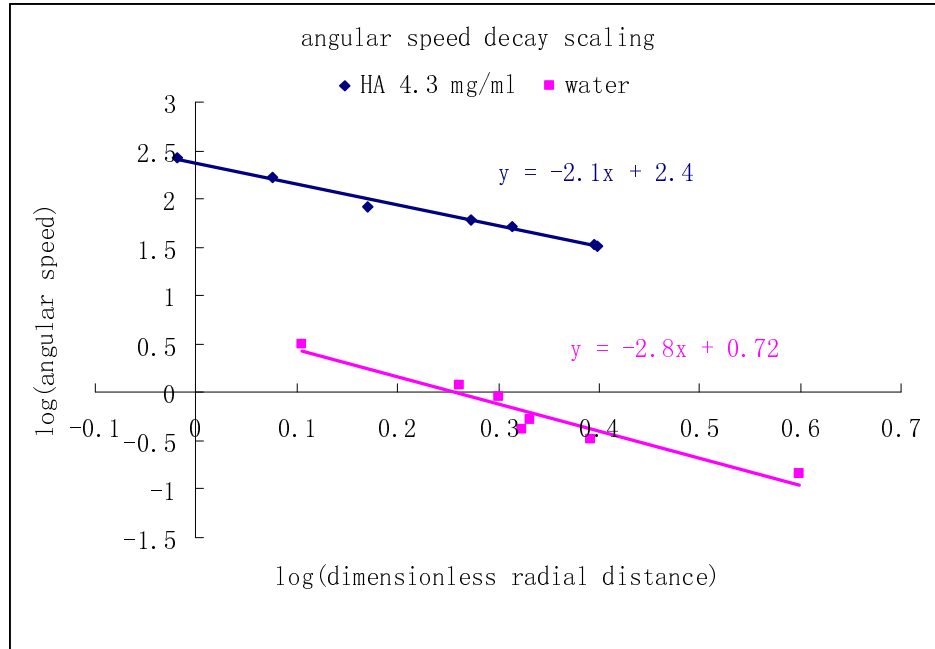
Figure 6.7, Log-log plot of angular speed vs. radial distance r/r_0 in both HA and water.

In the simplest models, like the Kelvin model and the Maxwell model, which are represented by a set of spring and dashpot elements in series and in parallel, viscoelasticity can be decomposed into independent elastic and viscous parts [32]. The elastic component of the stress is in phase with the applied strain, and the ratio of this stress to the strain is the storage modulus G', the real part of complex modulus G^*. The viscous component of the stress is out of phase with the strain and the ratio of this stress to the strain is the loss modulus G'', the imaginary part of G^*. Generally, for non-linear viscoelastic materials like this HA 4.3 mg/ml solution, the applied deformation energy is stored and dissipated at the same time and the ratio between the energy in the two parts is related to the exerting strain rates. Before Fahir's first work in 1998 [33], there had been no attempt to resolve the problem of a linear viscoelastic flow about an oscillating rod, so, regarding the highly time-dependent, non-linear properties of the HA 4.3 mg/ml solution, the reason for this slower

angular velocity field dissipation in the radial direction is currently without interpretation. One example which may help us to understand the phenomenon is to treat the angular velocity decay in the epicyclical flow as the attenuation of a harmonic oscillation in a semi-infinite Couette flow in different media. In Hermann's and Ferry's calculations, we have dimensionless functions, [34] [32]

$$\frac{\partial v_x}{\partial t} = \frac{1}{\text{Re}} \frac{\partial^2 v_x}{\partial y^2}, p = 0 \qquad (5)$$

$$\tau_{xx} = \tau_{yy} = \tau_{zz} = \tau_{xz} = \tau_{yz} = 0$$

$$\frac{\partial v_x}{\partial t} = \frac{1}{\text{Re}} \frac{\partial \tau_{xy}}{\partial y}, p = p_0(t) \qquad (6)$$

$$\tau_{xx} = \tau_{yy} = \tau_{zz} = 0$$

for viscous and linear viscoelastic models, respectively. Here the boundary condition is V(t) = $V_0 \sin(\omega t)$ at the bottom plate; oscillation amplitude A = V_0/ω; Re = $\dfrac{A^2 \omega}{\eta_0 / \rho}$. τ is the dimensionless stress term; v is the dimensionless velocity term; p is the dimensionless pressure term. x is the 1 D oscillation direction; y is the direction normal to the Couette plane; and z is the other Cartesian axis.

The solutions of functions (5) and (6) in a semi-infinite Couette flow are listed here:

$$\left| v_{(y,t)} \right| = v_0 \exp(-y * \sqrt{\frac{\rho \omega}{2\eta}}) \qquad (7)$$

$$\left| v_{(y,t)} \right| = v_0 \exp(-y * \sqrt{\frac{\rho \omega}{2|\eta *|}(1 - \frac{\eta''}{|\eta *|})}) \qquad (8)$$

If we normalize the two solutions based on the same apparent viscosity η, we find the elastic term in the viscoelastic materials will always make the amplitude V_{yx} bigger at the same y,

since for $\eta'' > 0$ for most materials, $\left|v_{(y,t)}\right|$ viscoelastic $/ \left|v_{(y,t)}\right|$ viscous < 1. This slower decaying of the velocity in the normal direction by a harmonic boundary oscillation due to the elastic component brings light to our observations in HA [35]. To explore the results in shear thinning media, however, may require new approaches which are in progress in the Virtual Lung project.

I have already mentioned in Chapter 4 that mixing in a low Re environment is hard to achieve. The obvious difference in the angular velocity decay rate between water and HA solution may have very interesting biological consequences, in particular, the extension of the vorticity component about a beating cilium in a shear thinning media like 4.3 mg/ml HA.

6.5   Conclusion

In this chapter, I studied the epicyclical flow in a more biologically-related environment. Using λ-DNA as a tracer, we analyzed the macromolecule response to this man-made epicyclical cilium flow. The lack of a fully stretched single λ-DNA may suggest that the epicyclical flow is not as efficient as a pure unilateral elongation flow to stretch a biomacromolecule. We conjecture that this is due to the periodic rolling of the maximum eigenvalue directions of the flow stress tensor.

A nanowire precessing in a shear thinning HA solution provided a good approximation of a rigid primary cilium beating inside a viscoelastic media. Cone and plate measurements revealed viscoelastic nature of the HA solution (4.3 mg/ml). The apparent extension of the vorticity component was attributed to the prominent elastic modulus when the strain rate enters a non-Newtonian region.

6.6 References

1.   Afzelius, B.A., *Cilia-related diseases.* Journal of Pathology, 2004. **204**(4): p. 470-477.

2.   Ibanez-Tallon, I., N. Heintz, and H. Omran, *To beat or not to beat: roles of cilia in development and disease.* Human Molecular Genetics, 2003. **12**: p. R27-R35.

3.   Ambrosio, L., et al., *Rheological study on hyaluronic acid and its derivative solutions.* Journal of Macromolecular Science-Pure and Applied Chemistry, 1999. **A36**(7-8): p. 991-1000.

4.   Masuda, A., et al., *Novel distance dependence of diffusion constants in hyaluronan aqueous solution resulting from its characteristic nano-microstructure.* Journal of the American Chemical Society, 2001. **123**(46): p. 11468-11471.

5.   Amblard, F., et al., *A magnetic manipulator for studying local rheology and micromechanical properties of biological systems.* Review of Scientific Instruments, 1996. **67**(3): p. 818-827.

6.   Oddou, C., D. Geiger, and S. Naili, *Nonstationary Rheology of Biological Tissues - Viscoelasticity or Poroelasticity.* Biorheology, 1986. **23**(2): p. 134-134.

7.   Smith, D.E., T.T. Perkins, and S. Chu, *Dynamical scaling of DNA diffusion coefficients.* Macromolecules, 1996. **29**(4): p. 1372-1373.

8.   Smith, D.E. and S. Chu, *Response of flexible polymers to a sudden elongational flow.* Science, 1998. **281**(5381): p. 1335-1340.

9.   http://www.glycoforum.gr.jp/science/hyaluronan/HA01/HA01E.html.

10.   Perkins, T.T., et al., *Relaxation of a Single DNA Molecule Observed by Optical Microscopy.* Science, 1994. **264**(5160): p. 822-826.

11.   Smith, D.E., T.T. Perkins, and S. Chu, *Self-Diffusion of an Entangled DNA Molecule by Reptation.* Physical Review Letters, 1995. **75**(22): p. 4146-4149.

12. Babcock, H.P., et al., *Visualization of molecular fluctuations near the critical point of the coil-stretch transition in polymer elongation.* Macromolecules, 2003. **36**(12): p. 4544-4548.

13. Hagerman, P.J., *Flexibility of DNA.* Annual Review of Biophysics and Biophysical Chemistry, 1988. **17**: p. 265-286.

14. Teixeira, R.E., et al., *Shear thinning and tumbling dynamics of single polymers in the flow-gradient plane.* Macromolecules, 2005. **38**(2): p. 581-592.

15. Glabe, C.G., P.K. Harty, and S.D. Rosen, *Preparation and Properties of Fluorescent Polysaccharides.* Analytical Biochemistry, 1983. **130**(2): p. 287-294.

16. Liberda, J., M. Ticha, and V. Jonakova, *Preparation of fluorescein-labelled and biotinylated derivatives of polysaccharides for lectin-saccharide binding studies.* Biotechnology Techniques, 1997. **11**(4): p. 265-267.

17. Nagata, H., et al., *Molecular-weight-based hyaluronidase assay using fluorescent hyaluronic acid as a substrate.* Analytical Biochemistry, 2004. **330**(2): p. 356-358.

18. Ogamo, A., et al., *Preparation and Properties of Fluorescent Glycosaminoglycuronans Labeled with 5-Aminofluorescein.* Carbohydrate Research, 1982. **105**(1): p. 69-85.

19. Slater, G.W., et al., *Deformation, stretching, and relaxation of single-polymer chains: Fundamentals and example.* Soft Materials, 2004. **2**(2-3): p. 155-182.

20. Perkins, T.T., D.E. Smith, and S. Chu, *Single polymer dynamics in an elongational flow.* Science, 1997. **276**(5321): p. 2016-2021.

21. Perkins, T.T., et al., *Stretching of a Single Tethered Polymer in a Uniform-Flow.* Science, 1995. **268**(5207): p. 83-87.

22. Schroeder, C.M., et al., *Observation of polymer conformation hysteresis in extensional flow.* Science, 2003. **301**(5639): p. 1515-1519.

23. Smith, D.E., H.P. Babcock, and S. Chu, *Single-polymer dynamics in steady shear flow.* Science, 1999. **283**(5408): p. 1724-1727.

24. Chu, S., *Single-molecule studies of the extension of polymers in shear, elongational, and mixed flows.* Abstracts of Papers of the American Chemical Society, 2001. **221**: p. U314-U314.

25. Michael Rubinstein, R.H.C., *Polymer physics.* 2003, New York Oxford University Press.

26. Larson, R.G., et al., *Hydrodynamics of a DNA molecule in a flow field.* Physical Review E, 1997. **55**(2): p. 1794-1797.

27. Larson, R.G., *The rheology of dilute solutions of flexible polymers: Progress and problems.* Journal of Rheology, 2005. **49**(1): p. 1-70.

28. Schroeder, C.M., E.S.G. Shaqfeh, and S. Chu, *Effect of hydrodynamic interactions on DNA dynamics in extensional flow: Simulation and single molecule experiment.* Macromolecules, 2004. **37**(24): p. 9242-9256.

29. R. B. Bird, C.F.C., R. C. Armstrong,, *Dynamics of Polymeric Liquids.* 2 ed. 1987, New York: Wiley,.

30. Tuinier, R., et al., *Concentration and shear-rate dependence of the viscosity of an exocellular polysaccharide.* Biopolymers, 1999. **50**(6): p. 641-646.

31. Mendichi, R., L. Soltes, and A.G. Schieroni, *Evaluation of radius of gyration and intrinsic viscosity molar mass dependence and stiffness of hyaluronan.* Biomacromolecules, 2003. **4**(6): p. 1805-1810.

32. Ferry, J.D., *Viscoelastic properties of polymers.* 1980, New York: John Wiley.

33. Akyildiz, F.T., *Longitudinal and torsional oscillations of a rod in a viscoelastic fluid.* Rheologica Acta, 1998. **37**(5): p. 508-511.

34. Schlichting, H., *Boundary layer theory.* 1960, New York: McGraw-Hill.

35. Yao, L.X., *unpublished results.* 2006.